GAP FILLING OF OPTICAL REMOTE SENSING MULTI-SOURSE DATA CUBE THROUGH MULTI-SCALE AND MULTI-TEMPORAL SEGMENTATION

Rennan de Freitas Bezerra Marujo

Doctorate Thesis of the Graduate Course in Applied Computing, guided by Dr. Leila Maria Garcia Fonseca, approved in March 27, 2019.

URL of the original document:
<http://urlib.net/8JMKD3MGP3W34R/3SUESRS>

INPE

São José dos Campos

2019

sid.inpe.br/mtc-m21c/2019/03.20.17.01-TDI

GAP FILLING OF OPTICAL REMOTE SENSING MULTI-SOURSE DATA CUBE THROUGH MULTI-SCALE AND MULTI-TEMPORAL SEGMENTATION

Rennan de Freitas Bezerra Marujo

Doctorate Thesis of the Graduate Course in Applied Computing, guided by Dr. Leila Maria Garcia Fonseca, approved in March 27, 2019.

URL of the original document:
<http://urlib.net/8JMKD3MGP3W34R/3SUESRS>

INPE

São José dos Campos

2019

Aluno (a): **Rennan de Freitas Bezerra Marujo**

Título: "GAP FILLING OF OPTICAL REMOTE SENSING MULTI-SOURCE DATA CUBE THROUGH MULTI-SCALE AND MULTI-TEMPORAL SEGMENTATION"

Aprovado (a) pela Banca Examinadora em cumprimento ao requisito exigido para obtenção do Título de **Doutor(a)** em

Computação Aplicada

Dr.   Rafael Duarte Coelho dos Santos

Presidente / INPE / SJCampos - SP

( ) Participação por Video - Conferência

(x) Aprovado   ( ) Reprovado

Dra.   Leila Maria Garcia Fonseca

Orientador(a) / INPE / SJCampos - SP

( ) Participação por Video - Conferência

(✓) Aprovado   ( ) Reprovado

Dr.   Sidnei João Siqueira Sant'Anna

Membro da Banca / INPE / São José dos Campos - SP

( ) Participação por Video - Conferência

(x) Aprovado   ( ) Reprovado

Dr.   Thales Sehn Körting

Membro da Banca / INPE / São José dos Campos - SP

( ) Participação por Video - Conferência

(x) Aprovado   ( ) Reprovado

Dr.   Giovanni de Araujo Boggione

Convidado(a) / IFG / Goiania - GO

( ) Participação por Video - Conferência

(x) Aprovado   ( ) Reprovado

Dra.   Silvia Helena Modenese Gorla da Silva

Convidado(a) / UNESP / São Paulo - SP

( ) Participação por Video - Conferência

(x) Aprovado   ( ) Reprovado

Este trabalho foi aprovado por:

( ) maioria simples

(x) unanimidade

São José dos Campos, 27 de março de 2019

*To my sister **Renata**, my brother **Rafael**, my girlfriend **Leticia**, to all my friends and mainly in memory of my mother **Elizete** and my uncle **Marcos**.*

ACKNOWLEDGEMENTS

ABSTRACT

A promising solution to solve the lack of Earth's surface observation problem on multi-spectral images consists in integrating multi-sensor data. However data must be harmonized before its measures can be comparable and a treatment for gaps (due to cloud cover, sensor defects, and partial images) must be considered. In this context, the present research proposes a methodology to build a gap-free multi-source and multi-spectral data cube, which involves Earth Observation data harmonization and reconstruction. To accomplish this, we tested two harmonization procedures, one based on linear regression and the other based on linear unmixing model, and propose a procedure for spatial-temporal gap-filling, which does not require previous reference. Two approaches for filling gaps are developed. The first one aims at improving a method based on spatial context of close-in-time images to fill small clouds and stripe effects, where in our adaptation a weighting factor is used for each pixel within segments. The second one uses a multi-temporal segmentation to fill the remaining gaps. The gap-filling strategies are applied on two image data cubes composed by Landsat-7/ETM+, Landsat-8/OLI images and CBERS-4/MUX images. To validate the gap-filling procedure, we simulate artificial gaps in the images and, subsequently we compare the original image with the gap-filled ones. Our approach based on weighting factor surpassed the original method for all bands, presenting R^2 greater than 0.90 and a VIF of at least 0.97, while asymptotically maintaining the algorithm cost. It also preserved the texture on reconstructed images, and also was capable of detecting narrow features, e.g., roads, riparian areas, and small streams. The second approach based on multi-temporal segmentation filled all the remaining gaps, 43.64% of the entire data cube. However, the estimated values are more affected by uncertainty and the image texture is affected, resulting in a homogeneous gap-filling. The harmonized and reconstructed areas were very similar to the original data, presenting an $UIQI$ of at least 0.92 and a VIF ranging from 0.6 to 0.7 on the final method, showing the feasibility of the methodology.

Keywords: Time series analysis. Multi-source. Data cube. Gap-filling. Segmentation.

PREENCHIMENTO DE LACUNAS EM CUBO DE DADOS DE SENSORIAMENTO REMOTO ÓTICO MULTIFONTE POR MEIO DE SEGMENTAÇÃO MULTINÍVEL E SEGMENTAÇÃO MULTITEMPORAL

RESUMO

Uma solução promissora para suprimir a ausência de dados de observações da Terra em imagens multi-espectrais, devido principalmente pela presença de nuvens, sombra de nuvens, defeitos na aquisição de dados e imagens parciais, tem sido a integração de dados multi-sensor. Contudo, deve-se harmonizar os dados provenientes de diferentes sensores para que estes possam ser comparáveis entre sí, além de que, lacunas de dados devem ser consideradas. Neste contexto, na presente pesquisa propõe-se um procedimento para construir um cubo de dados multispectral, multifonte e livre de lacunas, que envolve harmonização e reconstrução de dados da superfície terrestre. Para tanto, foram testados dois procedimentos de harmonização, um baseado em regressão linear e o segundo baseado em modelo linear de mistura espectral. Além disso, propoe-se um procedimento espaço-temporal para preenchimento de lacunas que não requer referência prévia da área. Foram desenvolvidas duas abordagens para preenchimento de lacunas, aplicadas serialmente. A primeira abordagem visa aprimorar um método baseado no contexto espacial para preencher lacunas oriundas de pequenas nuvens e defeitos do sensor Landsat-7/ETM+. A segunda abordagem de preenchimento de lacunas utiliza regiões homogêneas obtidas por meio de segmentação multitemporal para preencher as lacunas restantes do cubo de dados. As estratégias de preenchimento de lacunas são aplicadas em dois cubos de dados de imagem em duas áreas de estudo. Um cubo foi gerado a partir de um conjunto de dados composto por imagens Landsat-7/ETM+ e Landsat-8/OLI, e o segundo incluindo também imagens CBERS-4/MUX neste conjunto de dados. Para validar o procedimento de preenchimento de lacunas, foram simuladas lacunas artificiais nas imagens e, posteriormente, comparou-se as imagens originais com as imagens preenchidas. A abordagem baseada no fator de ponderação superou o método original para todas as bandas e apresentou R^2 maior que 0,90 e um VIF com valores superiores a 0,97, enquanto manteve assintóticamente o custo computacional do algoritmo. As imagens resultantes utilizando o método proposto tiveram sua textura preservada, além de também ser capaz de detectar características estreitas nelas, por exemplo, estradas, áreas ribeirinhas e pequenos riachos. A segunda abordagem baseada na segmentação multitemporal, preencheu as lacunas restantes, um total de 43,64% de todo o cubo de dados. No entanto, os resultados obtidos nesta abordagem foram mais incertos e a textura das áreas estimadas é afetada, resultando em um preenchimento homogêneo. As áreas resultantes no processo de harmonização e reconstrução apresentaram-se bastante similares as originais, apresentando um $UIQI$ de pelo menos 0,92 e VIF variando entre 0,6 e 0,7, demonstrando a viabilidade da metodologia.

Palavras-chave: Análise de Séries Temporais. Sensoriamento Remoto Multifonte. Cubo de dados. Preenchimento de lacunas. Segmentação.

LIST OF FIGURES

LIST OF TABLES

xv

LIST OF ABBREVIATIONS

6S	–	Second simulation of a satellite signal in the solar spectrum
AGDC	–	Australian Geoscience Data Cube
ARL	–	Application Readiness Levels
ARD	–	Analysis Ready Data
CBERS	–	China–Brazil Earth Resources Satellite program
CCD	–	High Resolution CCD Camera
CEOS	–	Committee on Earth Observation Satellites
CSIRO	–	Commonwealth Scientific and Industrial Research Organization
DTW	–	Dynamic Time Warpin
ETM+	–	Enhanced Thematic Mapper Plus
EROS	–	Earth Resources Observation and Science
ESPA	–	EROS Science Processing Architecture
GLS	–	Global Land Survey
HLS	–	Harmonized Landsat Sentinel
HOT	–	Haze Optimized Transformation
IBGE	–	Instituto Brasileiro de Geografia e Estatística
LaSRC	–	Landsat-8 Surface Reflectance Code
LEDAPS	–	Landsat Ecosystem Disturbance Adaptive Processing System
MAE	–	Mean Absolute Error
MGRS	–	Military Grid Reference System
MODIS	–	MODerate resolution Imaging Spectroradiometer
MODTRAN	–	Moderate resolution atmospheric transmission
NCI	–	National Computational Infrastructure
NDVI	–	Normalized difference vegetation index
NIR	–	Near Infrared
NMAE	–	Normalized Mean Absolute Error
NRMSE	–	Normalized Root Mean Square Error
OLI	–	Operational Land Imager
RS	–	Remote Sensing
RMSE	–	Root Mean Square Error
SLC	–	Scan Line Corrector
SWIR	–	Shortwave Infrared
TIR	–	Thermal Infrared
TOA	–	Top of Atmosphere
UIQI	–	Universal Image Quality Index
USGS	–	United States Geological Survey
VIF	–	Visual Information Fidelity
WI	–	Whiteness Index
WRS	–	Worldwide Reference System

CONTENTS

1 INTRODUCTION

Satellite remote sensing instruments are one of the most valuable tools available for understanding and monitoring changes occurring in land, coastal and oceanic ecosystems. Several remote sensing applications, such as agricultural monitoring and crop types mapping (BENDINI et al., 2017; MARUJO et al., 2017d), need a great amount of images acquired in different times and free of clouds to provide timely information on dynamic changes (KUENZER et al., 2015).

A wide range of satellite-borne instruments are currently in operation and some of them are freely available on the internet. The *Brazilian National Institute for Space Research* (INPE) pioneered the free provision of medium resolution satellite data, releasing images at no cost from the second *China-Brazil Earth Resources Satellite* (CBERS-2) (BANSKOTA et al., 2014). The adoption of this policy encouraged the *United States Geological Survey* (USGS) to make Landsat data available in 2008 (WOODCOCK et al., 2008; BANSKOTA et al., 2014), which resulted in a greater amount of access and use of orbital images (WULDER et al., 2012). Also the European Copernicus program (BERGER et al., 2012) made available the access to all users for Sentinel data, such as Sentinel-2A and Sentinel-2B, which have been used in various earth observation applications. The free data approach persists to recent days with free data availability from CBERS-4, Landsat-7, Landsat-8, MODIS, Sentinel-2, and other sensors.

Orbital sensors with high spatial resolution capture information from the Earth's surface in more detail than lower spatial resolution sensors (EHLERS et al., 2002). However, there is a compromise between the spatial, radiometric and temporal resolution characteristics of the sensor (LEFSKY; COHEN, 2003). Medium spatial resolution sensors, which range from 10 to 50 m (EHLERS et al., 2002), generate intermediary data that suppress the spatial and temporal resolutions trade-off, since this category of sensors can provide images with more spatial details than low spatial resolution sensors and can revisit a place to acquire images faster than high spatial resolution sensors.

Traditional change detection methods normally do not take advantage of the full potential of historical series (temporal trajectory analysis), since these methods use few images to map the Earth's surface, normally a bi-temporal change detection (COPPIN et al., 2004). In this context, time series of orbital images can provide a set of information and patterns that cannot be found in single time observations, e.g. as trends and periodicities (EHLERS, 2009). Because of that, the development of

techniques that fully incorporate the temporal dimension remains an area of intense research (GÓMEZ et al., 2016).

The concept of having multiple images of the same location, from different dates, grouped in a single multi-dimensional array is known as an image data cube. Integrating spectral and spatial information with the time component provides rich information to detail the space variations over time (PETITJEAN et al., 2012). However, the absence of Earth's surface observations, illustrated in Figure 1.1, due to cloud presence, low temporal resolution and sensor defects (e.g. stripe gaps in Landsat-7 images) can limit the full exploitation of time series (VUOLO et al., 2017). Also in this context, a characteristic in orbital images is that when the tile is located in the bordering path/row regions partial images occur.

Figure 1.1 - Types of spatial image gaps.

Illustration of the main radiometric problems occurring when working with satellite data. The first image illustrates the presence of clouds, which affects the surface observation by optical sensors. The second image illustrates the Landsat-7/ETM+ Scan Line Corrector (SLC) failure, which implies in stripes of missing data. The third image corresponds to partial images, which occurs on the path/rows borders.

Source: Adapted from Vuolo et al. (2017).

Considering the possibility of data absence, it is important to develop tools capable of reconstructing Earth Observation (EO) data, removing null observations, also know as gaps, and estimating close-to-reality values to fill the gaps. Reconstruction of EO data to obtain images without gaps, remains a challenge, nevertheless some studies have been developed to solve these problems (MAXWELL, 2004; MAXWELL et al., 2007; VUOLO et al., 2017).

Compared to the past years, nowadays there are more EO sensors available than ever, as shown in Figure 1.2. Shen et al. (2016) have pointed out that multi-source data is promising to complement EO data. However, since multi-source data differs in spatial, angular, spectral and temporal characteristics (SAMAIN et al., 2005), image processing techniques are needed to standardize distinct sensor data so it can be integrated (HOLDEN; WOODCOCK, 2016; ROY et al., 2016). We also have to consider that even sensors having correlating bandwidths their Spectral Response Function profiles can present significant differences (PINTO et al., 2016). In this context, products that are gridded to a common pixel resolution, map projection, and spatial extent (i.e., tile); atmospherically corrected and cloud masked to surface reflectance; normalized to a common nadir view geometry and adjusted to represent similar spectral responses are also called harmonized (CLAVERIE et al., 2018).

Figure 1.2 - Timelines of optical, including multispectral, earth observation satellites from 1972 to 2015.
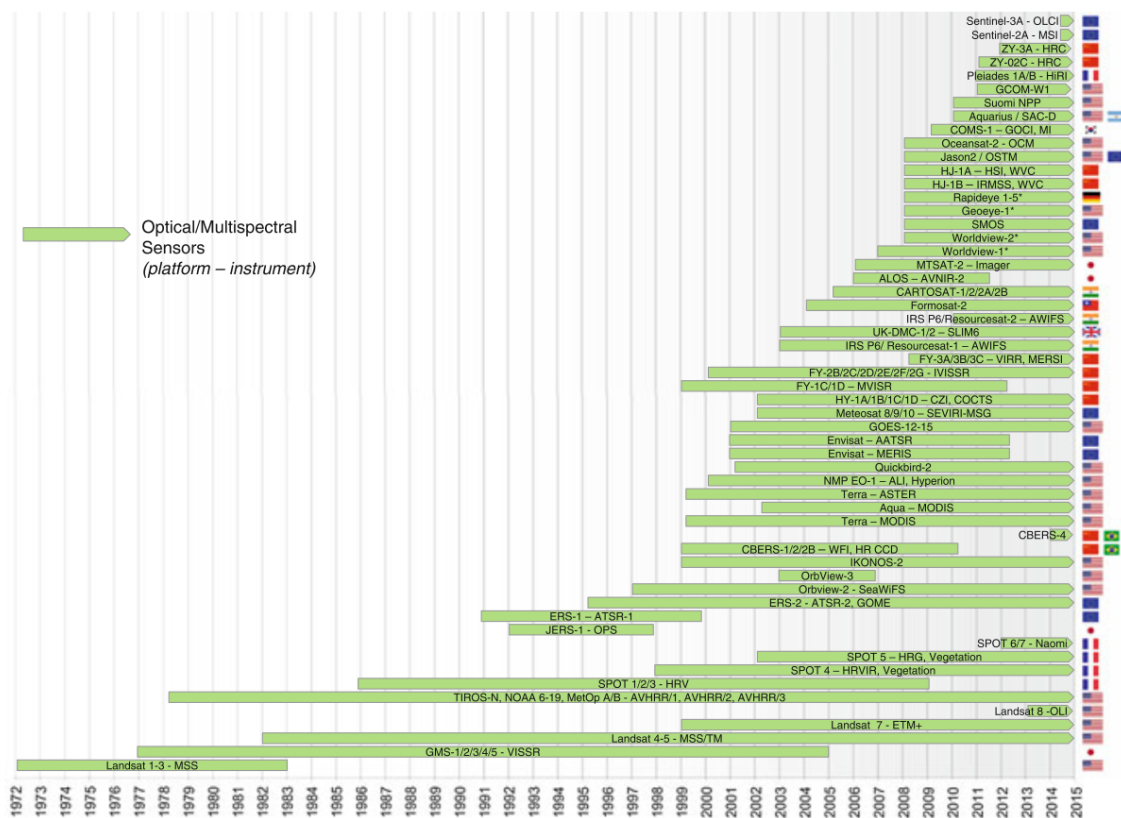
Visual timeline from 1972 to 2015 of the optical observation satellites, illustrating that nowadays the number of imaging sensors is bigger than ever.

Source: Kuenzer et al. (2015).

Therefore, the harmonization of multi-source orbital images is a crucial processing step to generate gap-free time series. Although the EO data reconstruction is an open problem (WULDER et al., 2015), attempts have been undertaken to harmonize data from multiple sources, including vegetation index intercalibration (TRISHCHENKO et al., 2002; STEVEN et al., 2003), reflectance fusion between medium and coarse images (GAO et al., 2006), linear spectral unmixing (AMORÓS-LÓPEZ et al., 2013; GEVAERT; GARCÍA-HARO, 2015) and bias adjustment (PINTO et al., 2016; ROY et al., 2016; HOLDEN; WOODCOCK, 2016).

Wulder et al. (2015) have categorized the use of multiple sensors in three types of virtual constellations according to "Application Readiness Levels" (ARL): (*i*) ARL-1, which combine sensors whose data are incompatible due to different measurements principles (e.g. passive and active systems), and (*ii*) ARL-2, which combine sensors that share a common measurement principle, e.g. reflectance estimation, however data transformation may be required depending on the sensors characteristics. (*iii*) ARL-3, which combine sensors with similar spatial and similar spectral characteristics, e.g. Landsat-7/ETM+, Landsat-8/OLI and CBERS-4/MUX with minimal processing requirements.

Also according to Wulder et al. (2015) and regarding the ARL-3 category, very few Earth-observation systems, apart from Landsat, independently meet the requirements that are essential for mapping sensors, specifically: a systematic acquisition strategy, consistent and calibrated radiometric quality, and long-term global archives. One of the few cases is CBERS program.

Considering that nowadays Landsat-8/OLI, Landsat-7/ETM+ and CBERS-4/MUX are in operation and the sensors present similar spectral bands (visible and near-infrared), similar spatial resolution (30 and 20m) and acquisition geometry, with a minimal spectral alignment and spatial resampling, CBERS-4/MUX data can be used to build a virtual constellation alongside Landsat data and increase its temporal resolution. Besides, we can also take into consideration other two points as hypotheses to develop our work: (1) Landsat-8/OLI images can be used as reference to spectrally harmonize Landsat-7/ETM+ and CBERS-4/MUX data, and (2) image processing techniques can be used to reconstruct EO data to integrate a gap-free multi-source optical remote sensing image data cube and, therefore, overcome the lack of Earth surface observations in time series.

Within this perspective, the objective of this work is to propose a procedure to build a gap-free multi-spectral data cube, which involves various processing tech-

niques including EO data harmonization and reconstruction of missing EO data. To accomplish this, we tested two spectral harmonization methods, one based on linear regression and the other based on linear unmixing model. Once images were harmonized, we developed a method for gap-filling imagery from Landsat-8/OLI, Landsat-7/ETM+ and CBERS-4/MUX sensors based on spatial and temporal context without requiring previous reference of the area. Two approaches for filling gaps due primarily to cloud cover, sensor defects and partial images are developed. The first improves a method proposed in the literature that uses spatial context of close-in-time images to fill small gaps (small clouds and strips defects). It uses the most frequent value within segments obtained in a multi-scale segmentation to fill the gaps. The second one uses time series matching and homogeneous regions obtained through a multi-temporal segmentation to estimate missing data. The gap-filling strategies are applied on two image data cubes: one generated from Landsat-7 and Landsat-8 images, and the second one including also CBERS-4/MUX images in dataset. To validate the method, we simulate artificial gaps in images and then compare the original image with the gap-filling one.

In summary, this work contributions reach optical multi-source harmonization, innovative gap-filling of remote sensing images and the building of remote sensing image data cubes. The harmonization processes tested are based on linear regression and linear unmixing model. The gap-filling procedure includes estimation of small gaps, such as Landsat-7/ETM+ stripes, through a multi-scale segmentation and estimation of larger gaps through multi-temporal segmentation. Unifying the mentioned techniques a remote sensing image data cube is built.

1.1 Organization

The remaining chapters of this thesis are organized as follow:

- Chapter 2: presents a discussion on the main concepts of remote sensing, multi-source approaches, image segmentation, time series, Analysis Ready Data, EO data reconstruction and some considerations regarding data provenance.

- Chapter 3: presents a detailed description of the proposed methodology, tests and a study cases.

- Chapter 4: presents the main results obtained in this work, based on the proposed methodology.

- Chapter 5: presents considerations about the experimental results, conclusions, as well as suggestions for future works.

2 REVIEW

2.1 Optical Remote Sensing

According to Jensen (2007), the main components of a multispectral sensors are the radiation detectors, with different wavelength band sensitivity, and the necessary hardware. The digital data acquired by these sensors are normally stored as numeric matrices. Each value in the matrix, called Digital Number (DN), is located in a row and a column. The DN values range in an digital image is limited by the radiometric resolution of the sensor, normally set as a number of bits. For instance, the radiometric resolution of a sensor an image quantized in 8 bits will present values in the range from 0 to 255.

A pixel (picture element) is the smallest element in a digital image. In the context of Remote Sensing (RS) systems, each pixel represents the spectral response of a specific Earth's surface area measured by a sensor. This area size is related to the sensor spatial resolution, the measure of the smallest object that can be resolved by the sensor, stated in metres.

Since each detector has its own wavelength sensitivity, a data set can be composed by a countable number of bands, presenting specific bright for each spectral band (JENSEN, 2007). The number of bands (intervals) a sensor has and these bands wavelength characterize its spectral resolution (JENSEN, 2007, Chapter 1). Satellites constructed for resources monitoring normally are Sun-synchronous in order to assure similar conditions during a subsequent image of the same area. Sensor revisit time is called temporal resolution.

Each sensor has its own radiometric, spatial, spectral and temporal characteristics. Landsat program provides the most faraway orbital image series, providing observations since 1972 and is freely available (COHEN; GOWARD, 2004). Landsat-8 Operational Land Imager (OLI) and Landsat-7 Enhanced Thematic Mapper Plus (ETM+) are still operational, acquiring images, even with ETM+ limitations due to a defect on the Scan Line Corrector (STOREY et al., 2005; MAXWELL, 2004). CBERS program also provides freely available images,

CBERS-4 was launched in December 2014, and it is in operation. CBERS-4 carries a Multispectral Camera (MUX), which is very similar to Landsat-7/ETM+ with 20m of spatial resolution. Table 2.1 presents some characteristics for Landsat-7/ETM+, Landsat-8/OLI and CBERS-4/MUX. These three satellites have been used in several

EO studies (WULDER et al., 2015; WULDER et al., 2016; TOTH; JÓŹKÓW, 2016).

Table 2.1 - Landsat-7/ETM+, Landsat-8/OLI and CBERS-4/MUX specifications.

		Satellite/Sensor		
		Landsat-7/ETM+	Landsat-8/OLI	CBERS-4/MUX
Spectral Bands (µm)	Coastal		0.433 − 0.453	
	Blue	0.45-0.52	0.450–0.515	0.45-0.52
	Green	0.53-0.61	0.525–0.600	0.52-0.59
	Red	0.62-0.69	0.630–0.680	0.63-0.69
	NIR	0.78-0.91	0.845–0.885	0.77-0.89
	Swir1	1.57-1.78	1.560–1.660	
	Swir2	2.08-2.35	2.100–2.300	
	Pan	0.52-0.90	0.500–0.680	
	Cirrus		1.36–1.39	
	TIRS1	10.42-12.50	10.6-11.19	
	TIRS2		11.5-12.51	
Spatial Resolution (m)		30	30	20
Swath Width (km)		185	185	120
Orbit Height (km)		705	705	778
Inclination (degree)		98.2	98.2	98.5
Temporal Resolution (days)		16	16	16

2.1.1 Preprocessing

Images acquired by orbital sensors suffer from distortions caused by sensor, solar, atmospheric, and topographic interactions (JENSEN, 2007). Therefore, it is necessary to preprocess the images to correct various effects due to geometric mismatches, cloud, cloud shadow, snow and atmosphere.

2.1.1.1 Geometric Corrections

The most common geometric corrections in an image is registration (YOUNG et al., 2017). Image registration is a digital image processing technique that precisely aligns two or more targets. In other words, it lines up images so that an object has the same position in both images (FONSECA; MANJUNATH, 1996; SUNDARESAN et al., 2007).

The registration technique normally consists of the following four steps (ZITOVÁ; FLUSSER, 2003): (*i*) feature detection; (*ii*) feature matching; (*iii*) transform model estimation; and (*iv*) image resampling and transformation. In the feature detection

step, salient and distinctive objects in the image (closed-boundary regions, edges, contours, line intersections, corners, etc.) are selected. In the feature matching process, the correspondence between the features detected in the sensed image and those detected in the reference image is established. Next, in the model estimation, the type and parameters of the so-called mapping functions, aligning the sensed image with the reference image, are estimated. Finally, the sensed image is transformed by means of the mapping functions. Image values in non-integer coordinates are computed by the appropriate interpolation technique.

In recent years, many automated registration methods have been proposed (ZITOVÁ; FLUSSER, 2003; LE MOIGNE et al., 2010; DALMIYA; DHARUN, 2015). However, specifically for multi-temporal applications, factors such as different illumination conditions (annual and seasonal variations) and noise, which implies image intensity variations, must be considered in the geometric model (BEHLING et al., 2014; SEDAGHAT; EBADI, 2015; GU et al., 2016). When considering multi-source data, the registration method also must be capable to dealing with differences in the spatial, spectral and radiometric resolution (GU et al., 2016).

In this context, Behling et al. (2014) proposed a methodology to fully register multi-source and multi-temporal data. The method is based on the assumption that the orthorectified standard data products of the various sensors only differ by constant spatial offsets, which can be corrected by applying image-specific shifts. The authors registered 26 years of Landsat (TM and ETM+), ASTER, SPOT and RapidEye sensors data, with spatial resolution ranging from 5 to 400m, resulting in an absolute accuracy of 23m Root Mean Square Error (RMSE). A sensor-internal coregistration is performed to obtain the high-accuracy spatial fit between datasets of the same sensor avoiding the uncertainties that get introduced by the co-registration of individual images to a spatial reference of a largely differing spatial resolution.

The higher spatial resolution dataset is downsampled to the lower resolution one. Then, using a moving windows of 51x51 pixels, the correlation process is applied on red and Near infrared (NIR) bands and repeated, until 100 tie points are identified per image pair or 10% of all image pixels have been checked. After the removal of outliers, the tie points are used to model the distortion, which is applied to correct all dataset.

2.1.1.2 Radiometric Correction

Radiance ($W \cdot m^{-2} \cdot sr^{-1}$) is the energy emitted by a surface into a unit solid angle, in a specific direction, by a unit projected area, over a unit wavelength interval (JENSEN, 2007, Chapter 2). Reflectance is a unitless measure of the ratio of radiation reflected by an object relative to the radiation incident upon the object (YOUNG et al., 2017).

Different surfaces interact with the Sun's electromagnetic radiation in distinct ways. The reflectance of an object is dependent on the material's physical composition, its roughness and geometric circumstances. Values obtained from absolute radiometric correction, e.g. surface reflectance and land surface temperature, are better suited for comparing across images than radiance discrete values (YOUNG et al., 2017).

Each sensor records signals that are stored as DN's according to the sensor radiometric resolution and after a few preprocessing these signals can be used to estimate reflectance values. The DN's are calibrated to radiance values according to the sensor specific gains and offsets coefficients in each spectral band. This relation may be established following (PINTO et al., 2016):.

$$L_i = G_i \times DN_i + offset_i, \tag{2.1}$$

where L_i is the top of atmosphere radiance at band i ($W \cdot m^{-2} \cdot sr^{-1}$), DN_i is the digital number from the image at band i, G_i is the coefficient gain for band i ($W \cdot m^{-2} \cdot sr^{-1}$) and $offset_i$ is the coefficient bias for band i ($W \cdot m^{-2} \cdot sr^{-1}$).

After a solar-effects correction, data can be converted from at-sensor spectral radiance into top of atmosphere (ToA) reflectance. According to Chander et al. (2009), there are some advantages in using ToA reflectance instead of at-sensor spectral radiance when comparing images from different sensors: the cosine effect of different solar zenith angles due to the time difference between data acquisitions is removed; different values of the exoatmospheric solar irradiance arising from spectral band differences are compensated; and the variation in the Earth-Sun distance between different data acquisition dates are corrected. The ToA radiance can be converted to planetary ToA reflectance data as:

$$\rho\lambda = \frac{\pi \cdot L_\lambda \cdot d^2}{E_{SUN_\lambda} \cdot \cos\theta_z}, \tag{2.2}$$

where $\rho\lambda$ is the planetary ToA reflectance (unitless), π is the mathematical constant (unitless), L_λ is the spectral radiance at the sensor's aperture ($W \cdot m^{-2} \cdot sr^{-1}$), d is the Earth-Sun distance (astronomical units), θ_z is the solar zenith angle (degrees or radians), and $E_{SUN_\lambda} \cdot \cos\theta_z$ is mean exoatmospheric solar irradiance ($W \cdot m^{-2}$) (CHANDER et al., 2009).

Chander et al. (2009) provides a table containing values of the Earth-Sun distance for each day of the year. Since the exoatmospheric solar irradiance is dependent to each sensor, Pinto et al. (2016) estimated its value for MUX and WFI on-board CBERS-4. Using those parameters alongside the solar elevation, which are individual to each image, it is possible to convert it into ToA Reflectance.

Atmospheric conditions and different illumination caused by the solar position and terrain slope may cause undesired artifacts in RS images (PONS et al., 2014). The atmospheric correction is a radiometric correction that uses the ToA reflectance and a radiative transfer model alongside the atmosphere conditions to estimate surface reflectance values. The most commonly used models are the *Second Simulation of a Satellite Signal in the Solar Spectrum* (6S) and the *Moderate resolution atmospheric Transmission* (MODTRAN) (CALLIECO; DELL'ACQUA, 2011).

The USGS *EROS Science Processing Architecture* (ESPA) provides surface reflectance products for Landsat-7/ETM+ and Landsat-8/OLI (UNITED STATES GEOLOGICAL SURVEY - USGS, 2017e). The product for both sensors uses the 6S radiation propagation model through the *Landsat Ecosystem Disturbance Adaptive Processing System* (LEDAPS) (UNITED STATES GEOLOGICAL SURVEY - USGS, 2017c) and *Landsat 8 Surface Reflectance Code* (LaSRC) (UNITED STATES GEOLOGICAL SURVEY - USGS, 2017d) algorithms, respectively (UNITED STATES GEOLOGICAL SURVEY - USGS, 2017e), while for MODTRAN there is an ENVI software plugin (ENVI, 2009).

2.1.2 Cloud Detection

Optical RS images are vulnerable to the occurrence of clouds, since clouds and cloud shadows affect the surface radiometric response (JENSEN, 2007). The white color appearance of clouds in the satellite images, can be determined by the additive effect of all wavelengths of the visible spectrum (POLIDORIO et al., 2005).

Methods for detecting clouds and cloud shadows in scenes that present water bodies and bare soil, using only sensor spectral responses, may not work properly. This is due to the low reflectance on water bodies that results in similar spectral charac-

teristics in areas affected by shadows and to the high reflectance on bare soil that present similar behavior as exhibited by clouds (ABREU et al., 2013).

Recent methods such as the *Function of Mask* (Fmask) algorithm (ZHU; WOODCOCK, 2012; ZHU et al., 2015), uses ToA reflectance and Brightness Temperature data as inputs to provide a cloud and cloud shadow mask. USGS uses this method as standard cloud mask for Landsat-7 and an enhanced version for Landsat-8 (UNITED STATES GEOLOGICAL SURVEY - USGS, 2015).

First, Fmask separates potential cloud pixels and clear-sky pixels. Then, the thermal bands are used to produce a probability mask for clouds over land and water separately. This probability mask for clouds is combined with the potential cloud pixels and a potential cloud layer is derived (ZHU; WOODCOCK, 2012; ZHU et al., 2015). To detect cloud shadows, a mask of dark pixels is extracted by thresholding the NIR band, then a prediction of possible cloud shadow locations is done using the view angle of the satellite sensor and the illuminating angle. The areas with maximum similarity to potential cloud shadow mask are labeled as cloud shadow (ZHU; WOODCOCK, 2012).

Regarding sensors that do not have thermal spectral bands, Silva and Liporace (2016) proposed an adaption of the *Fmask* algorithm to ensure automatic detection of cloud and cloud shadow using visible and near infrared spectrum. Originally the methodology was proposed to be used on Amazonia-1/AWFI, but it can be applied in any similar sensor, such as CBERS-4/MUX (MARUJO et al., 2017c).

To identify clouds, Silva and Liporace (2016) used three indices threshold: *Normalized Difference Vegetation Index* (NDVI), *Whiteness Index* (WI) and *Haze Optimized Transformation* (HOT), respectively, described, by:

$$NDVI = \frac{NIR - Red}{NIR + Red},$$ (2.3)

where NIR is the Near Infrared band and Red is the red band.

$$WI = \sum_{i=1}^{3} \left| \frac{(B_i - M)}{M} \right|,$$ (2.4)

where B_i are the visible bands and M is the modified mean band value obtained through:

$$M = 0.25 \cdot Blue + 0.375 \cdot Green + 0.375 \cdot Red, \tag{2.5}$$

where $Blue$ is the blue band, $Green$ is the green band and Red is the red band.

$$HOT = Blue - 0.45 \cdot Red - 0.08, \tag{2.6}$$

where $Blue$ and Red are the blue and red bands. A diagram containing the cloud detection by thresholding can be visualized in Figure 2.1. The thresholding values varies from scene to scene and are determined by the interpreter.

Figure 2.1 - Cloud detection method through thresholding.
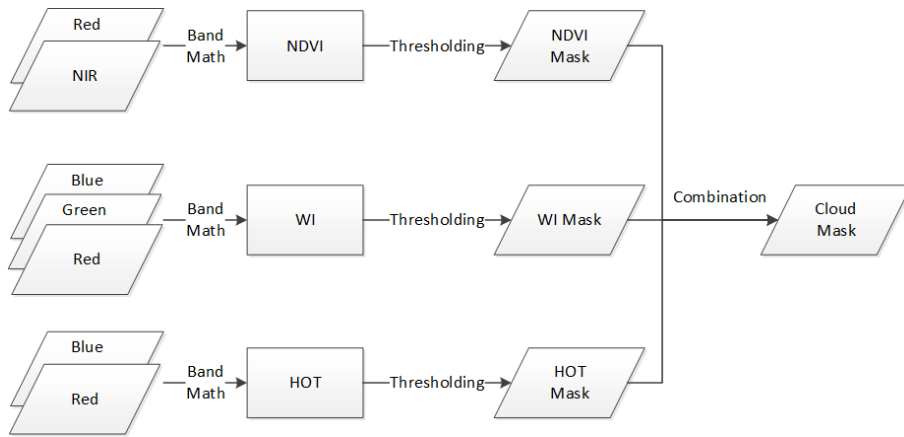
Silva and Liporace (2016) method to cloud detection through thresholding process. Spectral bands (Blue, Green, Red and NIR) are used to calculate Normalized Difference Vegetation Index (NDVI), Whiteness Index (WI) and Haze Optimized Transformation (HOT) to calculate a Cloud Mask by thresholding the indices and combining them using an *AND* operator.

Source: Author's production.

To detect cloud shadows, the authors performed a similar approach by combining a dark pixel mask, a water mask and a difference image. The dark pixel mask obtains candidate pixels, including false positives by thresholding the green and NIR bands, as demonstrated in:

$$D_2 = Green < (Green_{min} + \rho_{\lambda 2}), \tag{2.7}$$

where Green is the Green band; $Green_{min}$ is the least value found for the Green band; and $\rho_{\lambda 2}$ is reflectance threshold for the green band.

$$D_4 = NIR < (NIR_{min} + \rho_{\lambda 4}), \tag{2.8}$$

where NIR_{min} is the least value found for the NIR band; and $\rho_{\lambda 4}$ is reflectance threshold for the NIR band.

$$D = D_2 \, and \, D_4, \tag{2.9}$$

where D is the dark pixel mask, D_4 are the dark pixels obtained by Equation 2.7 and D_4 are the dark pixels obtained by Equation 2.8. Based on the same approach, the authors also built a water mask using the NIR band and the NDVI index. This approach is based on detecting water low response on the NIR band and separate water from soil using the NDVI. To do that, the authors detect and combine clean and turbid waters pixels, as can be seen in:

$$\begin{aligned} W = &((NDVI < NDVI_{clean}) \, and \, (B4 < \rho_{\lambda clean})) \, or \\ &((NDVI < NDVI_{turbid}) \, and \, (B4 < \rho_{\lambda turbid})), \end{aligned} \tag{2.10}$$

where $NDVI_{clean}$ is a NDVI threshold used to detect clean water; $B4$ is the NIR band; $\rho_{\lambda clean}$ is a NIR band threshold used to detect clean water; $NDVI_{turbid}$ is a NDVI threshold used to detect turbid water; $\rho_{\lambda turbid}$ is a NIR band threshold used to detect turbid water. The final mask, image difference, is used to minimize seasonal differences, assuming negative differences possible cloud shadows and positive differences as clouds. This mask is obtained by subtracting the target image by a reference image, as in:

$$Diff = B_4 - REFB_4, \tag{2.11}$$

where B_4 is the NIR band and $REFB_4$ is a NIR band reference without clouds. The

whole cloud shadow detection process can be visualized in Figure 2.2.

Figure 2.2 - Cloud shadow detection method through thresholding.
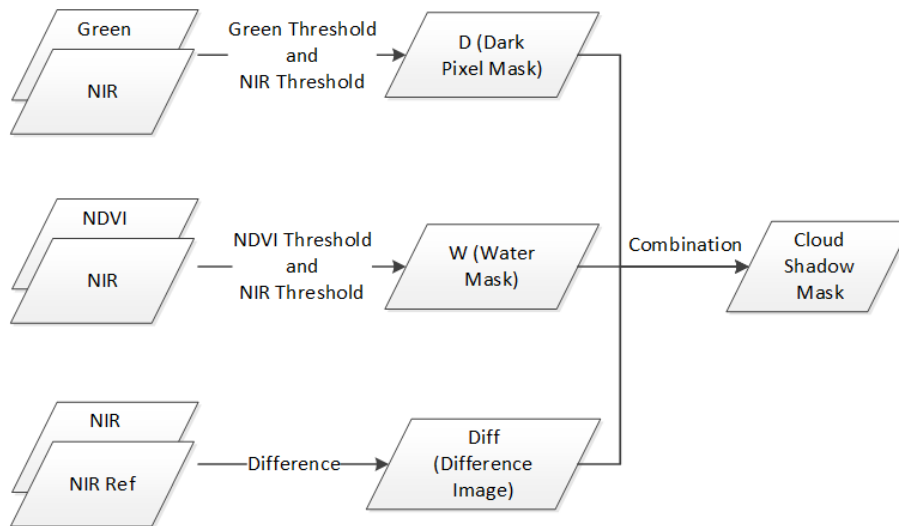
Silva and Liporace (2016) method to cloud shadow detection through thresholding process. Spectral bands (Red and NIR) are used alongside Normalized Difference Vegetation Index (NDVI) and a reference image NIR to calculate a dark pixel mask (D), water mask (W) and difference image (Diff) to calculate a Cloud Shadow Mask.

Source: Author's production.

Once preprocessed, RS images can be used in a variety of applications, e.g. crop monitoring (STEVEN et al., 2003) and change detection (COPPIN et al., 2004). In the past, these applications mainly used the spectral information alone, based on the pixel value of each band, while the spatial context was rarely considered (LI et al., 2014).

With the advance of the sensor spatial resolution, and considering that spectral-based methods did not provided satisfactory results, spatio-contextual information started to be incorporated into analyses (LI et al., 2014). However, change detection methods normally use few images, ranging from two to five images, to map the Earth's surface, and do not take advantage of the full potential of historical series (COPPIN et al., 2004). Hence, integrating the spectral and spatial information with the time component can provide rich information to detail the space variations over time (PETITJEAN et al., 2012).

2.2 Time series

Time series are sets of interdependent chronological observations that provide information and patterns that cannot be found in single time observations, such as trends and periodicities (EHLERS, 2009). Because of that, the development of techniques that fully incorporate the temporal dimension remains an area of intense research (GÓMEZ et al., 2016). In the RS context, time series can be extracted from a sequence of chronological images or field observations. MODIS (MODerate resolution Imaging Spectroradiometer) and Landsat are two of the most used data to extract time series (GÓMEZ et al., 2016). MODIS, on board Terra and Aqua platforms, temporal resolution, provides daily revisits, although its spatial resolution varies from 250m to 1km. Landsat program provides the most faraway orbital image series, providing observations since 1972 (COHEN; GOWARD, 2004). Nowadays, Landsat-7 and Landsat-8 are active, each one providing images with 30m of spatial resolution and 16 days of revisit time.

In time series observations, three factors are evident: (*i*) the order is crucial; (*ii*) the correlation has meaning; and (*iii*) cycles can be difficult to detect. Those characteristics make this type of data harder to analyze than singular time data and require specific statistical techniques (EHLERS, 2009). One of the main applications of RS time series is monitoring the changes on Earth's surface changes (GÓMEZ et al., 2016). For vegetation change detection, the reflectance (extracted from spectral bands) alongside the NDVI (ROUSE et al., 1974) and the EVI (HUETE et al., 1997) are extracted from image pixels or segments, in a same location and different dates, and used to compose a time series (GÓMEZ et al., 2016), as illustrated in Figure 2.3. Those values obtained through time represent time series and can represent a "phenology curve" when considering vegetation (BAUMANN et al., 2017).

Many approaches are used to deal with time series. Time series decomposition, for instance, supposes that a series is an additive or multiplicative aggregation of components: (*i*) the trend; (*ii*) the seasonality; and (*iii*) the residual components (VERBESSELT et al., 2010). In vegetation indices time series, for instance, the seasonality component may represent the vegetation vigor, the trend component relates to vegetation growth, degradation or stability over the years and the changes in remaining components may represent surface anisotropy, atmosphere effects, or sensor noise (KUENZER et al., 2015).

Integrating the spectral and spatial information with the time component, provides rich information to detail the space variations along the time (PETITJEAN et al.,

Figure 2.3 - Image time series extraction.
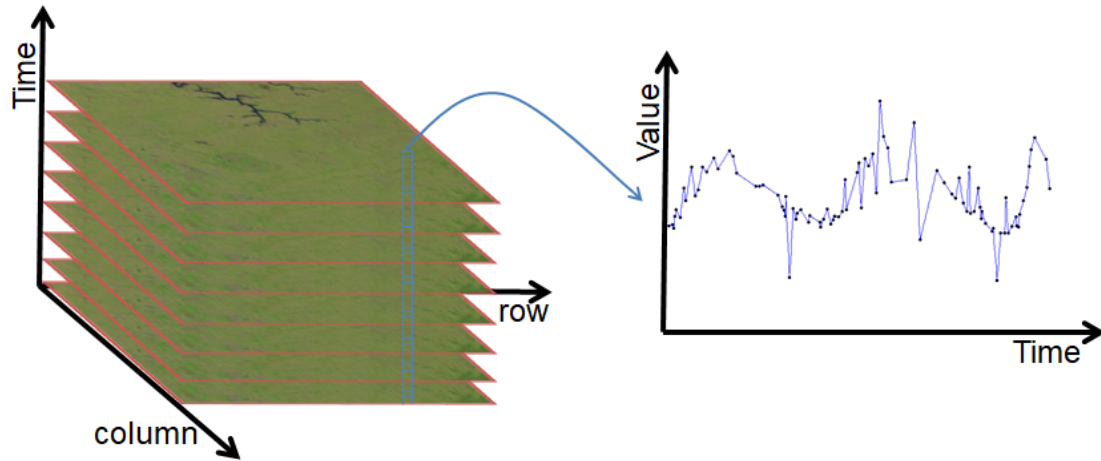
Extraction of the values of a time series (blue curve) from a stack of orbital images of the same location and different dates.

Source: Author's production.

2012). However, the absence of data, due to sensors failure or cloud presence still affects how precise a time series is. Based on that, another common approach used to deal with time series is smoothing algorithms (BENDINI et al., 2016; SHAO et al., 2016; VUOLO et al., 2017). The concept of time series smoothing is to obtain more consistent time series by reducing the effects of the residual component (KUENZER et al., 2015). However, it is important to emphasize that while reducing interference in the time series, most smoothing algorithms can change pixel values with useful information that had no noise influence (ERASMI et al., 2006).

Long term time series can be analyzed with respect to their daily, weekly, monthly, annual or decadal interval (KUENZER et al., 2015). Normally when referring to EO, this interval is defined by the sensor temporal resolution. In the context of vegetation analysis, one focus of time series analysis is on the extraction of phenology based on features, also called phenometrics (KUENZER et al., 2015). Many attempts have successfully exercised those metrics as classifying parameters in order to obtain land cover maps (ABREU et al., 2013; BENDINI et al., 2016; GÓMEZ et al., 2016).

Given the diverse applications and possibilities of analysis of time series, there is a demand for developing methods capable of extracting information from those series.

17

A promising method that has increasingly been used to classify RS time series is the Dynamic Time Warping (DTW) (BAUMANN et al., 2017).

2.2.1 Dynamic Time Warping

DTW method aims at finding an optimal global alignment between two data sequences, a minimal sum sequence without repeated elements that is called a warping path (MÜLLER, 2007). This method is based on Levenshtein's distance (LEVENSHTEIN, 1966) and was proposed by Sakoe and Chiba (1971) for speech recognition.

Basically, Levenshtein's distance between two strings is the least number of operations required to convert one string to another (PETITJEAN et al., 2012). DTW is a similarity measure that can compare time series and obtain details that can not be acquired by comparing using the Euclidean distance (PETITJEAN et al., 2012). In the context of time series classification using DTW, a known pattern is compared with an unknown time series in order to calculate an alignment and measure the two data similarity (BERNDT; CLIFFORD, 1994; PETITJEAN et al., 2012; MAUS et al., 2016b), as can be seen in Figure 2.4.

Figure 2.4 - Visual comparison between Euclidean distance and Dynamic Time Warping applied to time series.

Note that, while the two time series have an overall similar shape, they are not aligned in the time axis. Euclidean distance, which assumes the ith point in one sequence is aligned with the ith point in the other, will produce a pessimistic dissimilarity measure. The nonlinear dynamic time warped alignment allows a more intuitive distance measure to be calculated.

Source: Keogh and Ratanamahatana (2005).

Suppose we have two time series, Q and C, of lengths n and m, respectively, where $Q = (q_1, q_2, ..., q_n)$ and $C = (c_1, c_2, ..., c_m)$. To align these sequences using DTW, the first step consists in building an accumulated cost matrix $(n \times m)$, where the (i^{th}, j^{th}) element of the matrix contains the distance, $\delta(q_i, c_j)$, between the two points q_i and

c_j, where $i \in \{1, ..., n\}$ and $j \in \{1, ..., m\}$ (KEOGH; RATANAMAHATANA, 2005). As an example of the δ value, Maus et al. (2016a) used pixel value absolute difference from RS images as the metric. Based on that, when pixels present the same value, distance is 0 and increases according to the differences.

The accumulated cost matrix considers the lower left index as the initial element. This element is filled with the calculated δ between each series first value. Then the elements of the first row and the first column of the matrix are calculated, respectively, by:

$$D(1, c_j) = \delta(q_i, c_j) + D(1, c_{j-1}) \tag{2.12}$$

$$D(q_i, 1) = \delta(q_i, c_j) + D(q_{i-1}, 1) \tag{2.13}$$

After filling the first row and the first column, the values of the remaining elements are filled from left to right and from bottom to top as following equations:

$$D(Q_i, C_j) = \delta(q_i, c_j) + min \begin{Bmatrix} D(Q_{i-1}, C_{j-1}), \\ D(Q_i, C_{j-1}), \\ D(Q_{i-1}, C_j) \end{Bmatrix} \tag{2.14}$$

This process is represented in Figure 2.5.

Once completely filled, the accumulated cost matrix can be used to obtain an warping path. This path is calculated starting from the upper right element of the matrix summing always with the lowest value among the left, below and diagonal elements, as can be seen in Figure 2.6.

Following that, a warping path must respect three condition:

a) boundary: implies that a path should start and end on the matrix oppose diagonals;

b) monotonicity: the alignment path must preserve its direction or advance to the boundary direction;

c) step size: the alignment path must roam obeying neighborhood rules, in-

Figure 2.5 - Filling a DTW accumulated cost matrix example.
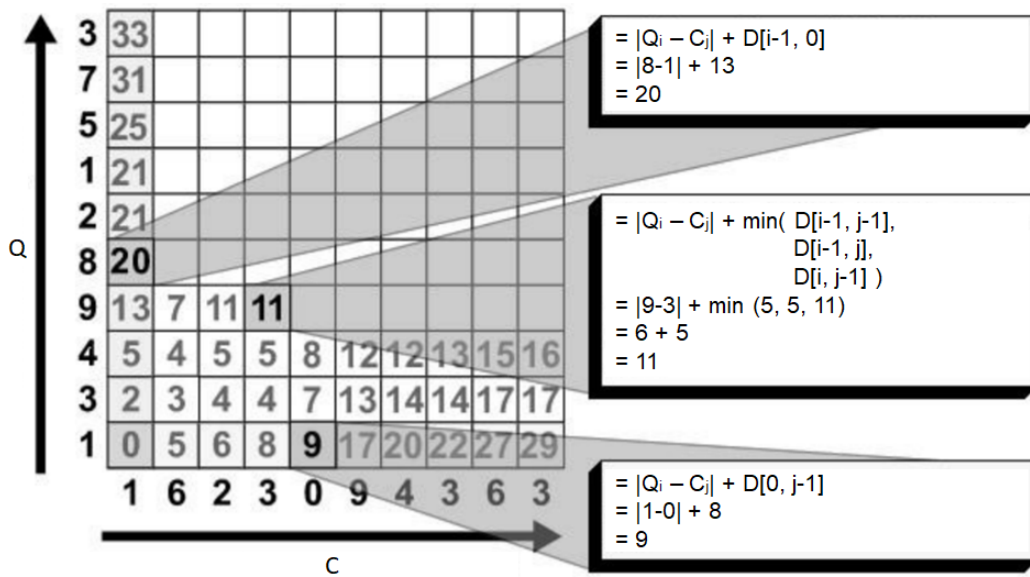
Example of how to fill a DTW accumulated cost matrix.
Source: Adapted from Souza et al. (2009).

cluding diagonal.

Considering two sequences Q of length $n = 9$ and a sequence C of length $m = 7$, as defined in Page 17, Figure 2.7 (a) shows an admissible warping path, while Figure 2.7 (b, c and d) shows cases in which theese conditions are broken.

Figure 2.6 - Warping path calculation example.
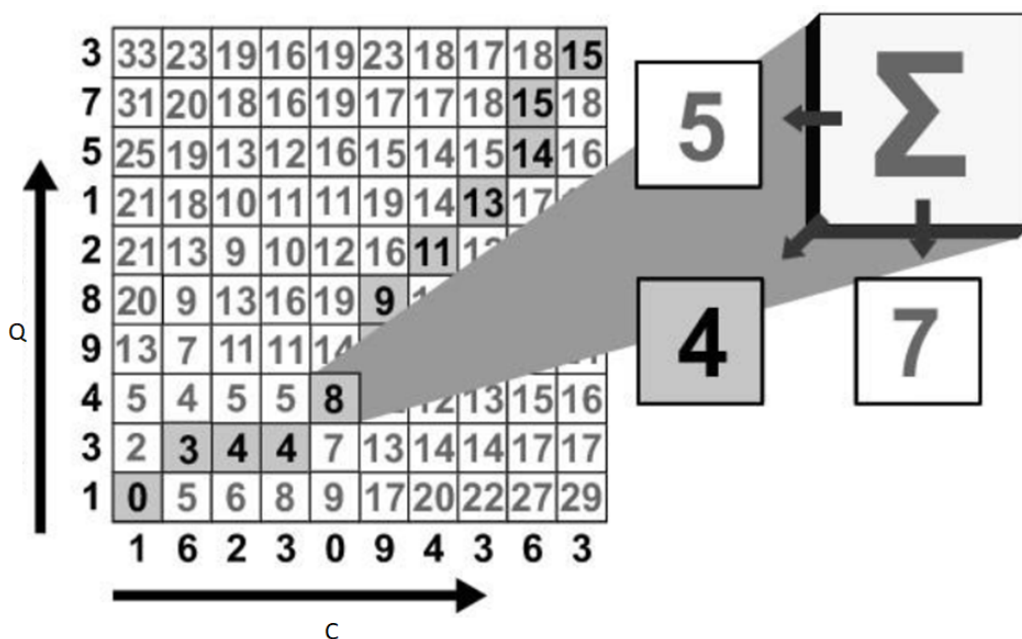
Example of how to calculate a warping path on an accumulated cost matrix.

Source: Adapted from Souza et al. (2009).

Figure 2.7 - DTW warping path conditions.
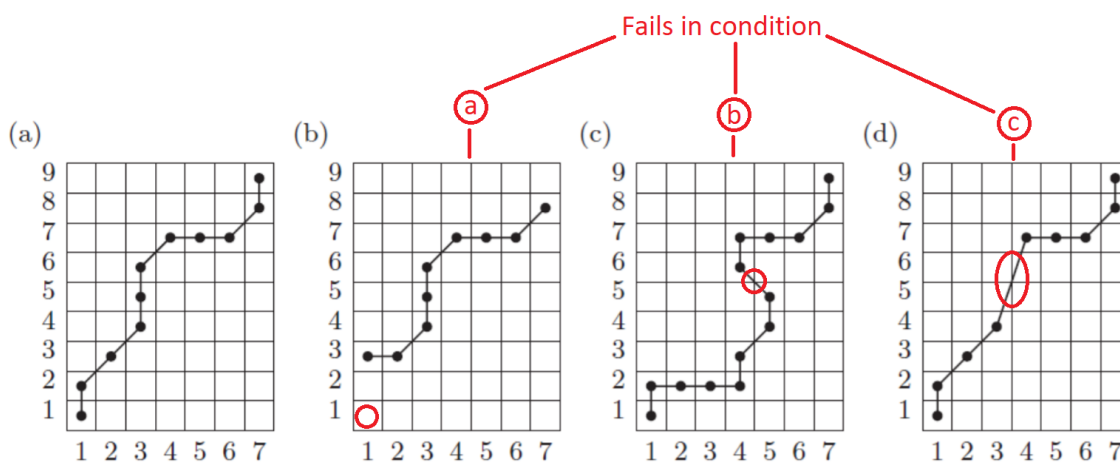
Illustration of paths of index pairs for some sequence. (a) Admissible warping path satisfying the boundary, monotonicity, step size conditions. (b) Boundary condition is violated. (c) Monotonicity condition is violated. (d) Step size condition is violated.

Source: Adapted from Müller (2007).

2.3   Image segmentation

Image segmentation is one of the most important technique in the image analyses. Image segmentation partitions an image into uniform regions or objects (GONZALEZ; WOODS, 2007, Chapter 10). As mentioned before, with the advance of spatial resolution in imaging sensors, spatio-contextual approaches have been more promising in differing Earth's surface objects than spectra-based approaches, since some land cover types cannot be effectively separated with spectral information, e.g., urban areas and bare soil (LI et al., 2014).

The segmentation enables images to be handled based on its regions instead of based on their pixel values. Segmentation methods are generally categorized in different approaches, e.g., histogram thresholding, edge-detection and region-growing (BLASCHKE et al., 2000). Several segmentation methods comparisons for RS applications have been published in the literature (BÉNIÉ et al., 1989; MEINEL et al., 2004). In optical RS, region-growing is the most employed approach, being multi-resolution segmentation (BAATZ; SCHÄPE, 2000), one of the most used algorithms.

Initially, the region-growing segmentation approach normally considers each pixel as a region. Interactively neighboring regions are compared through a homogeneity criterion, e.g. region pixel mean value, and merged if they are similar. Some region growing algorithms also implement a max size that each segment can reach. This is performed in order to limit segment area size, which implies in a stop on region-merging after a segment has a determined number of pixels (GONZALEZ; WOODS, 2007, Chapter 10). Region-growing algorithms input parameters, e.g. homogeneity criterion and minimum area size, are normally empirically set by an user, who tests several parameters values until a visually satisfactory result is found (ESPINDOLA, 2007). These parameters will interfere in the segmentation results. Hence, in order to result in a good segmentation they must be set according to the targets characteristics.

2.3.1   Multiresolution segmentation

Baatz and Schäpe (2000) proposed a segmentation method based on region-growing. The method is implemented in the commercial software *Definiens eCognition* (DEFINIENS IMAGING GMBH, 2002), and other implementations of the method in free libraries (KÖRTING et al., 2013). The method starts assuming a bottom-up approach, in which each image pixel is an object and if an homogeneity criterion is achieved, neighboring regions are merged into one larger object.

This homogeneity criterion is assigned to each possible merge, representing a "fusion factor". If the possible merge is smaller than the least fusion factor, the regions are merged and the process is repeated until there are no more possible merges. In order to find the best merging objects, a heuristic of *local mutual best fitting* is employed. In this heuristic, supposing an image object A, the neighbor object that best fits it is B, according to the homogeneity criterion, while D is the neighbor object that best fits B. If $D = A$ the merge is performed. Otherwise, the loop is repeated assuming B for A and D for B in order to perform the merge in A's neighborhood.

Normally region-growing segmentation approaches starts by randomly setting seeds on the image. Without order concern, these seed's neighboring pixels are evaluated to be merged into the same segment or not. In Baatz and Schäpe (2000) approach, this random seed location and processing order is not utilized to avoid a sub-optimal approach. Instead, the method systematically take points with maximum distance to all other points treated before. In this approach each segment can be treated once per cycle, if the order is defined over segments, or each segment can be treated p times per cycle, where p is the number of pixels in it.

In the *Ecognition*'s implementation, the algorithm uses 4 input parameters: (*i*) *scale*; (*ii*) color; (*iii*) compactness; and (*iv*) spectral bands weight. The *scale* consists in the fusion factor and will limit region fitness and segment size, consequently. The homogeneity criterion (f) used in Baatz and Schäpe (2000) algorithm follows (BAATZ; SCHÄPE, 2000; ESPINDOLA, 2007):

$$f = w_{color} \cdot h_{color} + (1 - w_{color}) \cdot h_{shape}, \tag{2.15}$$

where f is the homogeneity criterion; w_{color} is the color weight; h_{color} is the heterogeneity coefficient for the color attribute, which is complementary to shape; and h_{shape} is the heterogeneity coefficient for the shape attribute.

The color attribute heterogeneity coefficient is a weighted sum of the spectral bands standard-deviation. Described as follow:

$$h_{color} = \sum_{c}^{E} w_c (T_{union} \cdot \sigma_c^{union} - (T_{seg1} \cdot \sigma_c^{seg1} + T_{seg2} \cdot \sigma_c^{seg2})), \tag{2.16}$$

where E is the set of spectral bands, c is a spectral band, $c \in E$, w_c is the weight

for band c, s is a segment, $s \in \{seg1, seg2, union\}$, $seg1$ and $seg2$ are the merging sefments, $union$ is the result segment, T_s is the number of pixels of segment s, σ_c^s is the standard-deviation of segment s. The shape attribute depends on other two parameters: compactness and smoothness, as can be seen:

$$h_{shape} = w_{cp} \cdot h_{cp} + (1 - w_{cp}) \cdot h_{sm}, \qquad (2.17)$$

where h_{shape} is the heterogeneity coefficient for the shape attribute; w_{cp} is the compactness weight; h_{cp} is the heterogeneity coefficient for the compactness attribute and h_{sm} is the heterogeneity coefficient for the smoothness attribute.

Compactness represents the relation between factual edge length and the root of the object size and is given by:

$$cp = \frac{l}{\sqrt{p}}, \qquad (2.18)$$

where cp is the compactness attribute heterogeneity; l is the edge length and n is the number of pixels within the segment.

Smoothness is the deviation from the shortest possible edge length given by the bounding box b of the segment and is given by:

$$sm = \frac{l}{b}, \qquad (2.19)$$

where sm is the smoothness attribute heterogeneity; l is the edge length and b is the bounding box edge length.

Similarly to the color heterogeneity, compactness and smoothness heterogeneity are also calculated for the merging objects. If the calculated f is less than the scale-root-square the objects will be merged (ESPINDOLA, 2007).

2.3.2 Temporal segmentation

Considering that few researches adapted image segmentation techniques to be applied over image time series (THOMPSON; LEES, 2014), Costa et al. (2018) developed a RS image segmentation algorithm, that uses the DTW distance to detect homo-

geneous regions over time. The initial seeds are time series, instead of image pixels that are used in the conventional segmentation. The DTW distance is computed between the time series and their neighbors. If the time series are similar, according to a threshold parameter, their regions are merged, otherwise other neighbors are analyzed. This is repeated until all the neighbors are verified. Next, the growing process is applied to the remaining regions until the whole image has been segmented.

2.4 Multi-source remote sensing

The increasing number of satellite sensors and its data availability, has led to approaches that integrate multiple sensors, the multi-sensor or multi-source (WULDER et al., 2012). Applications with multiple sensors were documented in the past years (PEREIRA, 1988; SHIMABUKURO et al., 1991; POHL; VAN GENDEREN, 1998), though, the recent availability of great amount of orbital data makes this subject of research promising. In the literature, both terms multi-sensor and multi-source have been used as synonymous. Multi-sensor approaches can be employed to integrate different types of sensors, such as passive and active remote sensors (HOLLANDS; DIERKING, 2016; BRAGA et al., 2015). However, in this study, the term multi-source is utilized to nominate data obtained only from optical sources.

Combined data from different sensors can provide a higher spatiotemporal data coverage. In many applications, such as crop monitoring (STEVEN et al., 2003) and change detection (COPPIN et al., 2004), medium, or even high, spatial resolution images are required to provide detailed information of the surface (STEVEN et al., 2003). Though, for these applications, the sensor's revisit rate is long relative to plant active growth period (STEVEN et al., 2003). This strongly supports the combination of multiple observing systems to obtain more frequent measurements (MOUSIVAND et al., 2015). Nevertheless, sensors heterogeneity concerning spectral, directional, radiometric and spatial characteristics must be treated in order to make the data harmonized (SAMAIN et al., 2006; MOUSIVAND et al., 2015; BEHLING et al., 2016).

Samain et al. (2006) organized the multi-source heterogeneous aspects in four categories: spatial, temporal, spectral and directional. The optimum approach to deal with spatial differences between different sensors is to use multi-scale algorithms, which would use each sensor at its native spatial resolution. However, the complexity and processing cost of this approach is high. Resampling data to a common reference is more appropriate, even though this may propagate information loss. When data is resampled to the images with the larger pixels size (obtained by the sensor with least detailed spatial resolution), also called downsampling, information

is lost, whereas resampling to the images with the smaller pixel size (obtained by the sensor with most detailed spatial resolution), also called upscaling, introduces inaccurate measures, since the reconstruction of spectral details is not possible (SAMAIN et al., 2005).

Regarding the temporal aspect, each on-board satellite sensor has its own revisit time. Combining data from different sources and noisy data can make the interval between acquisitions irregular. Similarly to the spatial aspect, the optimum approach is to use each data on its native acquisition date. However, to facilitate image manipulation, several works in the literature suppose that there are few changes between images acquired in close proximity to one another. Based on that, these works adopt a regularly spaced in time dates, as such a bi-monthly data set (BENDINI et al., 2016; VUOLO et al., 2017). In this approach, when there are more images than the adopted, operations are performed, e.g., average or replacing, to maintain the interval.

Variations on Sun-view geometries and imaging angle can affect the reflectance values measured by orbital sensors (JENSEN, 2007). Based on that, when images from multiple sensors are acquired with distinct directional configurations, a treatment must be performed to harmonize the data. Samain et al. (2005), Samain et al. (2006) show that semi-empirical models designed to mimic the Bidirectional Reflectance Distribution Function (BRDF) are an efficient way of exploiting the angular information and harmonizing the observations to pre-defined standard configurations.

Variations in spectral characteristics are harder to deal with than Sun-view geometries (SAMAIN et al., 2006). Different sensors with similar bandwidth may acquire different responses to a same target on Earth's surface (TRISHCHENKO et al., 2002). Based on that, values obtained from different sensors cannot be compared directly. These differences occur even in spectral bands centered on the same wavelength and the same width, e.g CBERS-4/MUX and Landsat-7/ETM+ blue bands ($0.45\mu m - 0.52\mu m$). These differences occur even if sensors have similar spectral bands, because the Specral Response Function (SRF) is specific for each sensor (PINTO et al., 2016). In this context, Trishchenko et al. (2002) studied the effects of SRF on surface reflectance and NDVI measures comparing moderate resolution satellite sensors. The authors concluded that both measures are sensitive to the sensor's SRF and a correction procedure is needed even for similar sensors.

Although the start of the CBERS program history does not coincides with the Landsat program, the program's sensors are very similar. Since Landsat and CBERS sensors spectral bands have few bandwidth differences, similar spatial resolution and

acquisition geometry, with a minimal spectral alignment and spatial resampling, CBERS reflective bands can be seen as an opportunity to build a virtual constellation alongside Landsat data and increase temporal resolution (WULDER et al., 2015).

Consequently, in order to combine signals from different sensors, harmonization is necessary. This is recommended to compare surface reflectance responses from different sensors, especially in the visible bands (HOLDEN; WOODCOCK, 2016). Mainly, there are two approaches to harmonize spectral bands from multiple-sources in the literature: the statistical (SAMAIN et al., 2006; BENDINI et al., 2016; HOLDEN; WOODCOCK, 2016; ROY et al., 2016) and the spectral (HUBBARD; CROWLEY, 2005; GAO et al., 2006; ZURITA-MILLA et al., 2008; AMORÓS-LÓPEZ et al., 2013).

The statistical approach assumes that sensor bands relationship is dependable for any illumination and observation geometry. Based on that, linear regression method can be used as a harmonization method categorized in the statistical approach. The linear regression harmonization uses reflectance reference values to perform a regression analysis with reflectance target values, in the same position in different date, resulting in gain and offset coefficients to each band. In this context, Steven et al. (2003) show that, although spectral bands are not strictly equivalent, surface reflectance can be corrected for spectral band effects. The authors compared the NDVI response from different instruments obtaining a strong linear relation between them. The authors provided an intercalibration table for several sensors: *AVHRR, ATSR2, MSS, TM, ETM+, Spot2, Spot4, IRS, Ikonos, SeaWiFS, MISR, MODIS, POLDER, QuickBird* and *MERIS*.

The spectral approach is based on the restitution of the surface spectral signature. It assumes that the spectral reflectance can be decomposed and related to surface properties (SAMAIN et al., 2006). Efforts using this approach have been made, mainly by combining moderate and medium spatial resolution sensors (GAO et al., 2006; ZURITA-MILLA et al., 2008). Based on that, spectral unmixing method can be used as a harmonization method categorized in the spectral approach. The method based on spectral unmixing (ZURITA-MILLA et al., 2008) can be employed in the spectral approach. In this method, endmembers for predetermined classes, e.g. *vegetation*, *soil* and *water/shadow*, are utilized to transform the spectral image into a combination of class-fraction images through linear equations, defined by (SHIMABUKURO; PONZONI, 2017):

$$\rho_i = a \cdot veg_i + b \cdot soil_i + c \cdot shadow_i + e_i, \tag{2.20}$$

where ρ_i is the pixel reflectance value in band i; a, b, and c are the vegetation, soil and water/shadow proportions, respectively; veg_i, $soil_i$ and $shadow_i$ are the vegetation, soil and water/shadow endmembers and e_i is the error in band i.

Endmembers obtained on a reference image can be applied on fraction images of a target sensor to construct a synthetic image (GEVAERT; GARCÍA-HARO, 2015). The main advantage of this approach is the use of class proportions instead of sensor spectral response on a specific band, however this approach is dependent on the endmember selection (ZURITA-MILLA et al., 2008).

2.4.1 Multi-source applications

Regarding applications, Xaud and Santos (2010) organized the multi-source approach in categories, such as substitution, complementation, calibration and intercalibration. Those approaches have many purposes: substitution of noisy data, add information, calibration, image sharpening and others.

2.4.1.1 Substitution

Substitution is an approach applied when data is unavailable at a determined time and other source data is employed to replace the missing one. An example of this approach can be seen in the Amazon Deforestation Monitoring Project (PRODES), which maps deforestation in the Brazilian Amazon (INSTITUTO NACIONAL DE PESQUISAS ESPACIAIS - INPE, 2002). The project uses selected images with low cloud rates Landsat-5, CBERS-2, CBERS-2B, LISS-3, Resourcesat-1 and UK-DMC2 images to monitor deforestation within Brazil since 1988. When clouds occur, multiple images of close dates are utilized to map an area.

Other example of this approach can be seen in Bendini et al. (2016)'s work, which used the multi-spectral CBERS-4/MUX images to reduce noise on Landsat-8/OLI time series and then improve crop classification. The authors employed vegetation indices (EVI and NDVI) to derive phenological features of crops using filtered image time series and Random Forest algorithm to classify agricultural targets. Landsat time series were classified both with and without replacing original cloudy pixels by CBERS-4 corresponding pixels. In this case, a slight increase in the classification accuracy occurred when the replacement of the noisy pixels was performed.

2.4.1.2 Complementation

Complementation is a multi-source approach that extends a product, for instance with different wavelength bands, to compose it with other characteristics from multiple sensors. In this context, image fusion techniques, like pan sharpening method, can be considered a complementation, since in general, image fusion techniques combine spatial resolution of an image with spectral information of another image to produce a synthetic product (XAUD; SANTOS, 2010; ZHANG, 2010). Collection 6 of MODIS, on board platforms Terra and Aqua, provides multi-source products that uses this approach (UNITED STATES GEOLOGICAL SURVEY - USGS, 2016). Those products include: Leaf Area Index (MYNENI et al., 2015a; MYNENI et al., 2015b) and BRDF and Albedo Model Parameters (SCHAAF, 2015).

2.4.1.3 Calibration and intercalibration

Calibration is a multi-sensor approach that uses a low uncertainty sensor to calibrate other sensors, while Intercalibration is a multi-sensor approach that combines multiple similar sensor observations to minimize uncertainty of a phenomenon. Since Landsat-8/OLI presents low uncertainty data, Pinto et al. (2016) used it as reference to calibrate CBERS-4 MUX and WFI sensors. The authors utilized near simultaneous imaging to compare the sensors responses in a common ground target, and then to obtain the coefficients to calibrate each sensor band. Data from Landsat-7/ETM+ was also employed in the evaluation, obtaining favorable agreement with the reflectance data.

Similarly, Holden and Woodcock (2016) employed near-simultaneous Landsat-8 and Landsat-7 images to analyze consistency of both sensors surface reflection, since some spectral bands of Landsat-8 are narrow. The results showed that is necessary to harmonize their spectral bands, since Landsat-8 visible bands (blue, green and red) are darker and near infrared band in the Landsat-7 satellite is brighter.

Alongside the spectral differences, orbital data is not always "complete". Sometimes due to clouds, or sensor defects, the Earth surface cannot be observed through a specific sensor. In such cases, techniques to recover or estimate the sensor measurements are useful.

2.5 Earth observation data reconstruction and analysis ready data

Ideally, a pixel time series would be completely populated and free of cloud, cloud shadow, or haze, and with no missing data (HERMOSILLA et al., 2015). In reality, a

pixel series may have missing values for particular dates, which results in data gaps. This may affect many existing analysis methods, which generally assume fairly complete data (LOU; OBRADOVIC, 2011). Landsat-7, one of the most utilized satellites, began to present hardware failure on Enhanced Thematic Plus (ETM+) Scan Line Corrector (SLC) in May 2003, resulting in gaps of valid values, or missing data sections on the acquired images. The images collected before such failures are called SLC-on images, and afterwards they are referred as SLC-off. The gaps correspond to a single pixel near the center of a path/row image and can reach 14 pixels in width near image borders (STOREY et al., 2005), as illustrated in Figure 2.8.

Figure 2.8 - Landsat-7/ETM+ SLC-off effect image gaps.
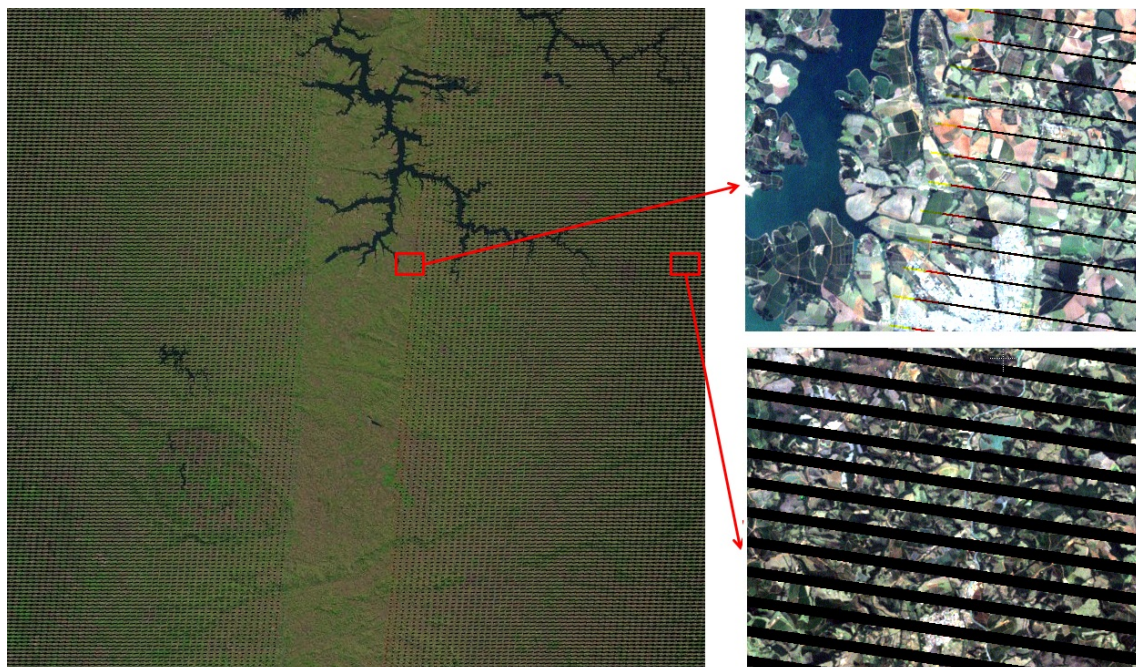
A subset of Landsat-7/ETM+ SLC-off image (path/row 220/75).
Source: Author's production.

Considering Tobler's first law of geography which establishes that near things are more related to each other than distant things (TOBLER, 1970), interpolating Landsat-7 SLC-off missing data would fill the gaps with neighboring pixel values. This procedure is acceptable for small gaps, however it produces less satisfactory results for large gaps. Following that, Maxwell (2004) developed a segmentation approach to fill Landsat-7 SLC-off missing data, pairing it with a reference image that

does not contains gaps, based on three principles:

- Adjacent pixels are more likely to be similar;

- Groups of the same landscape unit are likely to have similar spectral values;

- Most landscapes remain constant for long periods.

This segmentation approach uses a pixel value in its neighboring, delimited by homogeneous regions captured from other close date images (MAXWELL, 2004). As can be seen in Figure 2.9, Maxwell (2004) approach fills a target image containing gaps, a Landsat-7/ETM+ SLC-off image, by segmenting a reference image, such as Landsat-5/TM or Landsat-8/OLI acquired in a close date. The reference image is segmented and these segments are overlayed in the target image. For each segment containing a gap on the target image the mode value is calculated and used to fill the missing data, resulting in a synthetic image.

The gap-filling through segmentation has been improved further by using several segmentation levels. Maxwell et al. (2007) employed three segmentation levels and a nearest neighbor approach in case the third level isn't enough. In this approach, if a segment is fully contained in the missing data, a segmentation level with segments of a larger area is used to fill the gap (MAXWELL et al., 2007). This approach is exemplified in Figure 2.9 and detailed in Algorithm 1. The process is similar to Maxwell (2004), being the difference the number of segmentation levels. This extra segmentations are used in cases which a segment does not contains any valid value, using the other segmentation levels to repeat the process with larger segments.

Figure 2.9 - Multiresolution segmentation approach to fill Landsat-7 SLC-off data.
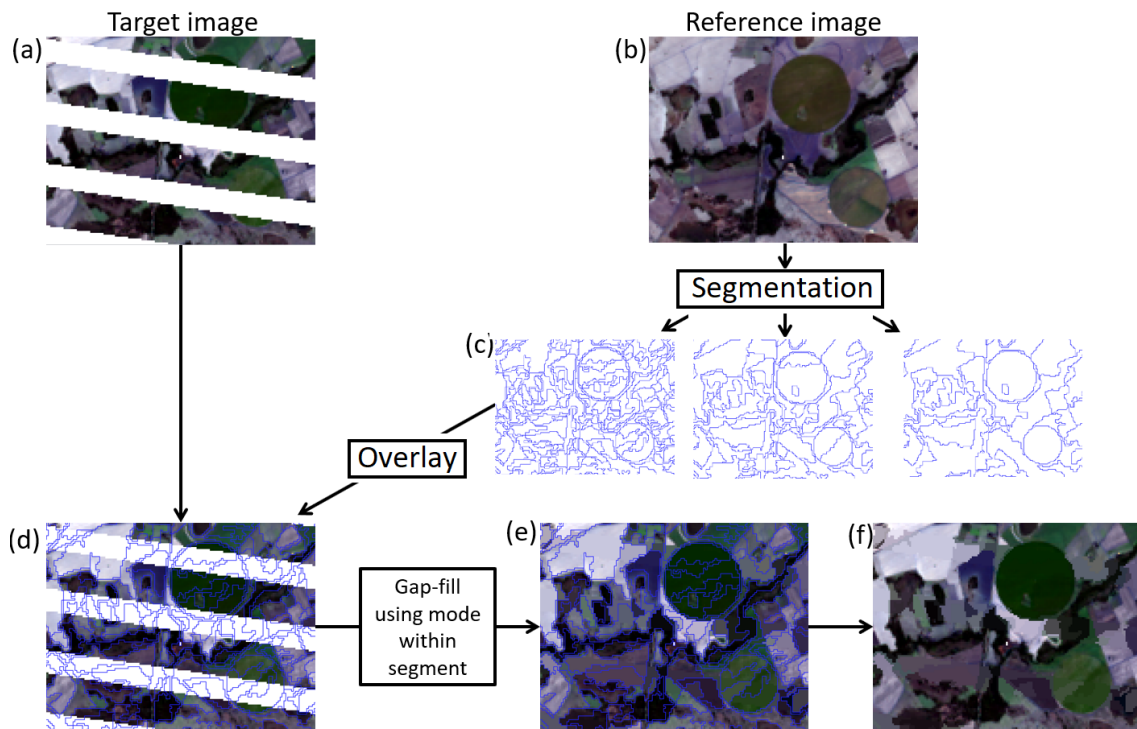
(a) a target image that contains gaps, in this case a Landsat-7/ETM+ SLC-off; (b) a reference image, in this case a Landsat-8/OLI acquired in a close date; (c) the reference image is segmented; (d) the segmentation is overlayed in the target image; (e) the mode value within the segment is calculated and used to fill missing data; (f) resulted synthetic image.

Source: Author's production.

Input: gappedImage, segmentation1, segmentation2, segmentation3
Output: filledImage

1 **foreach** *segment[i] of segmentation1* **do**
2   **if** *there is a NULL value within segment[i]* **then**
3   **if** *segment[i] most frequent value $\neq$ NULL* **then**
4   use segment[i] most frequent value to fill gappedImage NULL values that coincides with segment[i] position
5   **else**
6   **if** *segmentation2 segment on segment[i] position, most frequent value $\neq$ NULL* **then**
7   use segmentation2 segment most frequent value to fill gappedImage NULL values on segment[i] positions
8   **else**
9   **if** *segmentation3 segment that coincides with segment[i] position, most frequent value $\neq$ NULL* **then**
10   use segmentation3 segment most frequent value to fill gappedImage NULL values on segment[i] positions
11   **else**
12   fill gappedImage NULL values with nearest neighbor
13   **end**
14   **end**
15   **end**
16   **end**
17 **end**

Algorithm 1: MULTISCALE GAP-FILLING METHOD (MAXWELL ET AL., 2007) PSEUDO-CODE.

33

In the context of reconstructing Earth's surface observations, Vuolo et al. (2017) developed a methodology to build an equally spaced in time data cube. Data cubes are consistently processed and organized ready data for analysis, which prevent users to perform time-consuming preprocessing corrections as instrument calibration, geolocation and radiometry (AUSTRALIAN GEOSCIENCE, 2015; DWYER; LYMBURNER, 2016; FOGA et al., 2016). The authors employed a set of Landsat-4-5/TM, Landsat-7/ETM+ and Landsat-8/OLI time series to fill clouds and sensor defects. Their approach is based on template matching and smoothing time series.

The first step consists in building a data gap mask. This mask demarcates pixels affected by the SLC-off failure and by clouds. For cloud detection, the authors use the Fmask algorithm (ZHU et al., 2015). The second step consists in equally spacing the time series in a determined rate of 15 days. If there is more than 1 valid pixel on the 15 days interval, an average operation is performed using the values. The third step consists in building a template pool. For that, the authors use a reference land cover map to select appropriate time series with more valid observations for each class. The time series gaps in the templates are then filled using a smoothing algorithm. In the fourth step, the data cube time series that contains gaps is compared to all templates through euclidean distance, ignoring the invalid observations, and filling them using the most similar template. Finally, the smoothing algorithm is applied again independently of each spectral band and each pixel to produce smoothed out and gap-filled images (VUOLO et al., 2017).

Nowadays, due to the big volume of data acquired by sensors, some initiatives are building collaborative platforms to enable scientist to focus on their research instead of preprocessing. The USGS is using Landsat data to develop an Analysis Ready Data (ARD), a consistently data processed to the highest scientific standards and level of processing required for direct use in monitoring and assessing landscape change (UNITED STATES GEOLOGICAL SURVEY - USGS, 2017a). Landsat ARD products are processed to a common tiling scheme containing 5,000 x 5,000 30m pixels.

Another initiative is the Australian Geoscience Data Cube (AGDC), a collaboration between Geoscience Australia, Commonwealth Scientific and Industrial Research Organization (CSIRO), National Computational Infrastructure (NCI), Committee on Earth Observation Satellites (CEOS) and NASA. It uses open source standards and is designed to help both government and private industry to make informed decisions (AUSTRALIAN GEOSCIENCE, 2015). The AGDC provides Surface Reflectance, Landsat Pixel Quality, Landsat Fractional Cover and Landsat NDVI products and

intends to provide a variety of RS data products such as Landsat5/7/8, Sentinel-2A, MODIS, SRTM, and Himawari-8 datasets (CEOS, 2016a; CEOS, 2016b). There is even an effort to develop a merged Landsat and Sentinel-2 (HLS, Harmonized Landsat Sentinel) 5-day product with atmospheric correction (CEOS, 2016b), which emphasizes the importance of developing consistent multi-sensor data.

Despite the trend, methodologies for building data cubes and reconstruct Earth observations are still being developed (AUSTRALIAN GEOSCIENCE, 2015; CEOS, 2016b; WEISS et al., 2014; HERMOSILLA et al., 2015; VUOLO et al., 2017). Besides, scientific and application communities are also interested in the input records, processes, and data origins, the also called data provenance (DI et al., 2013). Based on that, Earth's surface reconstruction and estimation methodologies may also include data provenance in order to achieve interoperability among scientific products. The utility of this information is dependable of the user. Based on that and in the future products that may rise in EO data, in this research we encourage the conception of this kind of metadata.

3 METHODOLOGY

The proposed methodology aims to build a gap-filled optical medium spatial resolution multi-source RS image data cube. The developed methodology is divided in three stages: *(i) Pre-processing*; *(ii) Sensor Harmonization*; and *(iii) Gap-filling*, as illustrated in Figure 3.1.

Figure 3.1 - Methodology diagram.
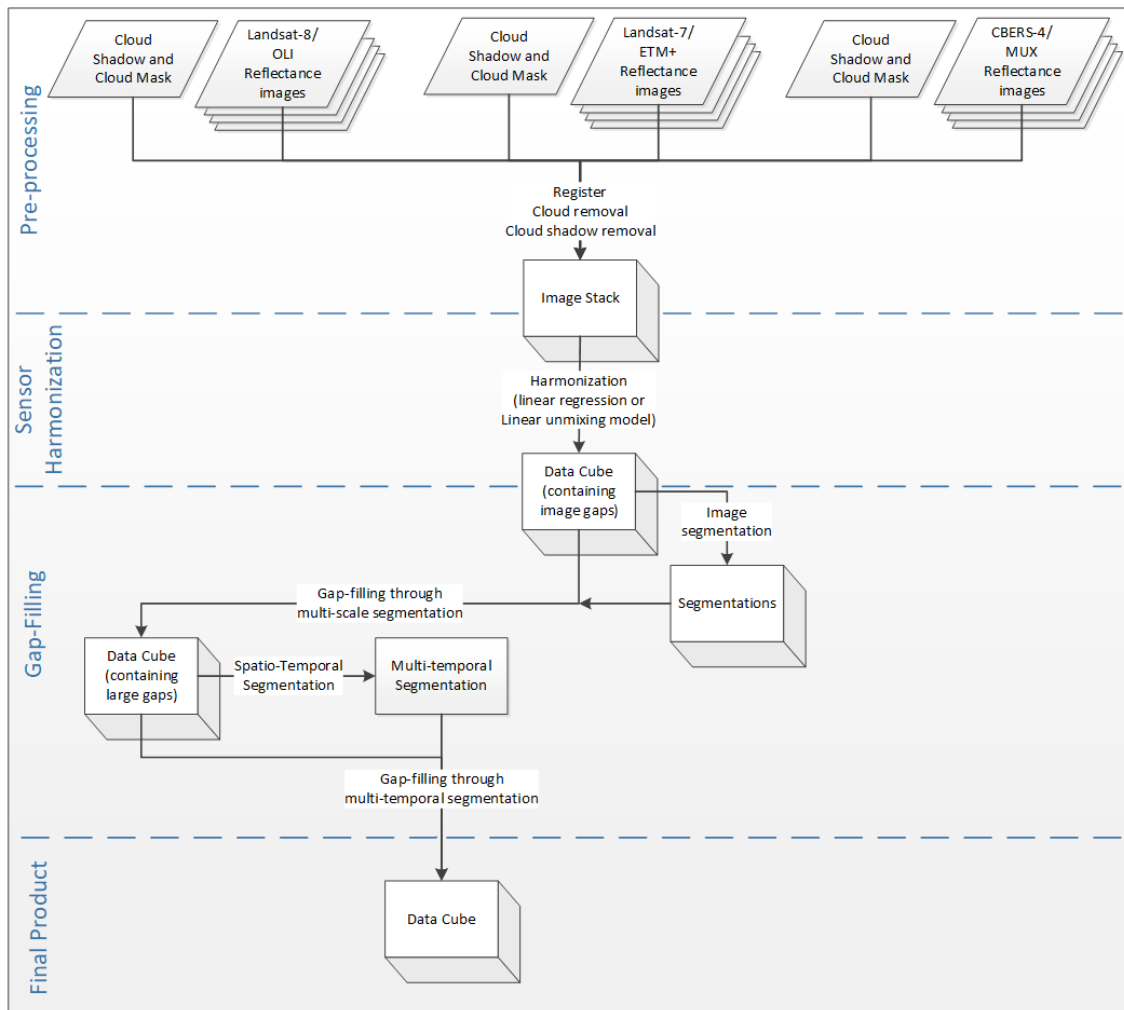
Schematic diagram of the adopted methodology to generate multi-source RS image gap-free data cube.

Source: Author's production.

Since this work uses data from multiple scenes, dates and sensors, some pre-

37

processing and sensor harmonization operations are required to combine the images. The *Pre-processing* stage consists in correcting the sensor/platform specific radiometric, data geometric distortions and providing a mask that infers if an image pixel is a valid surface observation. The *Harmonization* operation, bring these images to a common scale and spectrally harmonizes them. Finally, the *Gap-Filling* procedure aims at filling gaps in the images based on two approaches: filling smaller gaps, e.g. stripes, and small clouds using pixel neighborhood information; and filling larger gaps using time series information.

3.1 Pre-processing

In the *Pre-processing* stage, images from Landsat-8/OLI, Landsat-7/ETM+ and CBERS-4/MUX were acquired and processed to produce the surface reflectance values. A total of 322 images were acquired, respectively 122 Landsat-7/ETM+, 122 Landsat-8/OLI, and 78 CBERS-4/MUX images. Surface reflectance images from Landsat-7/ETM+ and Landsat-8/OLI were obtained through the USGS *EROS Science Processing Architecture* (ESPA) web portal (`https://espa.cr.usgs.gov/`) (UNITED STATES GEOLOGICAL SURVEY - USGS, 2017e). The Landsat-7/ETM+ and Landsat-8/OLI products use the *6S* radiation propagation model through the *Landsat Ecosystem Disturbance Adaptive Processing System* (LEDAPS) (UNITED STATES GEOLOGICAL SURVEY - USGS, 2017c) and *Landsat-8 Surface Reflectance Code* (LaSRC) (UNITED STATES GEOLOGICAL SURVEY - USGS, 2017d) algorithms, respectively (UNITED STATES GEOLOGICAL SURVEY - USGS, 2017e). These images are collection-1 data (UNITED STATES GEOLOGICAL SURVEY - USGS, 2017b) and contain evidences of cloud, cloud shadow, snow, water and clear pixel masks obtained using the *cfmask* algorithm (ZHU; WOODCOCK, 2012; ZHU et al., 2015).

CBERS-4/MUX images can be downloaded in the INPE's image catalog (`http://www.dgi.inpe.br/catalogo/`), which are not available in reflectance values. However, we got CBERS-4 reflectance images that were produced by INPE's researchers based on a method developed by Martins et al. (2018). The cloud mask for CBERS-4/MUX was also provided by INPE's researchers and it is adaptation of the *cfmask* algorithm (ZHU; WOODCOCK, 2012; ZHU et al., 2015) for sensor that doesn't have the thermal bands. It thresholds spectral indices (NDVI, WI, M, HOT), spectral bands (Blue, Green, Red and NIR) and their standard deviations to delimit clouds and cloud shadow (SILVA; LIPORACE, 2016; MARUJO et al., 2017c), as demonstrated in Chapter 2.1.2.

All acquired images from ETM+ and OLI, were already registered with an accuracy

less than or equal to 12m Radial Root Mean Square Error (RMSE) to the Global Land Survey (GLS) reference database, as all Collection-1 data (UNITED STATES GEOLOGICAL SURVEY - USGS, 2017b). In order to ensure spatial comparison, the CBERS-4/MUX images were resampled to 30m, taken OLI images as reference, through a bilinear function. This approach was adopted to avoid nearest neighbor information loss, however a cubic convolution would also be a considerable approach. Next, a manual registration was employed to register the images. First, MUX images were registered between themselves and, posteriorly, they were registered adopting OLI as reference. After ensuring the registration, all images were cropped into a square grid of 100 km x 100 km using the Military Grid Reference System (MGRS).

3.2 Sensor Harmonization

To ensure spectral harmonization between images, we assumed that OLI, ETM+ and MUX inclination can be ignored (difference of 0.3 degrees). Two harmonization approaches were conducted: *(i)* the spectral unmixing harmonization; *(ii)* the linear regression harmonization. To verify which approach would be used on the entire cube, initially two cloud-free images for each sensor were used tested to test both harmonization approaches. Considering also that ETM+ and OLI sensors acquire images with a time difference of nearly 8 days, to ensure acquisition on most coincidental date, the study area was chosen as the intersection between Landsat Path/Row 219/075 and 220/075 (WRS 2 – Worldwide Reference System 2) areas that provide images with one day of difference. This area overlaps with CBERS-4/MUX images acquired in the Path/Row 155/124 (CBERS WRS Path Row). Table 3.1 presents image acquisition dates used in the tests.

Table 3.1 - Acquisition dates for ETM+, OLI and MUX images.

	Landsat-8/OLI	Landsat-7/ETM+	CBERS-4/MUX
Date 1	06 Aug 2015 (219/075)	05 Aug 2015 (220/075)	04 Aug 2015 (115/124)
Date 2	29 Aug 2015 (220/075)	30 Aug 2015 (219/075)	30 Aug 2015 (115/124)

Considering OLI images as reference to harmonize images from target sensors (ETM+ and MUX), to perform the spectral unmixing harmonization, endmembers were manually collected, on reference sensor images in a given date (here called Date 1). The same endmembers locations were used in the target sensor images to obtain endmembers from the target sensor images, obtained in a given date (here

called Date 2). The endmembers were collected for classes of *vegetation*, *soil* and *water/shadow*, using the blue, green, red and NIR bands. During the endmember sampling of the aforementioned classes, the selected areas were ensured to remain unchanged on all images and that these points were not in border regions. Each target image was converted into fraction images using the endmembers through the spectral linear unmixing model. Then, using reference endmembers and the fraction images from the target sensors, the reverse process of unmixing transformation was employed in order to generate a synthetic reference sensor image on Date 2. To do that, each reference endmember of each class were multiplied by the target class fraction image and added by its error. As a result of this process, synthetic OLI images were generated. This process is shown in Figure 3.2.

Figure 3.2 - Spectral unmixing harmonization diagram.
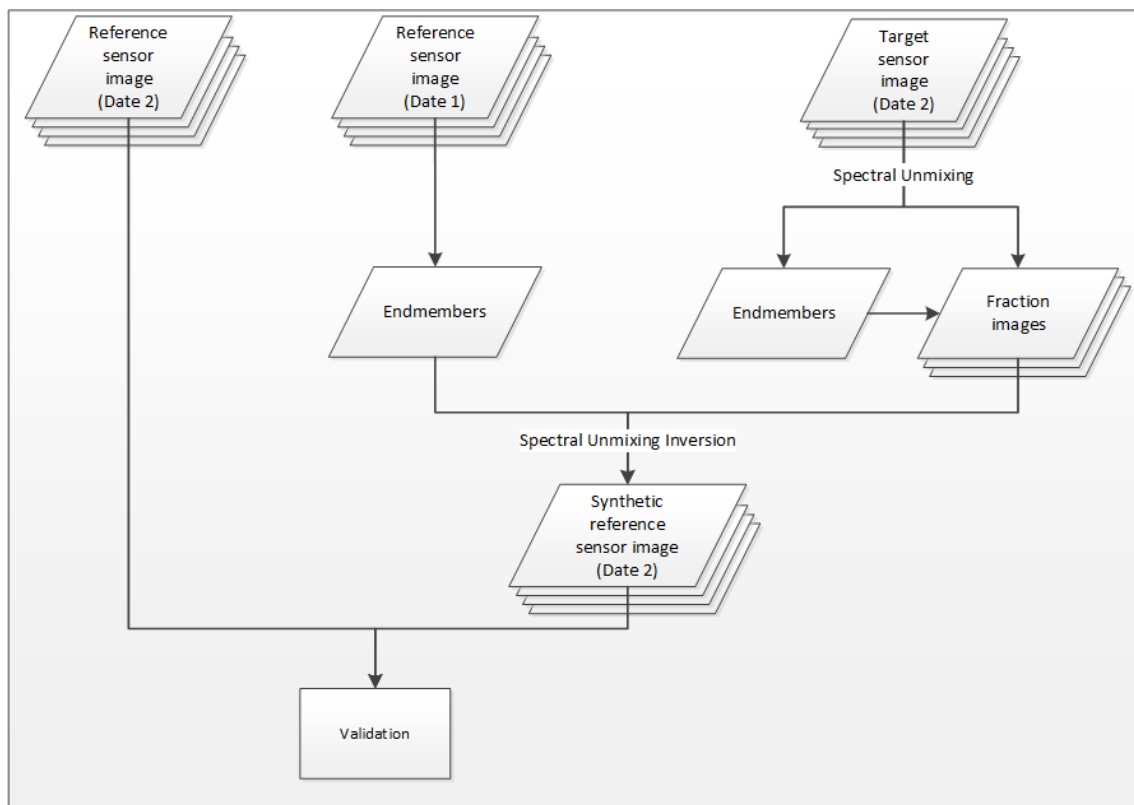
Schematic diagram of the spectral unmixing harmonization methodology generating a synthetic image and validating it with an image from close date.

Source: Author's production.

We utilized the Monte Carlo approach to perform the linear regression harmonization. This approach was used, instead of using the entire image to perform the regression, in order to avoid assuming a statistical distribution of the image and for the methodology to be scene independent. For each pair of target and reference image bands, a linear regression was performed, with $10,000$ random samples (pixels), which was repeated $1,000$ times. This samples were used on images from each pair on a given date (here called Date 1) in order to perform the regression (Table 3.1). After each regression a gain and offset coefficients were obtained. Using the average gain and offset coefficients obtained from all regressions during the Monte Carlo, this coefficients were multiplied by images from a second date (here called Date 2) target images to generate synthetic images, as illustrated in Figure 3.3.

Figure 3.3 - Linear regression spectral harmonization diagram.
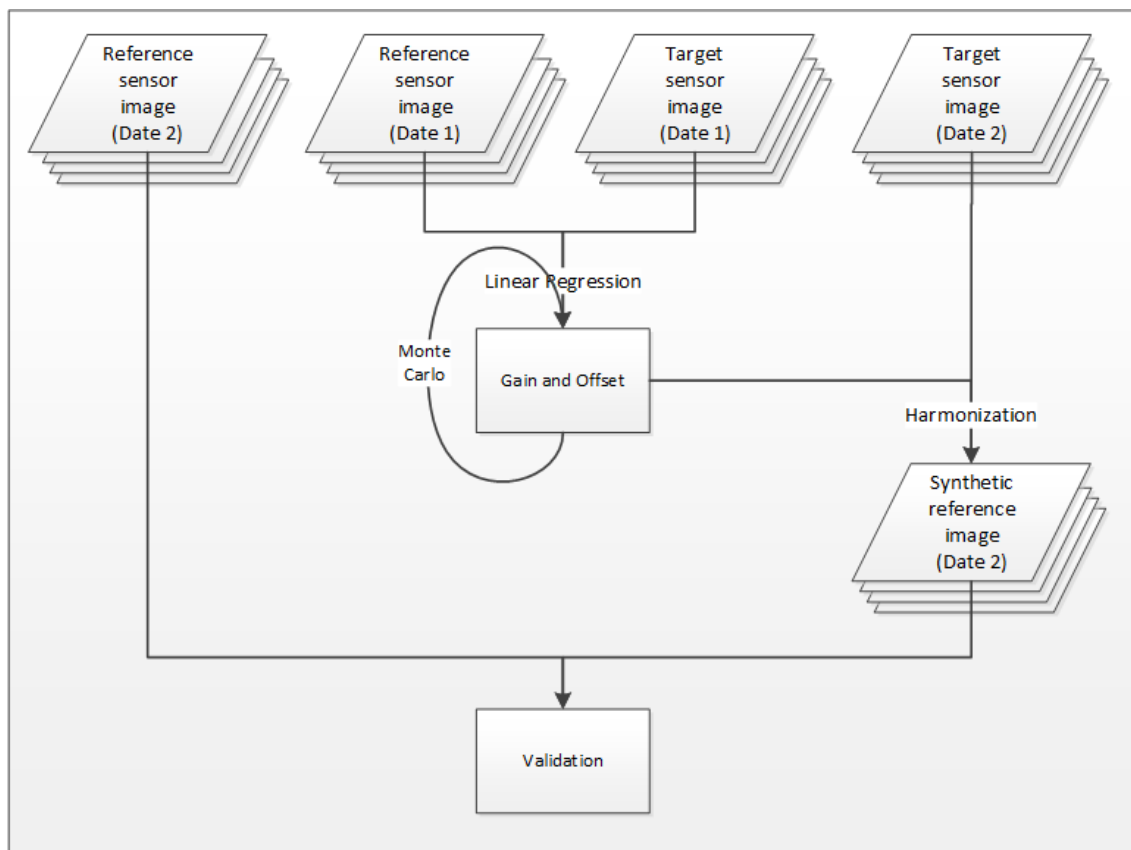
Schematic diagram of the harmonization methodology based on linear regression and validation using an image from close date.

Source: Author's production.

Both spectral harmonization methods were validated by comparing pairs of resulted synthetic images and Landsat-8/OLI reference images. Each image pixel was used to compare the images and calculate the Pearson's correlation coefficients.

3.3 Gap-filling

Even though all images are harmonized and can be used, gaps are still present. Gaps are detected as missing information, e.g. areas were there was cloud or cloud shadow and partial images, tagged as NULL values on images. Here these gaps are filled using the segmentation and time series matching approaches. The proposed gap-filling approach is inspired in Vuolo et al. (2017) which propose to fill multi-spectral time series. However we modified the method in four main points: *(i)* we use time series without smoothing algorithms because time series smoothing can remove important information (HIRD; MCDERMID, 2009; ADAMI et al., 2018); *(ii)* the resulting data cube dates are based on real image acquisition dates and not in a forced equidistant interval; *(iii)* two sequential approaches are employed to fill the gaps: the first one is an adaptation of Maxwell et al. (2007) method, which uses spatial context and segmentation to fill small gaps; and the second one uses time series matching based on a multi-temporal segmentation (COSTA et al., 2018) to fill large gaps and partial images; and *(iv)* our method relies on a multi-temporal segmentation that automatically merges homogeneous regions over the time, which makes it independent of reference data employed to extract time series templates.

3.3.1 Gap-filling through pixel weighting based on multiscale segmentation

In order to calculate the pixel weighting, the proposed method uses the mean value of the segment instead of the most frequently value (mode) suggested in Maxwell et al. (2007), but also maintaining the use of 3 fixed segmentations. In this case, two images are required in the processing: a target image that's the image with missing observations (gaps) and a reference image acquired in a date close to the target image one. We defined that the acquisition time interval between these images must be less than 9 days, otherwise this gap-filling process is not performed, since the remaining gaps will be filled by the second approach. The Baatz and Schäpe (2000) algorithm was adopted to generate 3 levels of segmentation, as in Maxwell et al. (2007). Each segmentation level contains segments of different sizes. Levels 1, 2 and 3 contain small, medium and large segments, respectively.

The Gap-filling procedure is illustrated in Figure 3.4, in which the gap-filling process

is performed using pairs of images, a reference and a target, notwithstanding it is applied to an image data cube. First, reference image is segmented. The segmentation produced in the level 1 is superimposed on both target and reference images. For each segment in the target image that contains gaps the mean value of this segment for both images are calculated. In the reference image, each pixel within the segment is divided by its mean, here called pixel weighting. The pixel weighting means how much this pixel is similar to its segment. Back to the target image, the gaps are filled with target image segment mean weighted by pixel weighting. In a case where all pixel values within a segment are null, the filling process is repeated using the next segmentation level, similarly to Maxwell et al. (2007).

The main difference between Maxwell et al. (2007) and the proposed approach is that instead of using the mode directly to fill the segment, in the proposed approach the reference image is also used to obtain the weighting distribution within the segment and that information is used in the filling process instead of using a single value. The main differences and similarities can be seen in Table 3.2, while the processing is detailed in Algorithm 2.

Table 3.2 - Differences between gap-filling through segmentation, multiscale segmentation and our proposed method which uses multiscale segmentation pixel weighting.

	Algorithm		
	Maxwell (2004)	Maxwell (2007)	Marujo (2019)
Fill gaps using segmentation	✓	✓	✓
Uses multiple levels of segmentation	x	✓	✓
Metric used to estimate missing values	mode	mode	pixel weighted mean
Realistic texture on gap-filled areas	x	x	✓

Figure 3.4 - Segmentation approach to fill Landsat-7 SLC-off data.
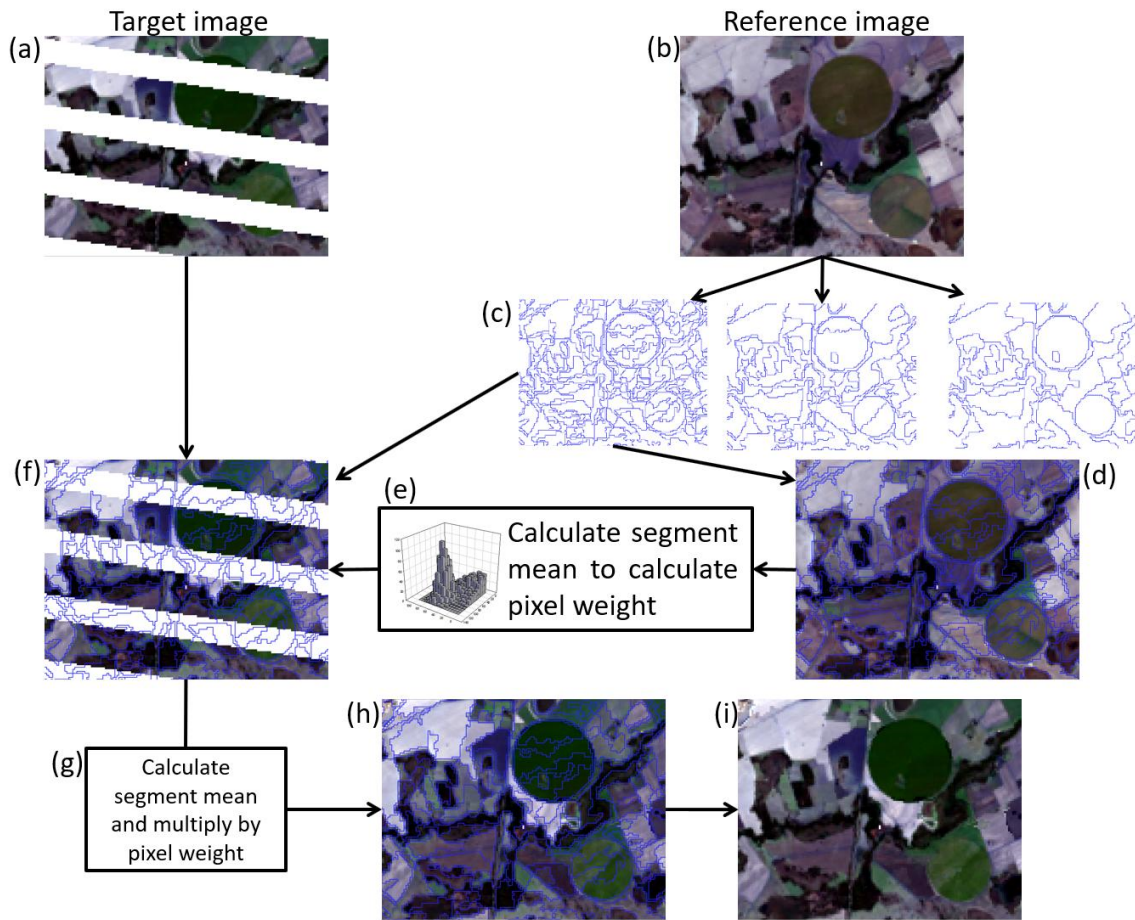
Segmentation approach fills Landsat-7 SLC-off gap images: (a) a target image contains gaps, in this case a Landsat-7 SLC-off; (b) a reference image is used, such as Landsat-5 or Landsat-8 acquired in a close date; (c) the reference image is segmented; (d) these segments are applied in the reference image; (e) the segment mean value is calculated and used to calculate pixel weights; (f) the segmentation is overlayed in the target image and the mean value within the segment is calculated; (g) for each pixel within the segment, its weight is multiplyed by the segment mean; (h) the gaps are filled with this result; (i) a synthetic image is obtained.

Source: Author's production.

In order to validate the method a study case was performed using Landsat-8/OLI images. The study area is the intersection between Landsat Path/Row 223/072 and 222/072 (WRS 2) areas, which can provide images with acquisition time difference of $7 - 9$ days. Based on that, 3 pairs of images were employed in the study, as can be seen in Table 3.3. The SLC-off effect was simulated using a Landsat-7/ETM+ image, while other image was adopted as reference to perform segmentation. The

44

Input: gapImage, refImage, seg1, seg2, seg3
Output: filledImage

1 **foreach** *segment[i] of seg1* **do**
2   **if** *there is a NULL value within segment[i]* **then**
3   **if** *gapImage mean value in segment[i] pixels $\neq$ NULL* **then**
4   meanTarg = gapImage mean in segment[i] pixels
5   meanRef = refImage mean in segment[i] pixels
6   pixelWeight = vector()
7   pixelWeight = (refImage values in segment[i] pixels)/meanRef
8   gapImage NULL values in segment[i] = meanTarg * pixelWeight
9   **else**
10   segment[i] = seg2 segment on segment[i] position
11   **if** *there is a NULL value within segment[i]* **then**
12   **if** *gapImage mean value in segment[i] pixels $\neq$ NULL* **then**
13   meanTarg = gapImage mean in segment[i] pixels
14   meanRef = refImage mean in segment[i] pixels
15   pixelWeight = vector()
16   pixelPro = (refImage values in segment[i] pixels)/meanRef
17   gapImage NULL values in segment[i] = meanTarg * pixelWeight
18   **else**
19   segment[i] = seg3 segment on segment[i] position
20   **if** *there is a NULL value within segment[i]* **then**
21   **if** *gapImage mean value in segment[i] pixels $\neq$ NULL* **then**
22   meanTarg = gapImage mean in segment[i] pixels
23   meanRef = refImage mean in segment[i] pixels
24   pixelWeight = vector()
25   pixelWeight = (refImage values in segment[i] pixels)/meanRef
26   gapImage NULL values in segment[i] = meanTarg * pixelWeight
27   **else**
                             /* Values are not filled   */
28   **end**
29   **end**
30   **end**
31   **end**
32   **end**
33   **end**
34 **end**

Algorithm 2: MULTISCALE GAP-FILLING METHOD PSEUDO-CODE.

gap filled image obtained by applying the proposed method was validated using the original images (from before simulating the SLC-off effect).

Table 3.3 - Acquisition dates for OLI images on Path/Row 223/072 and 222/072 to test the proposed gap-filling approach and Maxwell et al. (2007) method.

	Date 1	Date 2
Pair 1	02 Aug 2015 (219/075)	11 Aug 2015 (220/075)
Pair 2	28 Jul 2016 (219/075)	04 Aug 2016 (220/075)
Pair 3	31 Jul 2017 (219/075)	07 Aug 2017 (220/075)

3.3.2 Algorithm code and data provenance

A functional R script of the method can be found in Appendix A and is also distributed in `https://github.com/MarujoRe/EO_filling` as *marujo_multiscale.R*. The code is open source, free and is published so it can be used or adapted. The code uses 3 existent packages. *foreach* and *doParallel* are two packages used to parallelize the processing, distributing one segment to each processor on the filling stage. The third dependency package is the *raster* package, which is used to work with raster structures.

Regarding data provenance, for this study, an extra band was saved alongside the images, containing which pixel was filled in the process and by which image and segmentation level. An example of this band information can be seen in Figure 3.5. This band includes information about which segmentation level and date was employed to gap-filling.

Figure 3.5 - Partial data provenance band.

0	0	0	0	0	0	0	0
0	0	0	0	0	0	0	0
0	0	0	0	0	0	0	0
0	0	0	0	0	0	0	0
0	0	0	0	0	0	0	0
0	0	0	0	0	0	0	0
seg1_20150802	seg1_20150802	seg1_20150802	seg1_20150802	seg1_20150802	0	0	0
seg1_20150802	seg1_20150802	seg1_20150802	seg1_20150802	seg1_20150802	seg1_20150802	seg1_20150802	seg1_20150802
seg1_20150802	seg1_20150802	seg1_20150802	seg1_20150802	seg1_20150802	seg1_20150802	seg1_20150802	seg1_20150802
seg1_20150802	seg1_20150802	seg1_20150802	seg1_20150802	seg1_20150802	seg1_20150802	seg1_20150802	seg1_20150802
0	0	seg1_20150802	seg1_20150802	seg1_20150802	seg1_20150802	seg1_20150802	seg1_20150802
0	0	0	0	0	0	0	0
0	0	0	0	0	0	0	0
0	0	0	0	0	0	0	0
0	0	0	0	0	0	0	0
0	0	0	0	0	0	0	0

Partial data provenance band of Landsat-7/ETM+ from 08/10/2015, containing gap-filled history. "0" means that the pixel value was not changed. "seg" means that a segmentation was employed to fill the gapped location, followed by the segmentation level, which varies from 1 to 3. The following number sequence regards the date used to fill that location, in the format year/month/date.

Source: Author's production.

3.3.3 Gap-filling through multi-temporal segmentation time series matching

At this stage, the image data cube null values are due to clouds or partial images, regions that were not treated by the first gap-filling approach due to their size or lack of spatial information. Therefore, the methodology aims at filling those gaps values using temporal information through time series. The first step consists in segmenting the image data cube through multi-temporal segmentation to obtain homogeneous regions along the time (COSTA et al., 2018).

The gap-filling procedure based on time series matching is registered in Algorithm 3. First, the average time series is calculated for each segment, to serve as a segment reference time series. The null values within the segment are filled using this reference, since the segmentation guarantees that the segments are homogeneous along time. For a given date, if none valid observation is found within the segment, the reference time series do not have information for this date. For these cases, the missing values are estimated by a cubic polynomial interpolation of the time series. This approach was used considering that a time period of two years was used. Based on that, the series behavior is better described by this function rather than a simple nearest neighbor or linear interpolation.

Input: `gappedDataCube, segmentation`
Output: `filledDataCube`
```
1 foreach segment[i] of segmentation do
2     meanTS = vector()
3     meanTS = segment[i] time series mean
4     foreach timeSeries[j] within segment[i] do
5         if there is a NULL value within timeSeries[j] then
6             timeSeries[j] NULL values = meanTS values from the same
               position
7         end
8     end
9 end
```
Algorithm 3: TIME SERIES MATCHING GAP-FILLING METHOD PSEUDO-CODE.

As mentioned, the proposed gap-filling process is inspired in Vuolo et al. (2017). Based on that, Table 3.4 present the main differences and similarities between both methods. The main differences consists in (*i*) our method not requiring a previous reference of the area, since the multi-temporal segmentation groups similar regions; (*ii*) our method fills all missing values within a segment using a single time series extracted from the segment in analysis.

Table 3.4 - Differences between gap-filling through template matching and multi-temporal segmentation.

	Algorithm	
	Vuolo (2017)	Marujo (2019)
Uses time series information	✓	✓
Smoothed results	✓	x
Realistic texture on gap-filled areas	✓	x
Uses spatial information	x	✓
Does not require previous classification of the area (templates)	x	✓

3.3.4 Algorithm code and data provenance

A functional R script of the method can be found in Appendix B and is also distributed in https://github.com/MarujoRe/EO_filling as *marujo_ts_filling.R*. The code is open source, free and is published so it can be used or adapted. The code uses 4 existent packages: *foreach* and *doParallel* are used to parallelize the processing, *raster* package is used to work with raster structures and the *zoo* package is used to interpolate NA (not available) values in time series.

Regarding data provenance, for this study, an extra band was saved alongside the images, containing the information of which pixel was filled in the process using time series. An example of this band information can be seen in Figure 3.6. This band was an enhancement of the provenance band from the previous gap-filling step, now including the string "TemporalFill" to indicate pixels filled using the multi-temporal segmentation template matching.

Figure 3.6 - Partial data provenance band.

(a) (before temporal fill)

0	0	0	0	0
0	0	0	0	0
0	0	0	0	0
0	0	0	0	0
0	0	0	0	0
0	0	0	0	0
0	0	0	0	0
0	0	0	0	0
0	0	0	0	0
0	0	0	0	0
0	0	0	0	0
0	0	0	0	0
0	0	0	0	0
0	0	0	0	0
0	0	0	0	0
0	0	0	0	0
0	0	0	0	0

(a) (after temporal fill)

TemporalFill	TemporalFill	TemporalFill	TemporalFill	TemporalFill
TemporalFill	TemporalFill	TemporalFill	TemporalFill	TemporalFill
TemporalFill	TemporalFill	TemporalFill	TemporalFill	TemporalFill
TemporalFill	TemporalFill	TemporalFill	TemporalFill	TemporalFill
TemporalFill	TemporalFill	TemporalFill	TemporalFill	TemporalFill
TemporalFill	TemporalFill	TemporalFill	TemporalFill	TemporalFill
TemporalFill	TemporalFill	TemporalFill	TemporalFill	TemporalFill
TemporalFill	TemporalFill	TemporalFill	TemporalFill	TemporalFill
TemporalFill	TemporalFill	TemporalFill	TemporalFill	TemporalFill
TemporalFill	TemporalFill	TemporalFill	TemporalFill	TemporalFill
TemporalFill	TemporalFill	TemporalFill	TemporalFill	TemporalFill
TemporalFill	TemporalFill	TemporalFill	TemporalFill	TemporalFill
TemporalFill	TemporalFill	TemporalFill	TemporalFill	TemporalFill
TemporalFill	TemporalFill	TemporalFill	TemporalFill	TemporalFill
TemporalFill	TemporalFill	TemporalFill	TemporalFill	TemporalFill
TemporalFill	TemporalFill	TemporalFill	TemporalFill	TemporalFill
TemporalFill	TemporalFill	TemporalFill	TemporalFill	TemporalFill

(b) (before temporal fill)

0	0	0	0	0
0	0	0	0	0
0	0	0	0	0
0	0	0	0	0
0	0	0	0	0
0	0	0	0	0
0	0	0	0	0
0	0	0	0	0
seg1_20150811	seg1_20150811	seg1_20150811	seg1_20150811	0
seg1_20150811	seg1_20150811	seg1_20150811	seg1_20150811	seg1_20150811
seg1_20150811	seg1_20150811	seg1_20150811	seg1_20150811	seg1_20150811
seg1_20150811	seg1_20150811	seg1_20150811	seg1_20150811	seg1_20150811
seg1_20150811	seg1_20150811	seg1_20150811	seg1_20150811	seg1_20150811
seg1_20150811	seg1_20150811	seg1_20150811	seg1_20150811	seg1_20150811
0	0	0	0	0
0	0	0	0	0
0	0	0	0	0

(b) (after temporal fill)

TemporalFill	TemporalFill	TemporalFill	0	0
TemporalFill	TemporalFill	TemporalFill	TemporalFill	0
TemporalFill	TemporalFill	TemporalFill	TemporalFill	0
TemporalFill	TemporalFill	TemporalFill	TemporalFill	TemporalFill
TemporalFill	TemporalFill	TemporalFill	TemporalFill	TemporalFill
0	TemporalFill	TemporalFill	TemporalFill	TemporalFill
0	0	TemporalFill	TemporalFill	TemporalFill
0	0	0	TemporalFill	TemporalFill
seg1_20150811	seg1_20150811	seg1_20150811	seg1_20150811	TemporalFill
seg1_20150811	seg1_20150811	seg1_20150811	seg1_20150811	seg1_20150811
seg1_20150811	seg1_20150811	seg1_20150811	seg1_20150811	seg1_20150811
seg1_20150811	seg1_20150811	seg1_20150811	seg1_20150811	seg1_20150811
seg1_20150811	seg1_20150811	seg1_20150811	seg1_20150811	seg1_20150811
seg1_20150811	seg1_20150811	seg1_20150811	seg1_20150811	seg1_20150811
0	0	0	0	0
0	0	0	0	0
0	0	0	0	0

Partial data provenance band of Landsat-7/ETM+ image from 19 Aug 2015, containing gap-filled history. "0" means that the pixel value was not changed. "seg" means that a segmentation was employed to fill the gapped location, followed by the segmentation level, which varies from 1 to 3. The following number sequence regards the date used to fill that location, in the format year/month/date. "TemporalFill" means that the pixel value was filled through segmentation time series matching.

Source: Author's production.

3.4 Case studies

After testing each method individually, in order to test the the entire procedure of harmonization and gap-filling of Earth's surface data on an entire image data cube, two study areas were carried out using Landsat-7/ETM+, Landsat-8/OLI and CBERS-4/MUX images. The study areas are located in Goiás state (center-west of Brazil), as shown in Figure 3.7. The study areas are two Military Grid Reference System (MGRS) tiles, $22KDF$ and $22KEF$, that intersects with 3 Landsat scenes, Path/Rows 223/072, 222/072 and 222/073 (WRS 2) and 6 CBERS-4/MUX scenes, Path/Rows: 162/119, 162/120, 161/119, 161/120, 160/119 and 160/120 (CBERS WRS Path Row). In Figure 3.7 the Landsat and CBERS path/rows are shown in green and red squires, respectivelly. The study was performed using images from August 2015 to October 2017. This time period was chosen because CBERS-4 was operational and also due to, in Brazil, summer crops are normally planted during September/October. Besides, we got images less than 50% of cloud cover. Considering study area $22KDF$, 44 Landsat-7/ETM+ images, 41 Landsat-8/OLI, and 41 CBERS-4/MUX were used, while study area $22KEF$ used 78 Landsat-7/ETM+, 81 Landsat-8/OLI and 37 CBERS-4/MUX.

Figure 3.7 - Study areas and sensors path/rows.
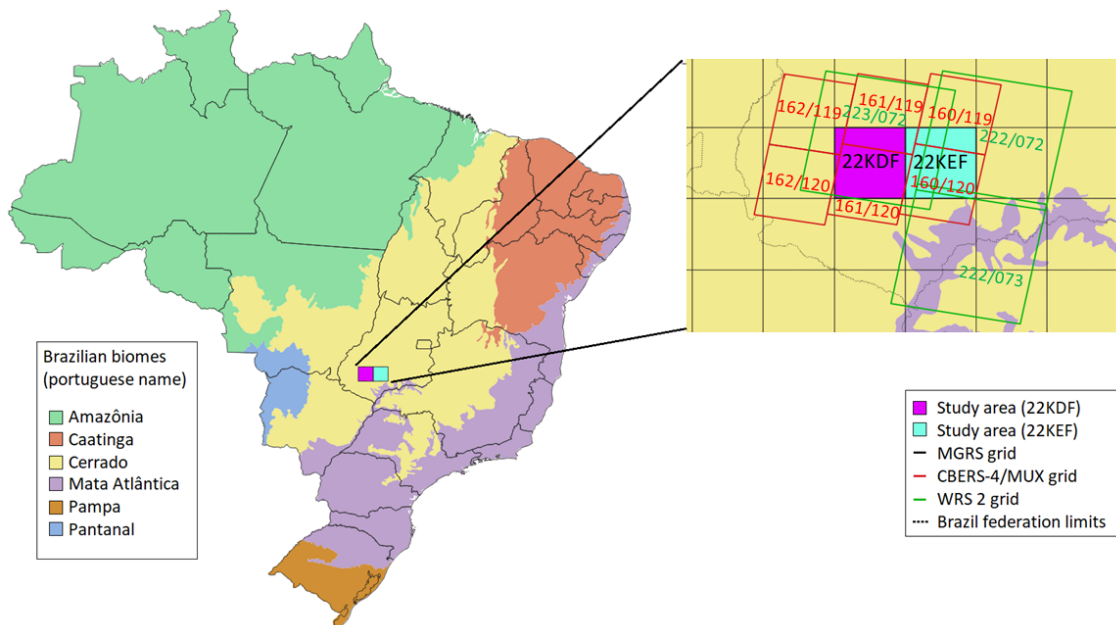
Study areas in Goiás state, Brazil, showing the Landsat and CBERS-4 path/rows.
Source: Author's production.

51

These two study areas, 22KDF and 22KEF, were defined to show how the methodology behave in different situations. In the first case, the tile is fully contained in the satellite scene. In the second case, the tile is located in the bordering path/row regions, resulting in partial images.

Pixels affected by clouds or cloud shadows were removed using quality masks. All images were acquired in reflectance values. They were resampled to 30m, registered and spectrally harmonized using linear regression, since in the results this approach showed better results than the spectral unmixing approach on the previous tests. To perform the linear regression harmonization on an image data cube, a 9 days difference was adopted as the maximum day interval, otherwise, the regression was performed using the mean gain and offset obtained from all other cases. This workflow produced a gapped image data cube. For validation purpose, we replicated the approach used by Vuolo et al. (2017), by randomly removing samples from valid areas, but increasing the number of 10x10 pixel boxes to three, since our area was larger. The artificial data gaps creation is illustrated in Figure 3.8. After the data cube was totally filled, the reference data was compared with the gap-filled data through Pearson Correlation Coefficient, Mean Absolute Error (MAE) and Visual Information Fidelity (VIF) (SHEIKH; BOVIK, 2006).

Figure 3.8 - Artificial data gaps.
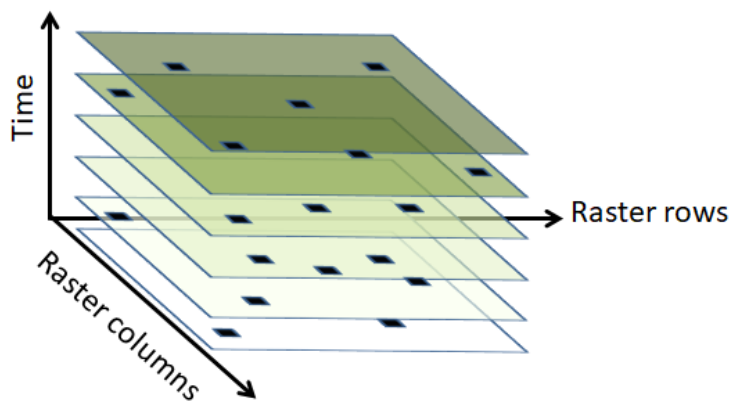
Generating validation samples. The black polygons indicate the position of the $10x10$ pixels sized boxes, which are removed from the time series.

Source: Author's production.

This gapped image data cube was filled using our proposed methodology. During the process, an extra band was created to store the processed pixel history, in order to provide possible users with information regarding the processes performed on the images. During the first gap filling process for instance, each filled pixel in this band contains information about which image and segmentation level was employed in the process. In the time series matching step, this band shows which pixels of the time series were filled by this second process.

Similarly in the *Harmonization* step, in the gap-filling step for the first gap filling method, a 9 days interval was defined. During this 9 day window, if there was a target and a reference images, the gap-filling process were performed, otherwise, in cases which there were no images available in this interval, the first gap-filling process wasn't applied. After that, the second gap-filling procedure, multi-temporal segmentation template matching, was applied. To validate the processing, previous validation areas were utilized to compare the filled values and the original values through R^2, MAE, Universal Quality Image Index (UIQI) (WANG; BOVIK, 2002) and VIF (SHEIKH; BOVIK, 2006). Afterwards, an optical multi-source RS images data cube is obtained so that it can be used in numerous RS applications.

4 RESULTS

The first results, presented in Section 4.1, refer to the spectral harmonization between Landsat-7/ETM+ and Landsat-8/OLI (L7·L8) and also between CBERS-4/MUX and Landsat-8/OLI (L8·C4) that already was published in Marujo et al. (2017a). The second results, presented in Section 4.2, refer to our proposed adaptation of Maxwell et al. (2007) method to fill gaps using multiscale segmentation. The third results, presented in Section 4.3, refer to the gap-filling process through multi-temporal segmentation time series matching.

4.1 Spectral Harmonization

Table 4.1 shows gain and offset coefficient values for each image band employed to spectrally harmonize the sensors through linear regression. These coefficients were utilized to transform Landsat-7/ETM+ and CBERS-4/MUX images into synthetic Landsat-8/OLI images. The gain coefficients values indicate that Landsat-7/ETM+ was more consistent with Landsat-8/OLI than CBERS-4/MUX.

Table 4.1 - Linear regression coefficients (gain and offset) for Landsat-8/OLI (L8) with CBERS-4/MUX (C4) and Landsat-8/OLI with Landsat-7/ETM+ (L7) in the blue, green, red and near infrared bands.

	Blue band		Green band		Red band		NIR band	
	Offset	Gain	Offset	Gain	Offset	Gain	Offset	Gain
L8 C4	184.78	0.69	106.13	0.89	28.04	1.02	209.25	1.28
L8 L7	-51.61	1.03	-24.89	1.05	-38.27	1.07	8.20	1.07

After applying the coefficients to generate the synthetic images, the resulted images were compared with the original images using the Pearson correlation coefficients, which can be seen in Table 4.2. The comparison was made using the obtained images harmonized through linear spectral unmixing and through linear regression (from tests using images in Table 3.3). The results indicate that shorter wavelength bands, mainly the blue band, are less intercorrelated than longer ones, such as red and near infrared. This is probably due to atmosphere interference in lower wavelength bands that was not completely suppressed by the atmosphere correction method (JENSEN, 2007). These results corroborates with Holden and Woodcock (2016) which also obtained better results for the longer wavelength bands.

The results in Table 4.2 indicate that Pearson correlation values obtained by linear

Table 4.2 - Pearson correlation coefficients obtained by harmonizing, through linear spectral unmixing (each date separately) and linear regression (both dates) for Landsat-8/OLI (L8), Landsat-7/ETM+ (L7) and CBERS-4/MUX (C4) imagery from 04/07/2015 and 08/29/2015.

	Blue band	Green Band	Red Band	NIR Band
Unmixing L8 C4 (date 1)	0.78	0.82	0.85	0.89
Unmixing L8 C4 (date 2)	0.76	0.79	0.82	0.79
Unmixing L8 L7 (date 1)	0.89	0.95	0.97	0.95
Unmixing L8 L7 (date 2)	0.88	0.94	0.97	0.92
Regression L8 C4	0.82	0.90	0.96	0.96
Regression L8 L7	0.93	0.97	0.98	0.96

regression method are in general, slightly more consistent than the ones produced by linear unmixing model approach. These results may indicate that linear unmixing approach could be propagating uncertainties produced in the endmembers extraction process, since the analyst must guarantee that the collected points do not change along the time and that they represent a pure spectral curve of the unmixing class. In the linear regression approach, the analyst supervision is not needed, since supervised sampling and pure spectres are not required, which also enables automatization of the process. Considering the image quality assessment, the Visual Information Fidelity (VIF) index (SHEIKH; BOVIK, 2006) was calculated, as shown in Table 4.3. Using this index can also be seen that Landsat-7/ETM+ data was more consistent with Landsat-8/OLI than CBERS-4/MUX data. However, through VIF the can be noted that the image quality wasn't so different using either spectral harmonization methods.

Table 4.3 - Visual Information Fidelity (VIF) index obtained by harmonizing, through linear spectral unmixing (each date separately) and linear regression (both dates) for Landsat-8/OLI (L8), Landsat-7/ETM+ (L7) and CBERS-4/MUX (C4) imagery from 04/07/2015 and 08/29/2015.

	Blue band	Green Band	Red Band	NIR Band
Unmixing L8 C4 (date 1)	0.86	0.86	0.85	0.85
Unmixing L8 C4 (date 2)	0.81	0.81	0.80	0.80
Unmixing L8 L7 (date 1)	0.95	0.95	0.94	0.93
Unmixing L8 L7 (date 2)	0.95	0.95	0.95	0.94
Regression L8 C4	0.82	0.81	0.81	0.81
Regression L8 L7	0.96	0.96	0.95	0.94

Even though Landsat-7/ETM+ and CBERS-4/MUX present bands with similar wavelengths, their spectral responses are different, as mentioned before. Landsat-8/OLI is a continuity mission of Landsat-7/ETM+ and both are processed using similar methods developed by USGS team. However, the correlation between CBERS-4/MUX and Landsat-8/OLI also showed high values, making promising to perform multi-source series to increase the number of surface observations.

Based on the obtained results and considering that no interpreters are required to perform the method, the linear regression approach will be used to perform further spectral image harmonizations on this research. Although harmonized images still contains gaps, after harmonization, the image data cube is constructed. Figure 4.1 shows the acquisition dates of the images of a set containing 81 Landsat-8/OLI, 78 Landsat-7/ETM+ and 37 CBERS-4/MUX images, used in the spectral harmonization in order to build a multi-source data cube (study area 22KEF), ranging from August 2015 to October 2017. Regarding data provenance, a table containing the gain and offset coefficients was saved alongside each image folder and for each date.

Figure 4.1 - Increase number of multisensor images used to built image data cube.
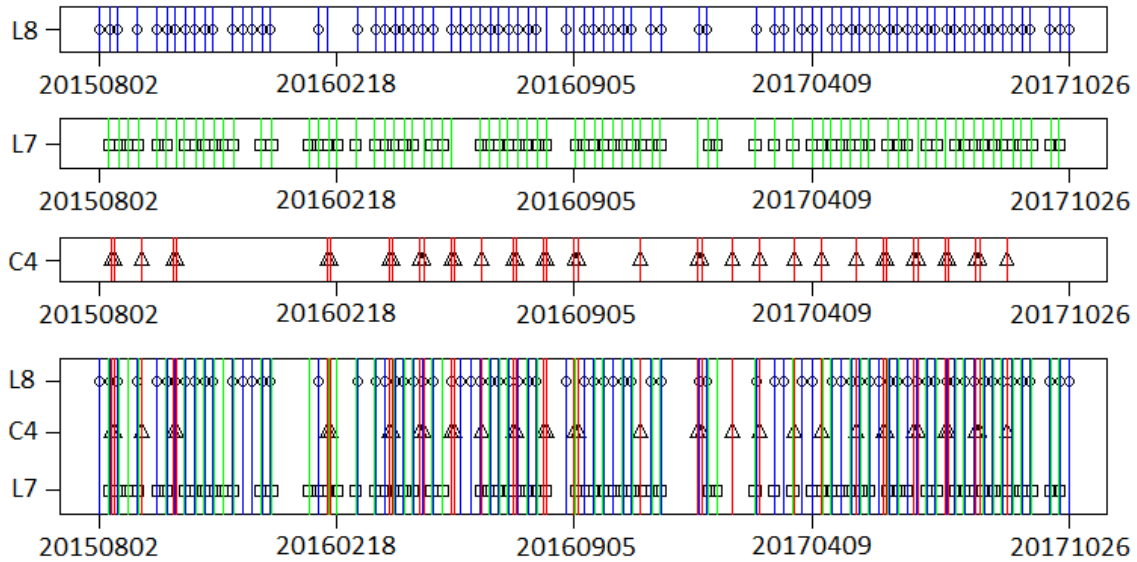
Set of 81 Landsat-8/OLI (L8), 78 Landsat-7/ETM+ (L7) and 37 CBERS-4/MUX (C4) images in blue, green and red lines, respectively, used in the spectral harmonization in order to build a multi-source data cube (study area 22KEF), ranging from August 2015 to October 2017.

Source: Author's production.

4.2 Gap-filling Through Multiscale Segmentation

The segmentation scale parameter (the algorithm merge criteria) was empirically adjusted to 50, 100, 200, respectively for levels 1, 2 and 3, whereas the compactness and shape parameters were maintained in 0.5 (which implies 0.5 for smoothness) and 0.1 (which implies in 0.9 for color), respectively, for all levels.

One of the most commonly occurring errors in the Maxwell et al. (2007) gap-filling approach is the loss of narrow features such as roads, riparian areas, and small streams. In our method these features remain detectable, since texture is maintained. This is mainly due to the pixel weighting step. In larger gaps, such as the ones found close to borders in SLC-off images, Maxwell et al. (2007) approach fills the areas as homogeneous regions due to the repetition of the same spectral value across missing values, while in our method the filled areas look visually more realistic due to the textured filling. These visual differences can be seen in Figure 4.2, which illustrates a comparison between Maxwell et al. (2007) and our method by filling the gaps of a

SLC-off Landsat-7/ETM+ using both methods. To illustrate the results of gap-filling on large scale, Figure 4.3 illustrates an entire Landsat scene presenting SLC-off gaps and the same image filled by our method, notwithstanding that this process was applied to the entire data cube.

Figure 4.2 - Gap-filling SLC-off Landsat-7/ETM+ image through two gap-filling approaches.
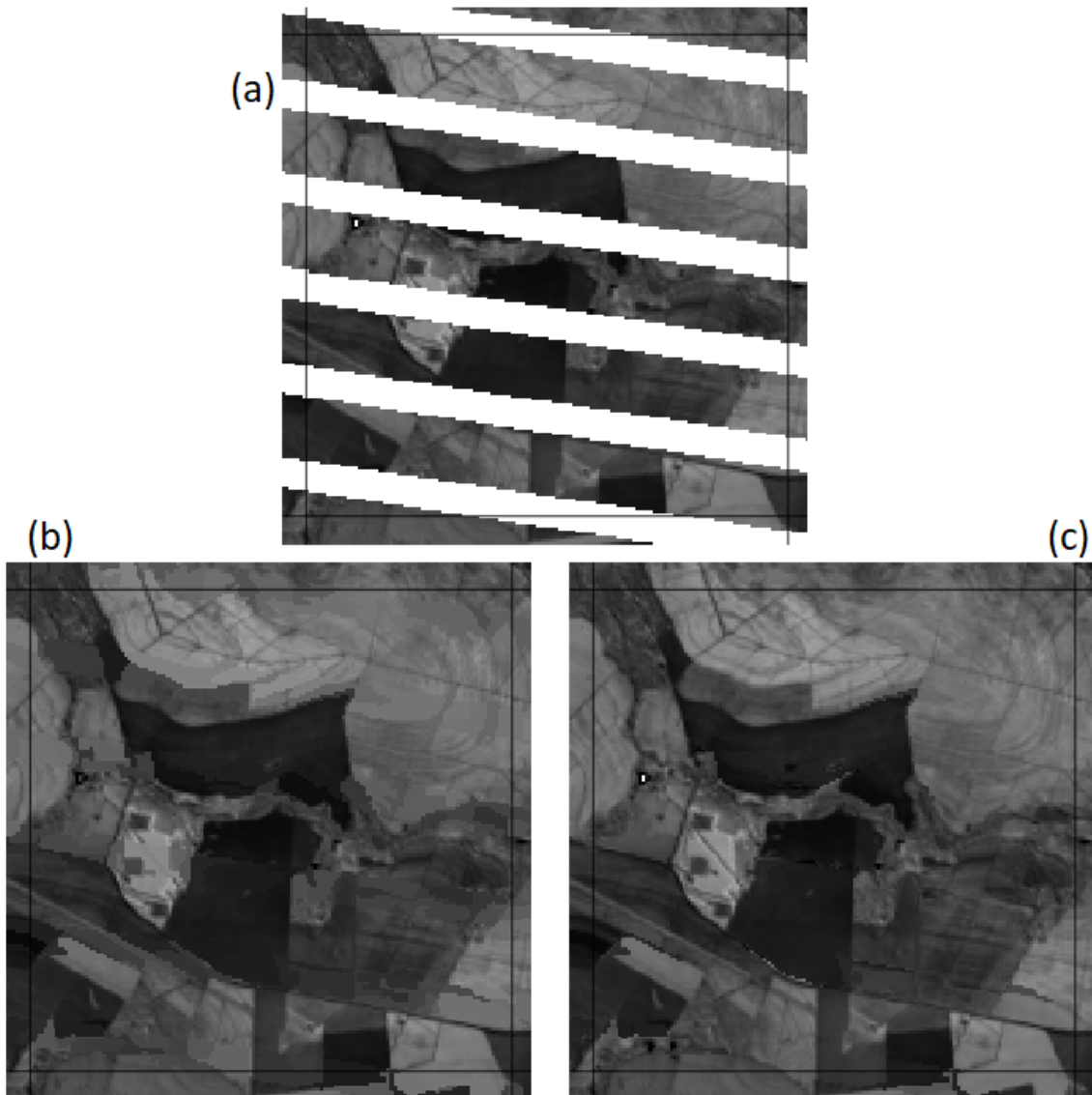
SLC-off Landsat-7/ETM+ NIR band image (a); NIR band image from "a" filled through Maxwell et al. (2007) hierarchical multi-scale segmentation method (b) and the same image from *a* filled through the proposed method, which uses segmentation pixel weighting (c).

Source: Author's production.

Figure 4.3 - Gap-filling through multiscale segmentation application in a study area.
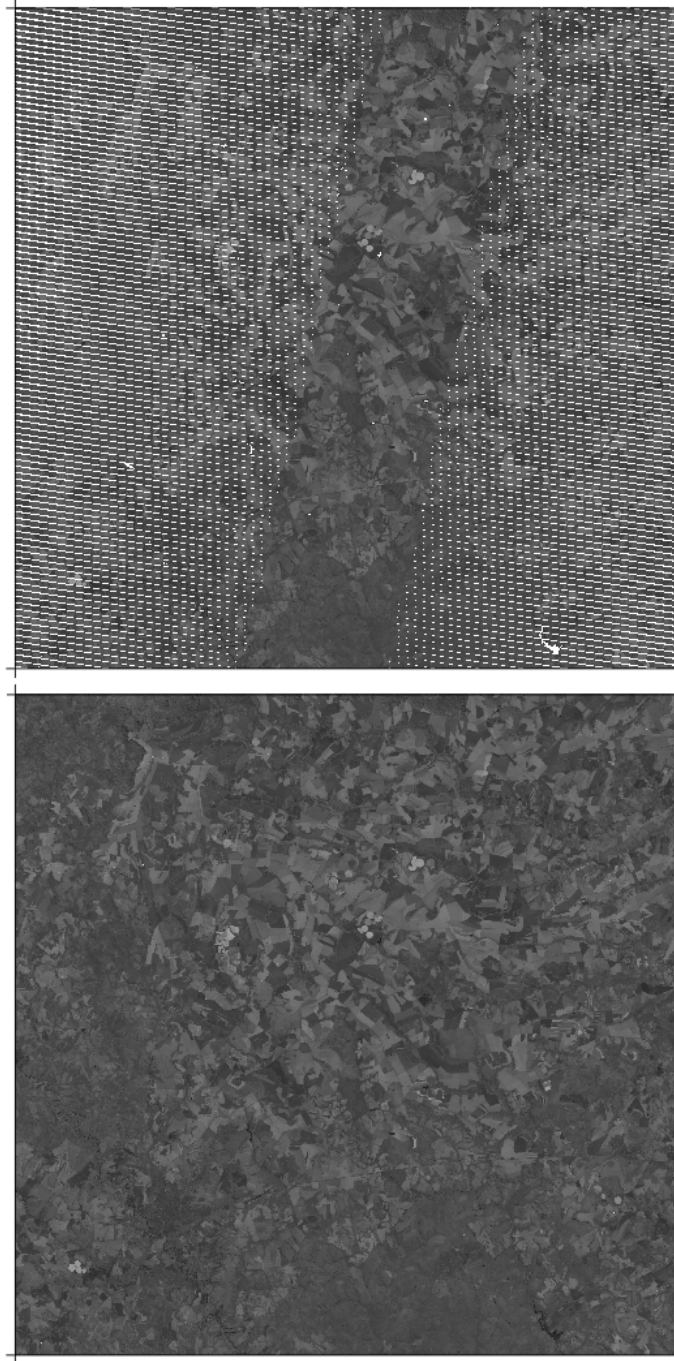
Visual comparison (NIR band) between SLC-off Landsat-7/ETM+ from 10 August 2015 (superior) and the image filled through the proposed gap-filling approach (inferior).

Source: Author's production.

To quantitatively evaluate both methods, Table 4.4 shows the agreement between Maxwell et al. (2007) (named as Maxwell) and our (named as Marujo) methods in relation to a reference. The R^2, mean absolute error (MAE) and VIF are used to evaluate the results. For all spectral bands, the R^2 obtained using our method is greater than the one using the original method, i.e. our method produces images more similar to the original ones. It the same table can also be noted that the residues (MAE) are lower using our method and that the image quality assessment is closer to the original image using our method rather than the original one.

In Table 4.4 is also possible to note that the greater the wavelength, better the correlation results, except for NIR, while the quality image (VIF) is almost constant. The crescent correlation results occurred probably due to atmospheric interference in shorter wavelength bands, also known as Rayleigh Scattering (JENSEN, 2007), that is not completely suppressed even with atmosphere correction. The differences obtained for the NIR bands probably occurred due to the differences in the sensors bandwidths and spectral response function, meaning that spectral harmonization approaches can enhance the obtained results.

Another characteristic that we noticed is that the algorithm's asymptotic cost was maintained since only linear operations were added to calculate the pixel weighting. We tested the algorithm performance using a 16Gb of memory ram and an intel processor i7-6500U of 2.5GHz computer. Figure 4.4 shows the execution time for both algorithms using images ranging from 100x100 to 2000x2000 pixels. An implementation of the method, in R, can be found in https://github.com/MarujoRe/EO_filling as *marujo_multiscale.R*.

Table 4.4 - Validation agreement between gap-filling through multiscale segmentation method (named as "Maxwell") and our method (named as "Marujo") on filling simulated SLC-off effect Landsat-8/OLI data, containing R^2, Mean Absolute Error (MAE) and Visual Information Fidelity (VIF) index.

	Dates and Metrics	Multispectral bands					
		Blue	Green	Red	NIR	SWIR 1	SWIR 2
Maxwell	Date 1 R^2	0.88	0.88	0.90	0.82	0.90	0.91
	Date 2 R^2	0.91	0.91	0.92	0.85	0.91	0.91
	Date 3 R^2	0.92	0.92	0.93	0.88	0.92	0.92
	All dates R^2	0.92	0.91	0.92	0.86	0.92	0.92
	Date 1 MAE	34.15	54.32	85.42	169.13	159.06	124.50
	Date 2 MAE	37.99	55.77	94.31	157.42	161.38	124.82
	Date 3 MAE	41.31	62.18	102.28	163.30	167.05	128.86
	All dates MAE	37.82	57.42	94.00	163.28	162.50	126.06
	Date 1 VIF	0.98	0.98	0.98	0.97	0.97	0.97
	Date 2 VIF	0.97	0.97	0.97	0.97	0.97	0.97
	Date 3 VIF	0.97	0.97	0.97	0.97	0.97	0.97
	All dates VIF	0.97	0.97	0.97	0.97	0.97	0.97
Marujo	Date 1 R^2	0.92	0.92	0.94	0.90	0.95	0.96
	Date 2 R^2	0.95	0.95	0.96	0.93	0.96	0.97
	Date 3 R^2	0.97	0.97	0.97	0.95	0.97	0.98
	All dates R^2	0.95	0.95	0.96	0.93	0.97	0.97
	All dates NRMSE	0.01	0.02	0.03	0.03	0.02	0.01
	Date 1 MAE	24.41	35.61	54.12	101.37	96.25	72.17
	Date 2 MAE	25.57	33.74	52.23	88.33	87.26	63.75
	Date 3 MAE	24.73	35.20	54.99	88.47	86.57	64.56
	All dates MAE	24.90	34.85	53.79	92.72	90.03	66.83
	Date 1 VIF	0.99	0.99	0.98	0.98	0.98	0.98
	Date 2 VIF	0.99	0.99	0.98	0.98	0.98	0.98
	Date 3 VIF	0.99	0.99	0.98	0.98	0.98	0.98
	All dates VIF	0.99	0.99	0.98	0.98	0.98	0.98

Figure 4.4 - Execution time for multiscale segmentation gap-filling algorithms.
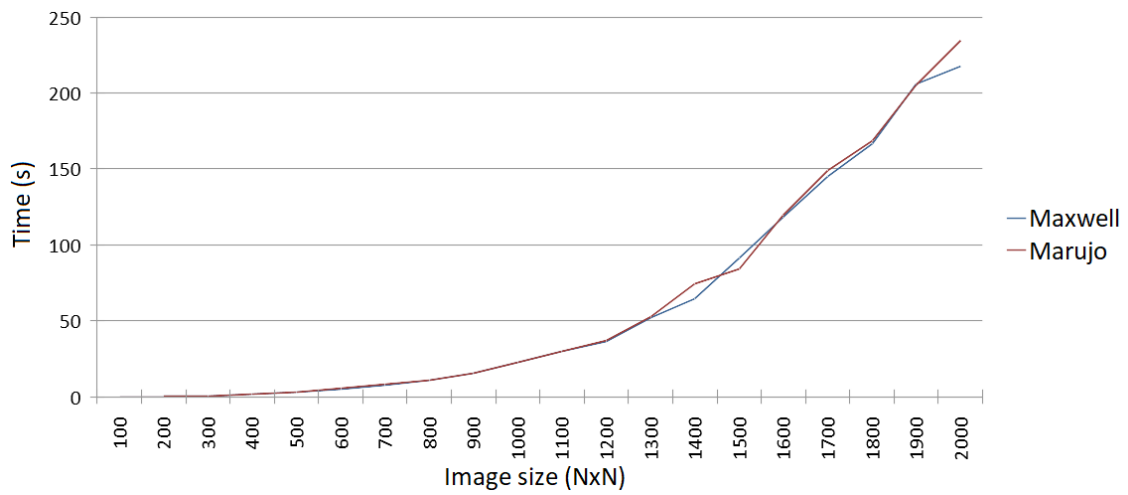
Execution time of Maxwell et al. (2007) algorithm (blue) and the proposed method (red) using images ranging from 100x100 to 2000x2000 pixels.

Source: Author's production.

4.3 Gap-filling Through Segmentation Time Series Matching

In this work, we adopted a threshold parameter of 0.03 (homogeneity criteria to merge pixels). After multi-temporal segmentation, segments with areas smaller than 7x7 pixels are merged to the biggest neighboring segment to avoid super-segmentation.

In a qualitative analysis, our method to fill gaps through segmentation time series matching, presented texture flaws as expected, since we use a single time series per segment as a template to fill the gapped time series. The filled areas appear as homogeneous regions due to the repetition of the same spectral value across missing values. The filled differences can be seen in Figure 4.5 and Figure 4.6.

Figure 4.5 compares a cloud gapped image, the same image filled through the multi-temporal segmentation times series matching and a non-gapped image from a close date. As can be noted, medium-sized gaps are filled by our method not only with temporal information but also considering the spatial context. However, the proposed gap-filling approach can affect further approaches, e.g., an object-based classification, since the filling is homogeneous and some attributes like texture can be affected. This characteristic can be more clearly observed with the existence of larger gaps, e.g., a partial image illustrated in Figure 4.6, in which can be seen that a single value is used to estimate all the missing data within a segment. To illustrate the application of our method in an entire scene, Figure 4.7 contains a partial image acquired by CBERS-4/MUX and the same image filled through our multi-temporal segmentation time series approach.

Figure 4.5 - Visual comparison between a Landsat-8/OLI image presenting gaps, the same image filled through a multi-temporal segmentation times series matching and a CBERS-4/MUX non-gapped image from a close date.
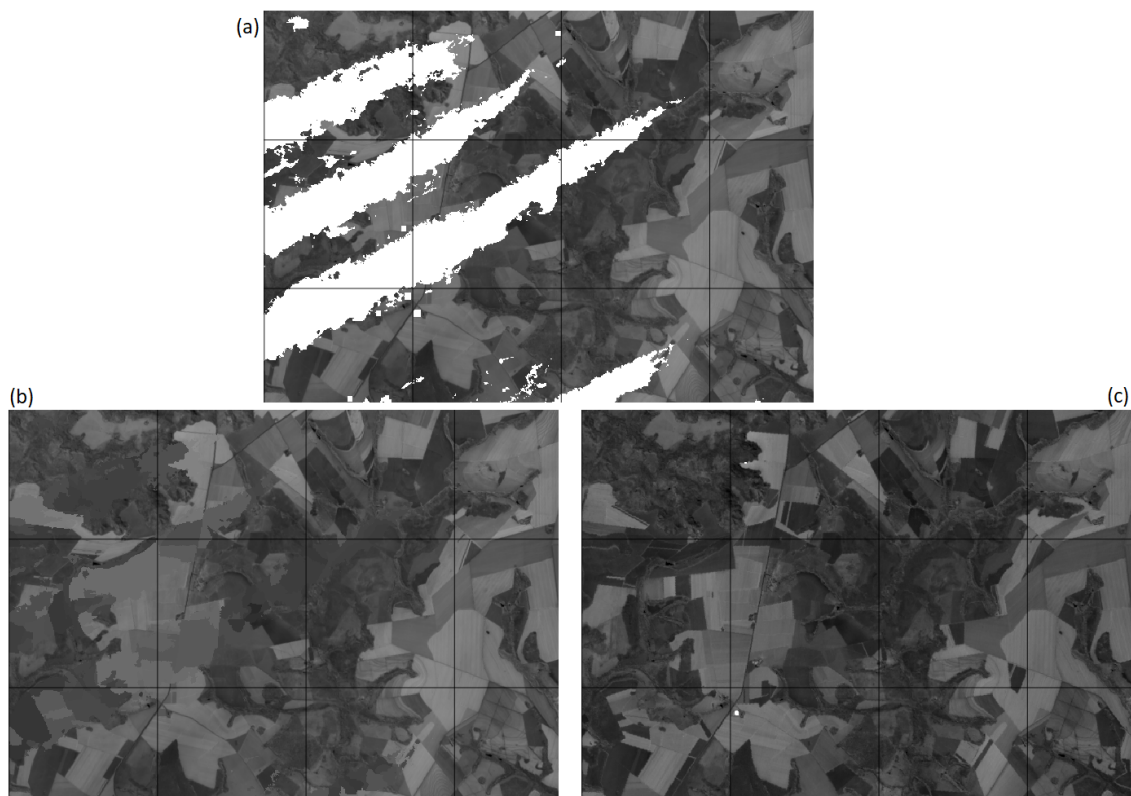
Landsat-8/OLI NIR band image, from 18 Aug 2015, presenting gaps due to cloud presence (a); the same image when applied to a gap-filling procedure through segmentation time series matching (b) and a CBERS-4/MUX image, from 12 Aug 2015, which does not contain gaps (c).

Source: Author's production.

Figure 4.6 - Visual comparison between non-gapped image and an image filled through the multi-temporal segmentation times series matching.
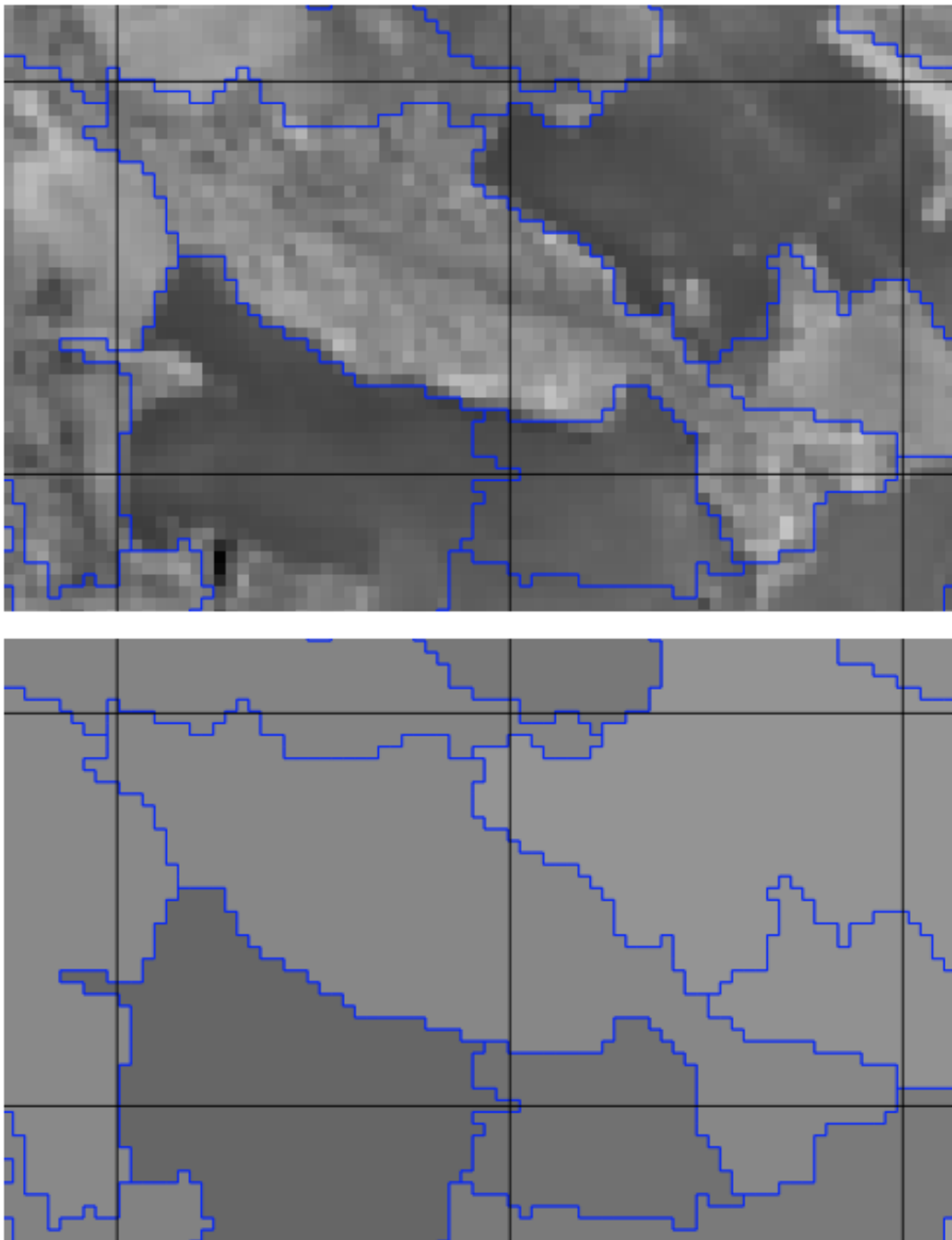
Non-gapped NIR band image from 02 Aug 2015 (superior) and gap-filled image, from 11 Aug 2015, through multi-temporal segmentation time series matching (inferior).

Source: Author's production.

Figure 4.7 - Gap-filling through segmentation time series matching application in study area 22KDF.
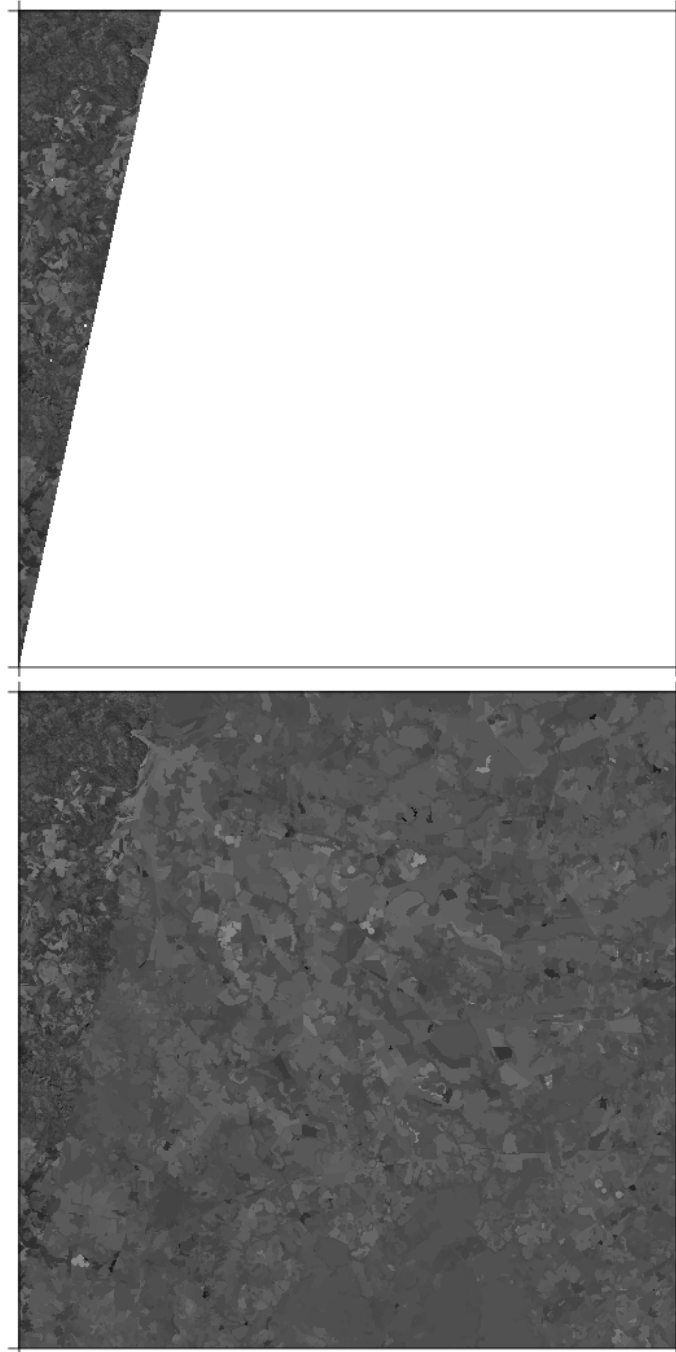
Visual comparison between partial CBERS-4/MUX NIR band image from 09 August 2015 (superior) and the image filled through our segmentation time series matching (inferior).

Source: Author's production.

Considering a time series analysis, Figure 4.8 demonstrates that our approach overcomes the lack of observations. In the figure, for three samples, can be seen two time series, a original time series (blue) and a filled time series (red). The filled time series contain all observations from the original time series while also containing the estimation of the dates in which the original time series presented gaps. As mentioned before, the estimation is performed using a reference time series obtained as the average of all time series within a segment. Periods with few observations presented changes in the time series curves due to the estimation of missing observations using the other time series from the segment. This can be better observed in sparse spots of the time series, in special the larger peak of the time series. However, the time series became noisy, probably due to differences in sensors measures, even after spectral harmonization.

In a quantitative analysis, in order to evaluate our method, Table 4.5 and 4.6 shows the agreement between the two study areas (22KDF and 22KEF) using series composed by Landsat-7/ETM+ and Landsat-8/OLI observations and also including CBERS-4/MUX data. The R^2 and MAE are utilized to evaluate the results in Table 4.5, while $UIQI$ and VIF are used in Table 4.6.

Considering the series composed by Landsat-7/ETM+ and Landsat-8/OLI on the two study areas, for 22KDF the relation between estimated and validation values were stronger than for 22KEF, in all bands. This was expected because 22KEF had more partial images, consequently more gaps, therefore, missing information implies in more uncertainty. A similar situation occurs when considering the series using the three sensors.

Considering both approaches, using two or three sensors, the relation between estimated and validation values using Landsat data is slightly greater than when including CBERS-4 data. This probably occurred because Landsat-7/ETM+ and Landsat-8/OLI data are more spectrally similar in processing than Landsat-8/OLI and CBERS-4/MUX.

Considering all cases, when including more satellite data, the Landsat-8/OLI coefficients decrease. This was probably caused due to differences in spectral measures, as we showed for CBERS-4/MUX data and according to Holden and Woodcock (2016) for Landsat-7/ETM+ data.

The red band presented the strongest relation between estimated and validation values. The NIR band presented most of the value differences. This can be explained

by the study area composition of mainly vegetation, which has a peak of values in this band.

Analysing the UIQI and VIF, the previous observations are still valid. Although UIQI presented consistent values (close to 1), this index is influenced by the gap-filling process, since the values are close to a regional mean. VIF, on the other hand, describe the image pixels variation. Considering that our method fill the gaps creating homogeneous regions, VIF presented values in the range of 0.6-0.7.

Figure 4.8 - Three samples of gapped and non-gapped time series from NIR band.
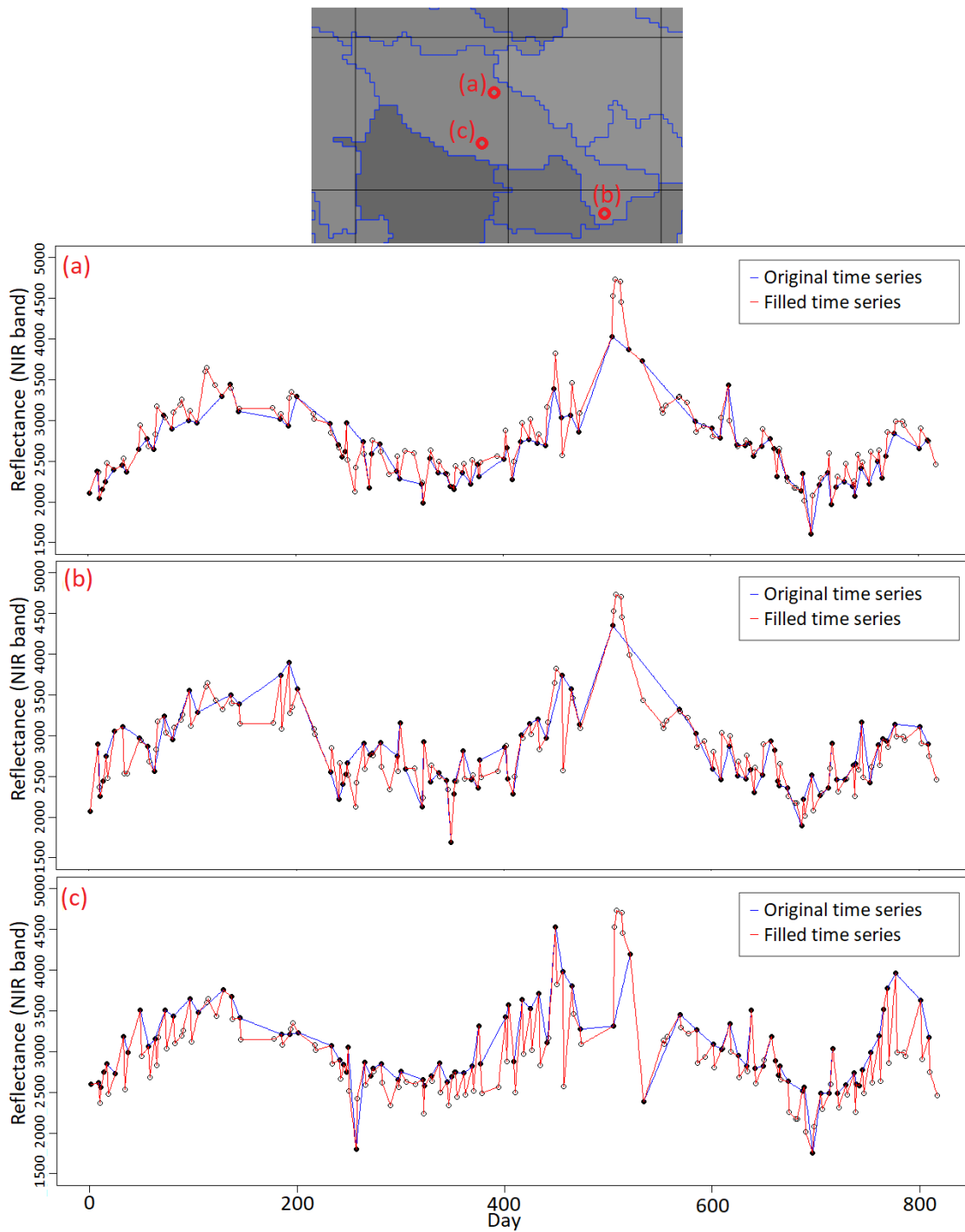
Samples, on NIR band, of non-filled time series (blue) and filled time series (red) from three regions of the same segment. Black dots are observations made from original data, while white dots are estimated by filling gaps through multi-temporal segmentation time series matching.

Source: Author's production.

Table 4.5 - Validation results using independent reference data from the four study cases. L7 refers to Landsat-7/ETM+ data, L8 refers to Landsat-8/OLI data and C4 refers to CBERS-4/MUX data. 22KDF and 22KEF are the two study areas (military grid reference system).

	Sensors and metrics	Multispectral bands					
		Blue	Green	Red	NIR	SWIR 1	SWIR 2
22KDF L7 L8	L7 R^2	0.86	0.88	0.93	0.92	0.95	0.95
	L8 R^2	0.79	0.78	0.83	0.77	0.78	0.82
	L7 L8 R^2	0.83	0.83	0.88	0.84	0.86	0.88
	L7 MAE	37.41	46.61	72.32	135.20	116.09	99.74
	L8 MAE	67.47	98.30	156.17	289.06	313.36	258.09
	L7 L8 MAE	51.91	71.54	112.76	209.41	211.24	176.12
22KDF L7 L8 C4	L7 R^2	0.85	0.88	0.94	0.91		
	L8 R^2	0.77	0.76	0.81	0.75		
	C4 R^2	0.86	0.83	0.86	0.76		
	L7 L8 C4 R^2	0.83	0.82	0.87	0.81		
	L7 MAE	37.93	46.56	69.09	132.29		
	L8 MAE	71.21	102.34	164.02	295.57		
	C4 MAE	64.92	87.37	140.04	288.40		
	L7 L8 C4 MAE	57.54	77.99	123.07	236.22		
22KEF L7 L8	L7 R^2	0.88	0.90	0.94	0.92	0.91	0.93
	L8 R^2	0.78	0.79	0.85	0.77	0.80	0.83
	L7 L8 R^2	0.78	0.79	0.85	0.77	0.80	0.83
	L7 MAE	32.48	41.39	65.12	132.66	120.65	100.11
	L8 MAE	52.11	71.25	115.47	244.90	224.55	178.68
	L7 L8 MAE	52.11	71.25	115.47	244.90	224.55	178.68
22KEF L7 L8 C4	L7 R^2	0.88	0.90	0.94	0.93		
	L8 R^2	0.69	0.69	0.75	0.57		
	C4 R^2	0.76	0.66	0.74	0.79		
	L7 L8 C4 R^2	0.77	0.75	0.82	0.76		
	L7 MAE	32.54	41.28	65.43	129.34		
	L8 MAE	74.12	105.49	173.26	373.72		
	C4 MAE	72.87	97.24	158.60	299.53		
	L7 L8 C4 MAE	57.34	78.38	127.58	262.46		

Table 4.6 - Universal Image Quality Index (UIQI) and Visual Information Fidelity (VIF) validation results using independent reference data from the four study cases. L7 refers to Landsat-7/ETM+ data, L8 refers to Landsat-8/OLI data and C4 refers to CBERS-4/MUX data. 22KDF and 22KEF are the two study areas (military grid reference system).

	Sensors and metrics	Multispectral bands					
		Blue	Green	Red	NIR	SWIR 1	SWIR 2
22KDF L7 L8	L7 *UIQI*	0.96	0.97	0.96	0.97	0.97	0.96
	L8 *UIQI*	0.94	0.95	0.93	0.97	0.96	0.94
	L7 L8 *UIQI*	0.95	0.96	0.94	0.97	0.96	0.95
	L7 *VIF*	0.67	0.70	0.67	0.70	0.70	0.67
	L8 *VIF*	0.65	0.67	0.63	0.66	0.65	0.64
	L7 L8 *VIF*	0.66	0.69	0.65	0.68	0.68	0.66
22KDF L7 L8 C4	L7 *UIQI*	0.96	0.97	0.96	0.97		
	L8 *UIQI*	0.93	0.95	0.92	0.96		
	C4 *UIQI*	0.96	0.97	0.95	0.97		
	L7 L8 C4 *UIQI*	0.95	0.96	0.95	0.97		
	L7 *VIF*	0.67	0.70	0.67	0.70		
	L8 *VIF*	0.65	0.67	0.63	0.66		
	C4 *VIF*	0.67	0.69	0.65	0.68		
	L7 L8 C4 *VIF*	0.66	0.68	0.65	0.68		
22KEF L7 L8	L7 *UIQI*	0.98	0.99	0.98	0.99	0.99	0.99
	L8 *UIQI*	0.95	0.96	0.94	0.96	0.96	0.95
	L7 L8 *UIQI*	0.97	0.98	0.96	0.98	0.97	0.97
	L7 *VIF*	0.69	0.72	0.69	0.71	0.70	0.69
	L8 *VIF*	0.66	0.67	0.64	0.66	0.66	0.64
	L7 L8 *VIF*	0.67	0.69	0.66	0.68	0.68	0.67
22KEF L7 L8 C4	L7 *UIQI*	0.98	0.99	0.98	0.99		
	L8 *UIQI*	0.94	0.96	0.93	0.96		
	C4 *UIQI*	0.94	0.95	0.93	0.96		
	L7 L8 C4 *UIQI*	0.96	0.97	0.95	0.97		
	L7 *VIF*	0.69	0.72	0.69	0.71		
	L8 *VIF*	0.66	0.67	0.64	0.66		
	C4 *VIF*	0.65	0.67	0.64	0.66		
	L7 L8 C4 *VIF*	0.67	0.69	0.66	0.68		

4.4 Final Remarks

Optical satellite sensors are affected by clouds, low temporal resolution and sensor defects, which incapacitates the Earth's surface observation. More frequently observations can be acquired by merging multiple sensors data. However, the processing of multiple sensors together presents greater challenges, than single sensor processing, due to the need for harmonization of heterogeneous data, and estimating missing

values.

This PhD thesis proposed a procedure to build a landsat-like satellite sensor image data cube, in which Landsat-7/ETM+, Landsat-8/OLI and CBERS-4/MUX were evaluated. In order to do that, two methodologies to harmonize data were evaluated and two methods for reconstructing missing data were proposed. The methodology to harmonize images from different optical sensors and reconstruct missing Earth's surface observation data was applied to two different study areas. Two case studies were conducted considering two extreme scenarios, the first one when a study area tile is fully contained in the sensor path/row and the second case when the study area is in bordering path/row regions, resulting in more partial images.

The spectral harmonization results showed that Landsat-8/OLI, Landsat-7/ETM+ and CBERS-4/MUX can be used together once their images are harmonized. Among the studied approaches, the harmonization through linear regression presented better results to harmonize data from the mentioned sensors. As a direct consequence of the harmonization, more images populated the image date cube, which overcame the Landsat original temporal resolution of 16 days. However, missing data still needed to be estimated due to gaps.

In order to reconstruct Earth observations we sequentially employed two approaches. The first one, an adaptation on Maxwell et al. (2007) multiscale segmentation gap-filling approach to use segmentation pixel weighting instead of most frequent value only. This method was mainly used to fill small image gaps, such as Landsat-7/ETM+ SLC-off effect. The second approach was inspired in Vuolo et al. (2017), which uses a previous time series library to reconstruct gapped ones through an euclidean distance comparison. In our method, we use a multi-temporal segmentation (COSTA et al., 2018) to estimate homogeneous areas and extract a time series of this area to serve as reference to fill gaps.

Our multiscale segmentation gap-filling method enhanced the original Maxwell et al. (2007) method, while asymptotically maintaining the algorithm cost. Our approach allowed image texture to be conserved on reconstructed images, allowing object based analysis to be further applied on Landsat-7/ETM+ images. Another improvement was that narrow features, e.g., roads, riparian areas, and small streams, remained detectable in reconstructed images.

In our multi-temporal segmentation approach, the main advantage is that it allows the reconstruction of areas without the need of a previous classification, since the

segmentation guarantee that. However, a peculiarity of our approach is that the reconstructed regions are filled with a single value per segment. Based on that, analysts must consider using the method, since it will not provide close-to-reality texture on the reconstructed regions.

Multi-source and Earth's surface observation reconstruction can continue to be improved. Considering the importance of monitoring Earth's surface, this research shows the potential to improve multi-source data quality and temporal frequency of orbital images time series. A wide of applications can benefit from that and initiatives can benefit collaborative data.

A total of 274,000,819 pixels were reconstructed through our multiscale segmentation, almost 1.92% of the entire image data cube. A total of 6,245,114,365 pixels were reconstructed through our multi-temporal segmentation time series matching approach, the equivalent of 43.64% of the entire image data cube.

In summary, we managed to provide two image data cubes of 100km x100km containing two years of images, ranging from August 2015 to October 2017, from Landsat-7/ETM+, Landsat-8/OLI and CBERS-4/MUX sensors, with a spatial resolution of 30m. A total of 274,000,819 pixels were reconstructed through our multiscale segmentation, almost 1.92% of the entire image data cube. A total of 6,245,114,365 pixels were reconstructed through our multi-temporal segmentation time series matching approach, the equivalent of 43.64% of the entire image data cube. Two examples of the methodology application can be seen in Figure 4.9, which demonstrate Landsat-7/ETM+ SLC-off image gaps being filled, through the multiscale segmentation approach and the remaining gaps being filled through the multi-temporal segmentation approach.

This research served to the publication and collaboration of several papers. Bendini et al. (2016) and Bendini et al. (2017) are assessment studies regarding the use of Landsat and CBERS imagery together. Marujo et al. (2017b) consists of initial tests regarding Maxwell et al. (2007) method application on Landsat-8/OLI images, since the original method was applied in Landsat-5/TM images. Marujo et al. (2017c) is an initial study regarding CBERS-4/MUX cloud detection based on Silva and Liporace (2016) approach to detect clouds in Amazonia-1 sensor. Marujo et al. (2017a) is a initial comparison of the linear regression and linear unmixing spectral harmonizations. Two papers are still being prepared for publishing, one regarding our multiscale segmentation gap-filling method and the other regarding the multi-temporal segmentation approach.

Figure 4.9 - Example of two Landsat-7/ETM+ SLC-off image gaps on NIR band, being filled through multiscale segmentation approach and multi-temporal segmentation approach.
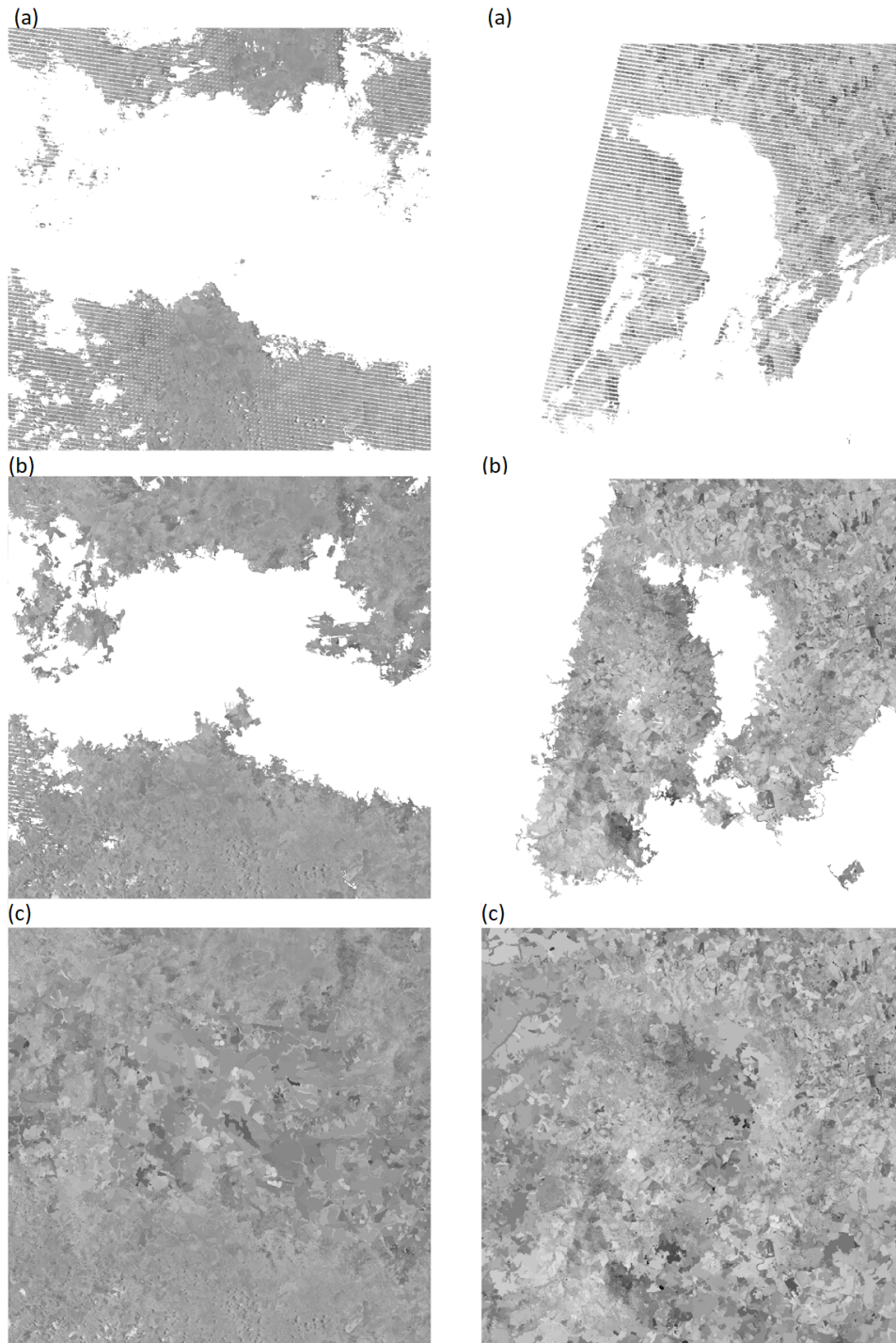
(a) Landsat-7/ETM+ SLC-off images; (b) the same images after multiscale segmentation gap-filling approach; and (c) after multi-temporal segmentation gap-filling.

Source: Author's production.

5 CONCLUSION

Different sensors image harmonization continues to be a topic of intense research and its development will lead to more effective approaches on monitoring the Earth's surface. Considering Landsat-7/ETM+, Landsat-8/OLI and CBERS-4/MUX sensors and the two harmonization methodologies tested in this research, spectral unmixing and linear regression, both approaches presented Pearson's correlation coefficients greater than 0.76 for all spectral bands. However, the linear regression approach results were more consistent in all bands, more used in the literature and easier to automatize, based on that it was chosen as the method to harmonize images from multiple sensors.

Considering the reconstruction of Earth's surface data, our multiscale segmentation gap-filling method enhanced the original method, while asymptotically maintaining the algorithm cost, notwithstanding that this approach was applied to the entire image data cube, instead of a single pair of images. Our approach allowed image texture to be conserved on reconstructed images, allowing object based analysis to be further applied on Landsat-7/ETM+ images. Another improvement was that narrow features, e.g., roads, riparian areas, and small streams, remained detectable in reconstructed images. Considering the VIF index, the method presented values greater than 0.97 for the gap-filling through multiscale segmentation, presenting better results than the original method in which it was inspired.

In our multi-temporal segmentation approach, the main advantage is that it allows the reconstruction of areas without the need of a previous classification, since the segmentation guarantee that. However, a peculiarity of our approach is that the reconstructed regions are filled with a single value per segment. Based on that, analysts must consider using the method, since it will not provide close-to-reality texture on the reconstructed regions. Considering all tested sensors and the different study areas, the least $UIQI$ obtained was 0.92 and a VIF ranging from 0.6 to 0.7 on the final method. Although the mentioned texture issue, the results points that the harmonized and reconstructed areas are very similar to the original data, showing the feasibility of the methodology.

Pragmatically, it is expected that the approach developed in this thesis can be used effectively in academic and industrial environments and henceforth contribute to improves overall multi-source harmonization and Earth observation data reconstruction. The developed codes are open source, free and published so it can be used or adapted, as is all its dependencies. The R version can be found in

77

5.1 Suggestions for Future Research

- Develop an approach capable of estimating the texture variance in multi-temporal segmentation time series matching approach;

- Expand the image data cube number of imaging sensors, such as Sentinel or other landsat-like sensors;

- Apply the developed methodology in regions with fewer Earth's surface observations, e.g. regions that are more affected by the presence of clouds such as the Amazon.

REFERENCES

ABREU, E. S.; FONSECA, L. M. G.; SANTOS, C. P. F. dos; RIBEIRO, V. O. "Cloud Detection Tool" - uma ferramenta para a detecção de nuvens e sombras em imagens de satélite. In: SIMPÓSIO BRASILEIRO DE SENSORIAMENTO REMOTO, 16., 2013, Foz do Iguaçu, Brazil. **Anais...** São José dos Campos: INPE, 2013. p. 4234–4241. ISBN 978-85-17-00066-9. Available from: <`http://marte2.sid.inpe.br/col/dpi.inpe.br/marte2/2013/05.29.00.32.13/doc/p1188.pdf`>. 12, 17

ADAMI, M.; BERNARDES, S.; ARAI, E.; FREITAS, R. M.; SHIMABUKURO, Y. E.; ESPÍRITO-SANTO, F. D.; RUDORFF, B. F.; ANDERSON, L. O. Seasonality of vegetation types of South America depicted by moderate resolution imaging spectroradiometer (MODIS) time series. **International Journal of Applied Earth Observation and Geoinformation**, v. 69, n. 1, p. 148–163, 2018. ISSN 03032434. Available from: <`http://linkinghub.elsevier.com/retrieve/pii/S0303243418301740`>. 42

AMORÓS-LÓPEZ, J.; GÓMEZ-CHOVA, L.; ALONSO, L.; GUANTER, L.; ZURITA-MILLA, R.; MORENO, J.; CAMPS-VALLS, G. Multitemporal fusion of Landsat/TM and ENVISAT/MERIS for crop monitoring. **International Journal of Applied Earth Observation and Geoinformation**, v. 23, n. 1, p. 132–141, 2013. ISSN 15698432. Available from: <`http://dx.doi.org/10.1016/j.jag.2012.12.004`>. 4, 27

AUSTRALIAN GEOSCIENCE. **Australian Geoscience Data Cube**. 2015. Available from: <`http://www.datacube.org.au/wiki/Main_Page`>. Access in: 07 Feb. 2017. 34, 35

BAATZ, M.; SCHÄPE, A. Multiresolution segmentation: an optimization approach for high quality multi-scale image segmentation. In: ANGEWANDTE GEOGRAPHISCHE INFORMATIONSVERARBEITUNG, 12. **Proceedings...** Heidelberg, 2000. p. 12–23. Available from: <`http://www.ecognition.com/sites/default/files/405_baatz_fp_12.pdf`>. 22, 23, 42

BANSKOTA, A.; KAYASTHA, N.; FALKOWSKI, M. J.; WULDER, M. A.; FROESE, R. E.; WHITE, J. C. Forest monitoring using Landsat time series data: a review. **Canadian Journal of Remote Sensing**, v. 40, n. 5, p. 362–384, 2014. ISSN 0703-8992. 1

BAUMANN, M.; OZDOGAN, M.; RICHARDSON, A. D.; RADELOFF, V. C. Phenology from Landsat when data is scarce: using MODIS and Dynamic Time-Warping to combine multi-year Landsat imagery to derive annual phenology curves. **International Journal of Applied Earth Observation and Geoinformation**, v. 54, p. 72–83, 2017. ISSN 03032434. 16, 18

BEHLING, R.; ROESSNER, S.; GOLOVKO, D.; KLEINSCHMIT, B. Derivation of long-term spatiotemporal landslide activity - a multi-sensor time series approach. **Remote Sensing of Environment**, v. 186, p. 88–104, 2016. ISSN 00344257. 25

BEHLING, R.; ROESSNER, S.; SEGL, K.; KLEINSCHMIT, B.; KAUFMANN, H. Robust automated image co-registration of optical multi-sensor time series data: database generation for multi-temporal landslide detection. **Remote Sensing**, v. 6, n. 3, p. 2572–2600, 2014. ISSN 20724292. 9

BENDINI, H. d. N.; FONSECA, L. M. G.; KÖRTING, T. S.; SANCHES, I. D. A.; MARUJO, R. F. B. Evaluation of smoothing methods on Landsat-8 EVI time series for crop classification based on phenological parameters. In: SIMPÓSIO BRASILEIRO DE SENSORIAMENTO REMOTO, 18., 2017, Santos, Brazil. **Anais...** São José dos Campos: INPE, 2017. p. 4267–4274. ISBN 978-85-17-00088-1. 1, 75

BENDINI, H. N.; FONSECA, L. M. G.; KÖRTING, T. S.; MARUJO, R. F. B. Assessment of a multi-sensor approach for noise removal on OLI/LANDSAT-8 time series using MUX/CBERS-4 data to improve a crop classification method based on phenological features. In: SIMPÓSIO BRASILEIRO DE GEOINFORMÁTICA, 17., 2016, Campos dos Jordão, Brazil. **Anais...** São José dos Campos: INPE, 2016. p. 12. 17, 26, 27, 28, 75

BÉNIÉ, G.; THOMSON, K.; GOLDBERG, M. A comparison of four segmentation algorithms in the context of agricultural remote sensing. **ISPRS Journal of Photogrammetry and Remote Sensing and Remote Sensing**, v. 44, p. 1–13, 1989. Available from: <http://www.sciencedirect.com/science/article/pii/0924271689900257>. 22

BERGER, M.; MORENO, J.; JOHANNESSEN, J. A.; LEVELT, P. F.;
HANSSEN, R. F. Esa's sentinel missions in support of earth system science.
Remote Sensing of Environment, v. 120, p. 84 – 90, 2012. ISSN 0034-4257.
Available from: <http:
//www.sciencedirect.com/science/article/pii/S003442571200065X>. 1

BERNDT, D. J.; CLIFFORD, J. Using dynamic time warping to find patterns in
time series. In: INTERNATIONAL CONFERENCE ON KNOWLEDGE
DISCOVERY AND DATA MINING, 3., 1994, Seattle, WA. **Proceedings...**
Seattle, WA: AAAI Press, 1994. p. 359–370. Available from:
<http://dl.acm.org/citation.cfm?id=3000850.3000887>. 18

BLASCHKE, T.; LANG, S.; LORUP, E.; STROBL, J.; ZEIL, P. Object-oriented
image processing in an integrated GIS / remote sensing environment and
perspectives for environmental applications. **Umweltinformation für Planung,
Politik und Öffentlichkeit**, n. 1995, p. 555–570, 2000. 22

BRAGA, B. C.; JOÃO, S.; SANT, S.; FREITAS, C. Distâncias estocásticas e
mapas de incertezas aplicados à classificação de dados de múltiplos sensores.
Revista Brasileira de Cartografia, v. 67, n. 7, p. 1391–1411, 2015. 25

CALLIECO, F.; DELL'ACQUA, F. A comparison between two radiative transfer
models for atmospheric correction over a wide range of wavelengths.
International Journal of Remote Sensing, v. 32, n. 1, p. 1357–1370, 2011.
ISSN 0143-1161. 11

CEOS. **CEOS data cube platform**. 2016. Available from:
<https://software.nasa.gov/featuredsoftware/ceos2>. Access in: 07 Feb.
2017. 35

_____. **The CEOS data cube: three-year work plan 2016 - 2018**. 2016.
Available from: <http://ceos.org/document_management/Meetings/Plenary/
30/Documents/5.3_Killough_Cube-3-Year-Work-Plan_v1.1.pdf>. Access in:
07 Feb. 2017. 35

CHANDER, G.; MARKHAM, B. L.; HELDER, D. L. Summary of current
radiometric calibration coefficients for Landsat MSS, TM, ETM+, and EO-1 ALI
sensors. **Remote Sensing of Environment**, v. 113, n. 5, p. 893–903, 2009. ISSN
00344257. Available from: <http://dx.doi.org/10.1016/j.rse.2009.01.007>.
10, 11

CLAVERIE, M.; JU, J.; MASEK, J. G.; DUNGAN, J. L.; VERMOTE, E. F.; ROGER, J.-C.; SKAKUN, S. V.; JUSTICE, C. The harmonized landsat and sentinel-2 surface reflectance data set. **Remote Sensing of Environment**, v. 219, p. 145 – 161, 2018. ISSN 0034-4257. Available from: <http://www.sciencedirect.com/science/article/pii/S0034425718304139>. 3

COHEN, W. B.; GOWARD, S. N. Landsat's role in ecological applications of remote sensing. **BioScience**, v. 54, n. 6, p. 535–546, 2004. 7, 16

COPPIN, P.; JONCKHEERE, I.; NACKAERTS, K.; MUYS, B.; LAMBIN, E. Digital change detection methods in ecosystem monitoring: a review. **International Journal of Remote Sensing**, v. 25, n. 9, p. 1565–1596, 2004. ISSN 0143-1161. 1, 15, 25

COSTA, W. S.; FONSECA, L. M. G.; KÖRTING, T. S.; BENDINI, H. d. N.; SOUZA, R. C. M. de. Spatio-temporal segmentation applied to optical remote sensing image time series. **IEEE Geoscience and Remote Sensing Letters**, v. 15, n. 8, p. 1299–1303, Aug 2018. ISSN 1545-598X. 24, 42, 47, 74

DALMIYA, C. P.; DHARUN, V. S. A survey of registration techniques in remote sensing images. **Indian Journal of Science and Technology**, v. 8, n. 26, p. 1–7, oct 2015. ISSN 0974-5645. Available from: <http://www.indjst.org/index.php/indjst/article/view/81048>. 9

DEFINIENS IMAGING GMBH. **eCognition user guide**. Munich, Germany: GmbH Definiens Imaging, 2002. Available from: <http://www.irfanakar.com/GIS_Remote_Sensing_files/eCognition%20Definiens/Elementd%204.0%20User%20Guide.pdf>. 22

DI, L.; YUE, P.; RAMAPRIYAN, H. K.; KING, R. L. Geoscience data provenance: an overview. **IEEE Transactions on Geoscience and Remote Sensing**, v. 51, n. 11, p. 5065–5072, nov 2013. ISSN 0196-2892. Available from: <http://ieeexplore.ieee.org/document/6471200/>. 35

DWYER, J.; LYMBURNER, L. **Analyses ready data**. 2016. Available from: <https://landsat.usgs.gov/sites/default/files/documents/USGS%20Analysis%20Ready%20Data.pdf>. 34

EHLERS, M.; JANOWSKY, R.; GAEHLER, M. New remote sensing concepts for environmental monitoring. **Remote Sensing for Environmental Monitoring**, v. 4545, p. 1–12, 2002. ISSN 0277786X. 1

EHLERS, R. S. **Análise de séries temporais**. 2009. Available from: <http://www.icmc.usp.br/pessoas/ehlers/stemp/>. Access in: 13 Aug. 2017. 1, 16

ENVI. **ENVI atmospheric correction module: QUAC and FLAASH user's guide**. Colorado, 2009. 44 p. Available from: <ftp://popo.jpl.nasa.gov/pub/ENVI_Installers/ENVI_Documentation/docs/FLAASH_Module.pdf>. 11

ERASMI, S.; BOTHE, M.; PETTA, R. Enhanced filtering of modis time series data for the analysis of desertification processes in northeast brazil. In: ISPRS/ITC-MIDTERM SYMPOSIUM: REMOTE SENSING: FROM PIXELS TO PROCESSES, 36., 2006, Enschede, The Netherlands. **Proceedings...** Enschede, The Netherlands: GEOWAY, 2006. p. 8–11. 17

ESPINDOLA, G. M. D. **Ajuste de parâmetros em algoritmos de segmentação de imagens por crescimento de regiões**. 55 p. INPE-14659-TDI/1215. Dissertação (Mestrado Sensoriamento Remoto) — Instituto Nacional de Pesquisas Espaciais (INPE), São José dos Campos, 2007. Available from: <http://urlib.net/rep/6qtX3pFwXQZGivnJSY/NwtLS?ibiurl.language=pt-BR>. Access in: 19 Ago. 2018. 22, 23, 24

FOGA, S.; DAVIS, B.; SAUER, B.; DWYER, J. **The future of landsat data products: analysis ready data and essential climate variables**. 2016. Available from: <https://gsa.confex.com/gsa/2016AM/webprogram/Handout/Paper285613/foga_gsa_presentation_FINAL.pdf>. 34

FONSECA, L. M. G.; MANJUNATH, B. S. Registration techniques for multisensor remotely sensed imagery. **Photogrammetric Engineering & Remote Sensing**, v. 62, n. 9, p. 1049–1056, 1996. ISSN 00991112. 8

GAO, F.; MASEK, J.; SCHWALLER, M.; HALL, F. On the blending of the landsat and MODIS surface reflectance: predicting daily landsat surface reflectance. **IEEE Transactions on Geoscience and Remote Sensing**, v. 44, n. 8, p. 2207–2218, 2006. ISSN 01962892. 4, 27

GEVAERT, C. M.; GARCÍA-HARO, F. J. A comparison of STARFM and an unmixing-based algorithm for Landsat and MODIS data fusion. **Remote Sensing of Environment**, v. 156, p. 34–44, jan 2015. ISSN 00344257. Available from: <http://dx.doi.org/10.1016/j.rse.2014.09.012>. 4, 28

GÓMEZ, C.; WHITE, J. C.; WULDER, M. A. Optical remotely sensed time series data for land cover classification: a review. **ISPRS Journal of Photogrammetry and Remote Sensing**, v. 116, p. 55–72, 2016. ISSN 09242716. 2, 16, 17

GONZALEZ, R. C.; WOODS, R. E. **Digital image processing (3 .ed.)**. Upper Saddle River, NJ, USA: Pearson, 2007. 976 p. ISSN 1098-6596. ISBN 013168728X. 22

GU, Y.; REN, K.; WANG, P.; GU, G. Polynomial fitting-based shape matching algorithm for multi-sensors remote sensing images. **Infrared Physics and Technology**, v. 76, p. 386–392, 2016. ISSN 13504495. Available from: <http://dx.doi.org/10.1016/j.infrared.2016.03.019>. 9

HERMOSILLA, T.; WULDER, M. A.; WHITE, J. C.; COOPS, N. C.; HOBART, G. W. An integrated Landsat time series protocol for change detection and generation of annual gap-free surface reflectance composites. **Remote Sensing of Environment**, v. 158, p. 220–234, mar 2015. ISSN 00344257. 29, 35

HIRD, J. N.; MCDERMID, G. J. Noise reduction of ndvi time series: an empirical comparison of selected techniques. **Remote Sensing of Environment**, v. 113, n. 1, p. 248 – 258, 2009. ISSN 0034-4257. Available from: <http://www.sciencedirect.com/science/article/pii/S0034425708002745>. 42

HOLDEN, C. E.; WOODCOCK, C. E. An analysis of Landsat 7 and Landsat 8 underflight data and the implications for time series investigations. **Remote Sensing of Environment**, v. 185, p. 16–36, 2016. ISSN 00344257. 3, 4, 27, 29, 55, 69

HOLLANDS, T.; DIERKING, W. Dynamics of the Terra Nova Bay Polynya: the potential of multi-sensor satellite observations. **Remote Sensing of Environment**, v. 187, p. 30–48, 2016. ISSN 00344257. Available from: <http://dx.doi.org/10.1016/j.rse.2016.10.003>. 25

HUBBARD, B. E.; CROWLEY, J. K. Mineral mapping on the Chilean-Bolivian Altiplano using co-orbital ALI, ASTER and Hyperion imagery: data dimensionality issues and solutions. **Remote Sensing of Environment**, v. 99, n. 1-2, p. 173–186, nov 2005. ISSN 00344257. Available from: <http://linkinghub.elsevier.com/retrieve/pii/S0034425705001781>. 27

HUETE, A. R.; LIU, H. Q.; BATCHILY, K.; LEEUWEN, W. V. A comparison of vegetation indices over a global set of TM images for EOS-MODIS. **Remote Sensing of Environment**, v. 59, n. 3, p. 440–451, 1997. ISSN 00344257. 16

INSTITUTO NACIONAL DE PESQUISAS ESPACIAIS - INPE. **Deforestation estimates in the Brazilian Amazon (PRODES)**. 2002. Available from: <http://www.obt.inpe.br/prodes/>. Access in: 13 Jan. 2017. 28

JENSEN, J. **Remote sensing of the environment: an Earth resource perspective**. New Jersey: Pearson Prentice Hall, 2007. 592 p. (Prentice Hall series in geographic information science). ISBN 9780131889507. 7, 8, 10, 11, 26, 55, 62

KEOGH, E.; RATANAMAHATANA, C. A. Exact indexing of dynamic time warping. **Knowledge and Information Systems**, v. 7, n. 3, p. 358–386, mar 2005. ISSN 0219-1377. Available from: <http://link.springer.com/10.1007/s10115-004-0154-9>. 18, 19

KÖRTING, T. S.; FONSECA, L. M. G.; CâMARA, G. Geodma—geographic data mining analyst. **Computers & Geosciences**, v. 57, p. 133 – 145, 2013. ISSN 0098-3004. Available from: <http://www.sciencedirect.com/science/article/pii/S0098300413000538>. 22

KUENZER, C.; DECH, S.; WAGNER, W. **Remote sensing time series**. Cham: Springer International, 2015. 458 p. (Remote Sensing and Digital Image Processing, v. 22). ISBN 978-3-319-15966-9. 1, 3, 16, 17

LE MOIGNE, J.; NETANYAHU, N. S.; EASTMAN, R. D. Introduction. In: _____ (Ed.). **Image registration for remote sensing**. Cambridge: University Press, 2010. p. 3–23. ISBN 9780511777684. 9

LEFSKY, M. A.; COHEN, W. B. Selection of remotely sensed data. In: WULDER, M.; FRANKLIN, S. E. (Ed.). **Remote sensing of forest environments**. Norwell Massachusetts, USA: Academic Press, 2003. p. 13–46. ISBN 978-1-4615-0306-4. 1

LEVENSHTEIN, V. I. Binary codes capable of correcting deletions, insertions, and reversals. **Soviet Physics Doklady**, v. 10, n. 8, p. 707–710, 1966. ISSN 00385689. 18

LI, M.; ZANG, S.; ZHANG, B.; LI, S.; WU, C. A review of remote sensing image classification techniques: the role of spatio-contextual information. **European Journal of Remote Sensing**, v. 47, n. 1, p. 389–411, 2014. ISSN 22797254. 15, 22

LOU, Q.; OBRADOVIC, Z. Modeling multivariate spatio-temporal remote sensing data with large gaps. In: INTERNATIONAL JOINT CONFERENCE ON ARTIFICIAL INTELLIGENCE, 22., 2011, Barcelona, Spain. **Proceedings...** AAAI PRESS, 2011. p. 1711–1716. Available from: <http://www.dabi.temple.edu/~zoran/papers/lou11.pdf>. 30

MARTINS, V. S.; SOARES, J. V.; NOVO, E. M.; BARBOSA, C. C.; PINTO, C. T.; ARCANJO, J. S.; KALEITA, A. Continental-scale surface reflectance product from cbers-4 mux data: assessment of atmospheric correction method using coincident landsat observations. **Remote Sensing of Environment**, v. 218, p. 55 – 68, 2018. ISSN 0034-4257. Available from: <http://www.sciencedirect.com/science/article/pii/S0034425718304280>. 38

MARUJO, R. F. B.; FONSECA, L. M.; KÖRTING, T. S. Spectral normalization between Landsat-8 / OLI , Landsat- 7 / ETM + and CBERS-4 / MUX bands through linear regression and spectral unmixing. In: SIMPÓSIO BRASILEIRO DE GEOINFORMÁTICA, 18., 2017, Salvador, Brazil. **Anais...** São José dos Campos: INPE, 2017. p. 10. Available from: <http://mtc-m16c.sid.inpe.br/col/sid.inpe.br/mtc-m16c/2017/12.01.20.02/doc/35marujo{_}bendini.pdf>. 55, 75

MARUJO, R. F. B.; FONSECA, L. M. G.; KÖRTING, T.; BENDINI, H.; QUEIROZ, G.; VINHAS, L.; FERREIRA, K. Remote sensing image processing functions in Lua language. **Journal of Computational Interdisciplinary Sciences**, v. 8, n. 3, p. 1–14, 2017. ISSN 1983-8409. Available from: <http://epacis.net/jcis/PDF{_}JCIS/JCIS11-art.0133.pdf>. 75

MARUJO, R. F. B.; FONSECA, L. M. G.; KÖRTING, T. S.; SANTOS, R. D. C. dos; BENDINI, H. d. N. CBERS-4/MUX automatic detection of clouds and cloud shadows using decision trees. In: SIMPÓSIO BRASILEIRO DE SENSORIAMENTO REMOTO, 18., 2017, Santos, Brazil. **Anais...** São José dos Campos: INPE, 2017. p. 6328–6335. ISBN 9788517000881. Available from: <http://marte2.sid.inpe.br/rep/sid.inpe.br/marte2/2017/10.27.15.45.15>. 12, 38, 75

MARUJO, R. F. B.; MARIN, M.; VOLPATO, L.; MARIA, H.; ALVES, R. Mapeamento da cultura cafeeira por meio de classificação automática utilizando atributos espectrais, texturais e fator de iluminação. **Coffee Science**, v. 12, n. 2, p. 17–28, 2017. Available from: <http://coffeescience.ufla.br/index.php/Coffeescience/article/view/1176/pdf{_}1176>. 1

MAUS, V.; CÂMARA, G.; APPEL, M.; PEBESMA, E. dtwSat: time-weighted dynamic time warping for satellite image time series analysis in R. **Journal of Statistical Software**, v. 8, n. 5, 2016. 19

MAUS, V.; CâMARA, G.; CARTAXO, R.; SANCHEZ, A.; RAMOS, F. M.; QUEIROZ, G. R. de. A time-weighted dynamic time warping method for land-use and land-cover mapping. **IEEE Journal of Selected Topics in Applied Earth Observations and Remote Sensing**, v. 9, n. 8, p. 3729–3739, aug 2016. ISSN 1939-1404. 18

MAXWELL, S. K. Filling Landsat ETM+ SLC-off gaps using a segmentation model approach. **Photogrammetric Engineering & Remote Sensing**, v. 70, n. 10, p. 1109–1111, 2004. ISSN 00991112. 2, 7, 30, 31

MAXWELL, S. K.; SCHMIDT, G. L.; STOREY, J. C. A multi-scale segmentation approach to filling gaps in Landsat ETM+ SLC-off images. **International Journal of Remote Sensing**, v. 28, n. 23, p. 5339–5356, 2007. ISSN 01431161. xv, 2, 31, 33, 42, 43, 46, 55, 58, 60, 62, 64, 74, 75

MEINEL, G.; NEUBERT, M.; SENSING, R.; CITY, L. A comparison of segmentation programs for high resolution remote sensing data. **International Archives of Photogrammetry and Remote Sensing**, v. 35, n. 2, p. 1097–1105, 2004. 22

MOUSIVAND, A.; MENENTI, M.; GORTE, B.; VERHOEF, W. Multi-temporal, multi-sensor retrieval of terrestrial vegetation properties from spectral-directional radiometric data. **Remote Sensing of Environment**, v. 158, p. 311–330, 2015. ISSN 00344257. 25

MÜLLER, M. **Information retrieval for music and motion**. Berlin: Springer, 2007. 313 p. ISSN 1195096X. ISBN 9783540740476. 18, 21

MYNENI, R.; KNYAZIKHIN, Y.; PARK, T. **MCD15A3H MODIS/Terra+Aqua leaf area index/FPAR 4-day L4 global 500m SIN Grid V006**. 2015. Available from: <https://doi.org/10.5067/MODIS/MCD15A3H.006>. Access in: 19 Jan. 2017. 29

_____. **MCD15A3H MODIS/Terra+Aqua leaf area index/FPAR 8-day L4 global 500m SIN grid V006**. 2015. Available from: <https://doi.org/10.5067/MODIS/MCD15A2H.006>. Access in: 19 Jan. 2017. 29

PEREIRA, M. C. **Detecção, monitoramento e análises de alguns impactos ambientais de queimadas na Amazônia usando dados de avião e dos satélites NOAA e Landsat.** 270 p. INPE-4503-TDL/326. Dissertação (Mestrado em Sensoriamento Remoto) — Instituto Nacional de Pesquisas Espaciais (INPE), São José dos Campos, 1988. Available from: <http://urlib.net/rep/6qtX3pFwXQZ3r59YD6/GNooP>. Access in: 19 Ago. 2018. 25

PETITJEAN, F.; INGLADA, J.; GANÇARSKI, P. Satellite image time series analysis under time warping. **IEEE Transactions on Geoscience and Remote Sensing**, v. 50, n. 8, p. 3081–3095, 2012. ISSN 01962892. 2, 15, 17, 18

PINTO, C.; PONZONI, F.; CASTRO, R.; LEIGH, L.; MISHRA, N.; AARON, D.; HELDER, D. First in-flight radiometric calibration of MUX and WFI on-board CBERS-4. **Remote Sensing**, v. 8, n. 5, p. 405, 2016. ISSN 2072-4292. 3, 4, 10, 11, 26, 29

POHL, C.; VAN GENDEREN, J. L. Review article multisensor image fusion in remote sensing: concepts, methods and applications. **International Journal of Remote Sensing**, v. 19, n. 5, p. 823–854, 1998. ISSN 0143-1161. 25

POLIDORIO, A. M.; FLORES, F. C.; FRANCO, C.; IMAI, N. N. I.; TOMMASELLI, A. M. G. Detecção automática de sombras e nuvens em imagens CBERS e Landsat 7 ETM. In: SIMPÓSIO BRASILEIRO DE SENSORIAMENTO REMOTO, 13., 2005, Goiânia, Brazil. **Anais...** São José dos Campos: INPE, 2005. p. 4233–4240. 11

PONS, X.; PESQUER, L.; CRISTÓBAL, J.; GONZÁLEZ-GUERRERO, O. Automatic and improved radiometric correction of Landsat imagery using reference values from MODIS surface reflectance images. **International Journal of Applied Earth Observation and Geoinformation**, v. 33, n. 1, p. 243–254, 2014. ISSN 15698432. 11

ROUSE, J. W.; HAAS, R. H.; SCHELL, J. A.; DEERING, D. W.; HARLAN, J. C. Monitoring the vernal advancements and retrogradation of natural vegetation. In: EARTH RESOURCES TECHNOLOGY SATELLITE-1 SYMPOSIUM, 9., 1974, Washington, USA. **Proceedings...** Washington: NASA, 1974. p. 1–137. 16

ROY, D. P.; ZHANG, H. K.; JU, J.; GOMEZ-DANS, J. L.; LEWIS, P. E.;
SCHAAF, C. B.; SUN, Q.; LI, J.; HUANG, H.; KOVALSKYY, V. A general
method to normalize Landsat reflectance data to nadir BRDF adjusted reflectance.
Remote Sensing of Environment, v. 176, p. 255–271, 2016. ISSN 00344257. 3,
4, 27

SAKOE, H.; CHIBA, S. A dynamic programming approach to continuous speech
recognition. In: INTERNATIONAL CONGRESS ON ACOUSTICS, 7., 1971,
Budapeste, Hungria. **Proceedings...** Hungria: ICA, 1971. p. 65–69. 18

SAMAIN, O.; GEIGER, B.; ROUJEAN, J. L. Spectral normalization and fusion of
optical sensors for the retrieval of BRDF and albedo: application to
VEGETATION, MODIS, and MERIS data sets. **IEEE Transactions on
Geoscience and Remote Sensing**, v. 44, n. 11, p. 3166–3178, 2006. ISSN
01962892. 25, 26, 27

SAMAIN, O.; ROUJEAN, J. L.; GEIGER, B. Fusion of AVHRR and
VEGETATION data using a Kalman filter for the retrieval of surface BRDF and
albedo. **International Geoscience and Remote Sensing Symposium
(IGARSS)**, v. 2, n. 1, p. 1142–1145, 2005. 3, 26

SCHAAF, Z. W. C. **MCD43A1 MODIS/Terra+Aqua BRDF/albedo model
parameters daily L3 global - 500m V006**. 2015. Available from:
<https://doi.org/10.5067/MODIS/MCD43A1.006>. Access in: 19 Jan. 2017. 29

SEDAGHAT, A.; EBADI, H. Distinctive order based self-similarity descriptor for
multi-sensor remote sensing image matching. **ISPRS Journal of
Photogrammetry and Remote Sensing**, v. 108, p. 62–71, 2015. ISSN
09242716. 9

SHAO, Y.; LUNETTA, R. S.; WHEELER, B.; IIAMES, J. S.; CAMPBELL, J. B.
An evaluation of time-series smoothing algorithms for land-cover classifications
using MODIS-NDVI multi-temporal data. **Remote Sensing of Environment**,
v. 174, p. 258–265, 2016. ISSN 00344257. 17

SHEIKH, H. R.; BOVIK, A. C. Image information and visual quality. **IEEE
Transactions on Image Processing**, v. 15, n. 2, p. 430–444, 2006. ISSN
1057-7149. Available from: <http://dx.doi.org/10.1109/TIP.2005.859378>.
52, 53, 56

SHEN, H.; HUANG, L.; ZHANG, L.; WU, P.; ZENG, C. Long-term and fine-scale satellite monitoring of the urban heat island effect by the fusion of multi-temporal and multi-sensor remote sensed data: a 26-year case study of the city of Wuhan in China. **Remote Sensing of Environment**, v. 172, p. 109–125, 2016. ISSN 00344257. Available from: <http://dx.doi.org/10.1016/j.rse.2015.11.005>. 3

SHIMABUKURO, Y. E.; PONZONI, F. J. **Modelo linear e aplicações**. São Paulo: Oficina de Textos, 2017. 128 p. ISBN 978-85-7975-270-4. 27

SHIMABUKURO, Y. E.; SANTOS, J. R.; HERNANDEZ FILHO, P.; LEE, D. C. L. **Avaliação conjuntural da técnica de abordagem multisensor para o monitoramento da vegetação do brasil**. São José dos Campos, 1991. 13 p. Available from: <http://mtc-m12.sid.inpe.br/col/sid.inpe.br/iris@1912/2005/07.19.22.18.28/doc/INPE%205326.pdf>. 25

SILVA, M. A. O. da; LIPORACE, F. d. S. Detecção automática de nuvem e sombra de nuvem em imagens de sensoriamento remoto. **Boletim de Ciências Geodésicas**, v. 22, n. 2, p. 369–388, jun 2016. ISSN 1982-2170. Available from: <http://www.scielo.br/scielo.php?script=sci{_}arttext{&}pid=S1982-21702016000200369{&}lng=pt{&}nrm=iso{&}tlng=en>. 12, 13, 15, 38, 75

SOUZA, C. F. S.; PANTOJA, C. E. P.; SOUZA, F. C. M. Verificação de assinaturas offline utilizando dynamic timewarping. In: CONGRESSO BRASILEIRO DE REDES NEURAIS, 9., 2009, Ouro Preto, Brazil. **Anais...** ABRICOM, 2009. p. 25–28. Available from: <http://www.cricte2004.eletrica.ufpr.br/anais/cbrn/2009/108{_}CBRN2009.pdf>. 20, 21

STEVEN, M. D.; MALTHUS, T. J.; BARET, F.; XU, H.; CHOPPING, M. J. Intercalibration of vegetation indices from different sensor systems. **Remote Sensing of Environment**, v. 88, n. 4, p. 412–422, 2003. ISSN 00344257. 4, 15, 25, 27

STOREY, J.; SCARAMUZZA, P.; SCHMIDT, G. Landsat 7 scan line corrector-off gap-filled product development. In: PECORA GLOBAL PRIORITIES IN LAND REMOTE SENSING, 16., 2005, Sioux Falls, USA. **Proceedings...** South Dakota: ASPRS, 2005. p. 23–27. Available from: <https://pdfs.semanticscholar.org/52ec/df3f8086959f68bebe4fe6f494cb67e0962e.pdf>. 7, 30

SUNDARESAN, A.; VARSHNEY, P. K.; ARORA, M. K. Robustness of change detection algorithms in the presence of registration errors. **Photogrammetric Engineering & Remote Sensing**, v. 73, n. 4, p. 375–383, apr 2007. ISSN 00991112. 8

THOMPSON, J. A.; LEES, B. G. Applying object-based segmentation in the temporal domain to characterise snow seasonality. **ISPRS Journal of Photogrammetry and Remote Sensing**, v. 97, p. 98 – 110, 2014. ISSN 0924-2716. 24

TOBLER, W. R. A computer movie simulating urban growth in the Detroit region. **Economic Geography**, v. 46, n. 277, p. 234, 1970. ISSN 00130095. 30

TOTH, C.; JÓŹKÓW, G. Remote sensing platforms and sensors: a survey. **ISPRS Journal of Photogrammetry and Remote Sensing**, v. 115, p. 22–36, 2016. ISSN 09242716. 8

TRISHCHENKO, A. P.; CIHLAR, J.; LI, Z. Effects of spectral response function on surface reflectance and NDVI measured with moderate resolution satellite sensors. **Remote Sensing of Environment**, v. 81, n. 1, p. 1–18, 2002. ISSN 00344257. 4, 26

UNITED STATES GEOLOGICAL SURVEY - USGS. **Product guide: climate data record (CDR)**. Sioux Falls, 2015. 27 p. Available from: <https://pubs.usgs.gov/fs/2013/3117/>. Access in: 10 Oct. 2017. 12

_____. **MODIS ASCII subset products - FTP access**. 2016. Available from: <https: //lpdaac.usgs.gov/dataset_discovery/modis/modis_products_table>. Access in: 19 Jan. 2017. 29

_____. **Landsat analysis ready data (ARD)**. 2017. Available from: <https://landsat.usgs.gov/ard>. Access in: 17 Nov. 2017. 34

_____. **Landsat collection 1 level 1 product definition**. Sioux Falls, 2017. 32 p. Available from: <https://landsat.usgs.gov/sites/default/files/documents/LSDS-1656_ Landsat_Level-1_Product_Collection_Definition.pdf>. Access in: 17 Nov. 2017. 38, 39

_____. **Product guide: Landsat 4-7 surface reflectance (LEDAPS) Product**. Sioux Falls, 2017. 36 p. Available from: <https://landsat.usgs.gov/sites/default/files/documents/ledaps_product_guide.pdf>. Access in: 10 Nov. 2017. 11, 38

_____. **Product guide: Landsat 8 surface reflectance code (LaSRC) Product**. Sioux Falls, mar 2017. 36 p. Available from: <https://prd-wret.s3-us-west-2.amazonaws.com/assets/palladium/production/s3fs-public/atoms/files/LSDS-1368_%20L8_Surface-Reflectance-Code-LASRC-Product-Guide.pdf>. Access in: 17 Nov. 2017. 11, 38

_____. **User guide: Earth resources observation and science (EROS) Center Science Processing Architecture (ESPA) on demand interface**. Sioux Falls, 2017. 35 p. Available from: <https://www.sciencebase.gov/catalog/item/53bbc188e4b084059e8bff0a>. Access in: 18 Nov. 2017. 11, 38

VERBESSELT, J.; HYNDMAN, R.; NEWNHAM, G.; CULVENOR, D. Detecting trend and seasonal changes in satellite image time series. **Remote Sensing of Environment**, v. 114, n. 1, p. 106–115, 2010. ISSN 00344257. 16

VUOLO, F.; NG, W.-T.; ATZBERGER, C. Smoothing and gap-filling of high resolution multi-spectral time series: example of Landsat data. **International Journal of Applied Earth Observation and Geoinformation**, v. 57, p. 202–213, 2017. ISSN 03032434. 2, 17, 26, 34, 35, 42, 48, 52, 74

WANG, Z.; BOVIK, A. C. A universal image quality index. **IEEE Signal Processing Letters**, v. 9, n. 3, p. 81–84, 2002. ISSN 1070-9908. 53

WEISS, D. J.; ATKINSON, P. M.; BHATT, S.; MAPPIN, B.; HAY, S. I.; GETHING, P. W. An effective approach for gap-filling continental scale remotely sensed time-series. **ISPRS Journal of Photogrammetry and Remote Sensing**, v. 98, p. 106 – 118, 2014. ISSN 0924-2716. 35

WOODCOCK, C. E.; ALLEN, R.; ANDERSON, M.; BELWARD, A.; BINDSCHADLER, R.; COHEN, W.; GAO, F.; GOWARD, S. N.; HELDER, D.; HELMER, E. H.; NEMANI, R.; OREOPOULOS, L.; SCHOTT, J.; THENKABAIL, P. S.; VERMOTE, E. F.; VOGELMANN, J. E.; WULDER, M. A.; WYNNE, R. H. Free access to Landsat imagery. **Science**, v. 320, n. 5, p. 1011–1012, 2008. ISSN 00368075. 1

WULDER, M. A.; HILKER, T.; WHITE, J. C.; COOPS, N. C.; MASEK, J. G.; PFLUGMACHER, D.; CREVIER, Y. Virtual constellations for global terrestrial monitoring. **Remote Sensing of Environment**, v. 170, p. 62–76, 2015. ISSN 00344257. 4, 8, 27

WULDER, M. A.; MASEK, J. G.; COHEN, W. B.; LOVELAND, T. R.; WOODCOCK, C. E. Opening the archive: how free data has enabled the science and monitoring promise of Landsat. **Remote Sensing of Environment**, v. 122, p. 2–10, 2012. ISSN 00344257. 1, 25

WULDER, M. A.; WHITE, J. C.; LOVELAND, T. R.; WOODCOCK, C. E.; BELWARD, A. S.; COHEN, W. B.; FOSNIGHT, E. A.; SHAW, J.; MASEK, J. G.; ROY, D. P. The global Landsat archive: Status, consolidation, and direction. **Remote Sensing of Environment**, v. 185, p. 271–283, 2016. ISSN 00344257. Available from: <http://dx.doi.org/10.1016/j.rse.2015.11.032>. 8

XAUD, H. A. M.; SANTOS, J. R. Contribuição da abordagem multisensor no monitoramento de florestas tropicais afetadas por incêndios recorrentes. In: SEMINÁRIO DE ATUALIZAÇÃO EM SENSORIAMENTO REMOTO E SISTEMAS DE INFORMAÇÕES GEOGRÁFICAS APLICADOS À ENGENHARIA FLORESTAL, 9., 2010, Curitiba, Brazil. **Proceedings...** [S.l.]: Unicentro, 2010. p. 170–177. 28, 29

YOUNG, N. E.; ANDERSON, R. S.; CHIGNELL, S. M.; VORSTER, A. G.; LAWRENCE, R.; EVANGELISTA, P. H. A survival guide to Landsat preprocessing. **Ecology**, v. 98, n. 4, p. 920–932, 2017. ISSN 00129658. 8, 10

ZHANG, J. Multi-source remote sensing data fusion: status and trends. **International Journal of Image and Data Fusion**, v. 1, n. 1, p. 5–24, 2010. ISSN 1947-9832. Available from: <http://www.tandfonline.com/doi/abs/10.1080/19479830903561035>. 29

ZHU, Z.; WANG, S.; WOODCOCK, C. E. Improvement and expansion of the Fmask algorithm: cloud, cloud shadow, and snow detection for Landsats 4-7, 8, and Sentinel 2 images. **Remote Sensing of Environment**, v. 159, p. 269 – 277, 2015. ISSN 0034-4257. 12, 34, 38

ZHU, Z.; WOODCOCK, C. E. Object-based cloud and cloud shadow detection in Landsat imagery. **Remote Sensing of Environment**, v. 118, p. 83 – 94, 2012. ISSN 0034-4257. 12, 38

ZITOVÁ, B.; FLUSSER, J. Image registration methods: a survey. **Image and Vision Computing**, v. 21, n. 11, p. 977–1000, 2003. ISSN 02628856. 8, 9

ZURITA-MILLA, R.; CLEVERS, J. G. P. W.; SCHAEPMAN, M. E. Unmixing-based Landsat TM and MERIS FR data fusion. **IEEE Geoscience and Remote Sensing Letters**, v. 5, n. 3, p. 453–457, 2008. ISSN 1545598X. 27, 28

APPENDIX A: R SCRIPT OF GAP-FILLING THROUGH MULTI-SCALE SEGMENTATION

```
library(raster)
fillMarujo <- function(imgGap,imgRef,imgSegMask1,imgSegMask2,
                       imgSegMask3){
  cat("Filling...")
  # Get all image value as a vector
  Gappixels <- values(imgGap)
  Refpixels <- values(imgRef)
  seg1pixels <- values(imgSegMask1)
  seg2pixels <- values(imgSegMask2)
  seg3pixels <- values(imgSegMask3)

  # Get segmentation IDs
  segNum <- unique(seg1pixels)

  # Label the vector with the segment number
  names(Gappixels) <- values(imgSegMask1)
  names(Refpixels) <- values(imgSegMask1)

  # Get the value as a vector, test if the value is NA
  NA_which <- which(is.na(Gappixels))

  # Get the segments that contain those NA pixels
  segsWithNA <- vector()
  segsWithNA <- as.numeric(unique(names(NA_which)))
  Segmentationpixels <- which(names(Gappixels)
  %in% segsWithNA)

  #Selects ALL pixels that will be used in filling process
  GapElements <- imgGap[Segmentationpixels]
  names(GapElements) <- imgSegMask1[Segmentationpixels]
  # Store the elements in a list of segments
  SegmentListGap  <- list()
  SegmentListGap  <- split(GapElements,
  f = names(GapElements))
```

```
#Select filling process pixels
RefElements <- Refpixels[Segmentationpixels]
#names(RefElements) <- imgSeg[Segmentationpixels]
SegmentListRef  <- list()
SegmentListRef  <- split(RefElements, f = names(RefElements))
SegmentListpixel <- list()
SegmentListpixel <- split(Segmentationpixels,
                              f = names(RefElements) )


listIndexpixelOrderNA <- which(is.na(
                          unlist(SegmentListGap) ) )


for(s in 1:length(SegmentListGap)){
  #Check NA value
      if (any( is.na(SegmentListGap[[s]]) ) ){
        # not all are NA
        if(!all( is.na(SegmentListGap[[s]]) ) ){
          RefsegmentMean = mean(SegmentListRef[[s]],
                                    na.rm = T)
              GapsegmentMean = mean(SegmentListGap[[s]],
                                    na.rm = T)
              RefsegmentDeviationProp = SegmentListRef[[s]]
                                      / RefsegmentMean
          indexNA = which(is.na(SegmentListGap[[s]]) )

              SegmentListGap[[s]][indexNA] = GapsegmentMean
                        * RefsegmentDeviationProp[indexNA]
                    SegmentListGap_filled[[s]] <- SegmentListGap[[s]]
      }
        else{ #all are NA #use level 2
              lvl1segname <- as.numeric(names(
                  SegmentListRef[[s]][1])[1])
              lvl1segpixel <- which(seg1pixels[] ==
                                  lvl1segname)[1]
              seg2 <- seg2pixels[lvl1segpixel]
              seg2Indexes <- which(seg2pixels[] == seg2)
              valuesSeg2 <- Gappixels[seg2Indexes]

                            96
```

```r
    if (!all( is.na(valuesSeg2) ) ){ # not all are NA
RefsegmentMean = mean(Refpixels[seg2Indexes],
                        na.rm = T)
    GapsegmentMean = mean(Gappixels[seg2Indexes],
                            na.rm = T)
    RefsegmentDeviationProp = SegmentListRef[[s]]
                                / RefsegmentMean
    indexNA = which(is.na(SegmentListGap[[s]]) )

    SegmentListGap[[s]][indexNA] = GapsegmentMean
                * RefsegmentDeviationProp[indexNA]
    SegmentListGap_filled[[s]] <- SegmentListGap[[s]]
  }
  else{
    lvl1segname <- as.numeric(names(
          SegmentListRef[[s]][1])[1])
    lvl1segpixel <- which(seg1pixels[] ==
                            lvl1segname)[1]
    seg3 <- seg3pixels[lvl1segpixel]
    seg3Indexes <- which(imgSegMask3[] == seg3)
    valuesSeg3 <- Gappixels[seg3Indexes]
    if (!all( is.na(valuesSeg3) ) ){ # not all are NA
      RefsegmentMean = mean(Refpixels[seg3Indexes],
                            na.rm = T)
        GapsegmentMean = mean(Gappixels[seg3Indexes],
                            na.rm = T)
        RefsegmentDeviationProp = SegmentListRef[[s]]
                                    / RefsegmentMean
        indexNA = which(is.na(SegmentListGap[[s]]) )

        SegmentListGap[[s]][indexNA] = GapsegmentMean
                    * RefsegmentDeviationProp[indexNA]
    SegmentListGap_filled[[s]] <- SegmentListGap[[s]]
    }
    else{
      SegmentListGap_filled[[s]] <- SegmentListGap[[s]]
    }
```

```
                }
              }
            }
            else{
              return(SegmentListGap[[s]])
            }
        }
    pixelOrder <- unlist(SegmentListpixel)
    pixelOrderNA <- pixelOrder[listIndexpixelOrderNA]
    imgGap[pixelOrder] = unlist(SegmentListGap_filled)

    return(imgGap)
}


### DEMO Data ###
imgSegMask1 <- raster(matrix(c(10,10,10,10,10,20,20,10,10,20,
                              20,10,10,10,10,30),4,4))
imgSegMask2 <- raster(matrix(c(10,10,10,10,10,10,10,10,10,10,
                              10,10,10,10,10,30),4,4))
imgSegMask3 <- raster(matrix(c(10,10,10,10,10,10,10,10,10,10,
                              10,10,10,10,10,10),4,4))
imgGap        <- raster(matrix(c(1,2,3,4,2,20,22,2,NA,NA,NA,NA,
                              NA,NA,NA,NA),4,4))
imgRef        <- raster(matrix(c(10,20,30,40,20,20,22,20,30,40,
                              50,60,70,80,90,00),4,4))
##################

filledimg <- fillMarujo(imgGap,imgRef,imgSegMask1,imgSegMask2,
                        imgSegMask3)
```

98

APPENDIX B: R SCRIPT OF GAP-FILLING THROUGH SEGMENTATION TIME SERIES MATCHING

```r
library(raster)
library(foreach)
library(doParallel)
library(zoo)

calcMeanTS <- function (TSlist){
  useindex <- lapply(TSlist, is.na)
  meanTS <- rep(0, length=length(useindex[[1]]) )
  countVec <- rep(0, length=length(useindex[[1]]) )
  for(a in 1:length(TSlist)){
    pos <- which(useindex[[a]] == F)
    countVec[pos] <- countVec[pos] +1
    meanTS[pos] <- meanTS[pos] + TSlist[[a]][pos]
  }
  meanTS[meanTS==0] <- NA
  meanTS <- meanTS/countVec
  meanTS <- na.spline(meanTS)
}

# Calculate the number of cores
no_cores <- detectCores() - 1
# Initiate cluster
cl <- makeCluster(no_cores)
registerDoParallel(cl)

#For each segment
for(i in 1:numSegs){
  segmentTS <- list()
  numTS <- length(SegmentList[[i]])
  #For each TimeSeries in segment
  #Extract all time series
  for(k in 1:numTS){
    segmentTS[[k]] <- as.numeric(extract(myStack,
    SegmentList[[i]][k]))
  }
```

```r
    #Check if any element is NA in the segment
    if( any( unlist( lapply(segmentTS, is.na) )) ){
      TS_mean <- calcMeanTS(segmentTS)
      #which TS contain NA but are not all values
      TS_with_NA <- intersect( which( sapply(
                            lapply(segmentTS, is.na), any )),
      which(!sapply( lapply(
                            segmentTS,is.na),all)))

      to_be_filled_pos <- vector("list",numImgs)
      to_be_filled_value <- vector("list",numImgs)
      for(k in TS_with_NA){
        NAindex <- which(is.na(segmentTS[[k]]))
        for( img in NAindex){
          to_be_filled_pos[[img]] <- append(
                            to_be_filled_pos[[img]],
                            SegmentList[[i]][k])
          to_be_filled_value[[img]] <- append(
                            to_be_filled_value[[img]],
                            TS_mean[img])
        }
      }
      for( img in 1:numImgs){
        if(!is.null(to_be_filled_pos[[img]])){
          to_be_filled_pos_list[[img]] <-
                            append(to_be_filled_pos_list[[img]],
                            to_be_filled_pos[[img]])
          to_be_filled_value_list[[img]] <-
                            append(to_be_filled_value_list[[img]],
                            to_be_filled_value[[img]])
        }
      }
    }
  }
stopCluster(cl)
```